Title
Measurement of the Cosmic Microwave Background Polarization with the BICEP Telescope at the South Pole

Author
Takahashi, Yuki David

Publication Date
2010

Peer reviewed|Thesis/dissertation

Measurement of the Cosmic Microwave Background Polarization with the BICEP Telescope at the South Pole

by

Yuki David Takahashi

A dissertation submitted in partial satisfaction of the

requirements for the degree of

Doctor of Philosophy

in

Physics

in the

Graduate Division

of the

University of California, Berkeley

Committee in charge:

Professor William L. Holzapfel, Chair

Professor Adrian T. Lee

Professor Chung-Pei Ma

Fall 2010

Measurement of the Cosmic Microwave Background Polarization
with the BICEP Telescope at the South Pole

Yuki David Takahashi

Abstract

Measurement of the Cosmic Microwave Background Polarization
with the BICEP Telescope at the South Pole

by

Yuki David Takahashi

Doctor of Philosophy in Physics

University of California, Berkeley

Professor William L. Holzapfel, Chair

The question of how exactly the universe began is the motivation for this work. Based on the discoveries of the cosmic expansion and of the cosmic microwave background (CMB) radiation, humans have learned of the Big Bang origin of the universe. However, what exactly happened in the first moments of the Big Bang? A scenario of initial exponential expansion called "inflation" was proposed in the 1980s, explaining several important mysteries about the universe. Inflation would have generated gravitational waves that would have left a unique imprint in the polarization of the CMB. To search for this evidence for inflation, a team gathered in 2002 to design a telescope experiment called BICEP. Sited at the South Pole, BICEP was a novel 25-cm aperture refractor with 49 pairs of polarization-sensitive bolometers. We completed 3 years of successful observations from February 2006 to December 2008. To constrain the amplitude of polarization resulting from inflation, expected to be at least 7 orders of magnitude fainter than the 3 K CMB intensity, precise control of systematic effects is essential. A crucial challenge is preventing systematic errors from introducing false polarization anisotropy signal at the level corresponding to $\sim$0.1 μK in amplitude. One main focus of this thesis is the characterization of systematic effects for BICEP. We developed a simulation framework for propagating instrumental systematic effects to the final polarization results. Based on these simulations, we established benchmarks for the characterization of critical instrumental properties including bolometer relative gains, beam mismatch, polarization orientation, telescope pointing, sidelobes, thermal stability, and timestream noise model. Guided by these benchmarks, we carefully measured these properties and have shown that we have characterized the instrument adequately to ensure that systematic errors do not limit BICEP's current cosmology results. We have analyzed the first 2 years of data, lowering the upper limits on the gravitational-wave induced polarization by an order of magnitude over all previous experiments. The systematic error analysis has identified what future refinements are likely necessary to probe CMB polarization down to levels corresponding to inflationary energy scales below 2×10^{16} GeV.

Contents

List of Figures

List of Tables

Acknowledgements

First I'd like to thank my parents for raising me strictly during the first several years of my life, not giving us kids any candies, teaching us discipline, and taking us to the Gotemba library when I was 9 years old, where I encountered an astronomy encyclopedia that sparked my fascination about the universe. Thank you for letting me be independent and being supportive of my move from Japan to the USA for high school.

At Midland High School, I'd like to thank my physics teacher Chuck Trzcinski for letting me pursue an independent study with my somewhat ambitious goal of formulating a theory that explains all four fundamental forces. In college at Caltech, it was a privilege being a physics lab partner with Chris Hirata – thank you for always being helpful and patient with my questions throughout. Thanks also to Professor George Djorgovski for helping me study about the Big Bang. During my MSc research in the UK, I appreciated our little cosmology study group that Dr. Martin Hendry organized.

Starting up at Berkeley, I thank my fellow classmates and International House mates – Brad Zamft, Jason Bowen, and Miguel Daal – for the many late nights helping each other survive through difficult classes. Friendly faces of Anne Takizawa and Donna Sakima also helped me feel more comfortable in this big Physics Department.

When I first came to Berkeley, Adrian Lee inspired me about experimental studies of the Big Bang – thank you for your contagious enthusiasm. I also enjoyed Chung-Pei Ma's cosmology classes and appreciated the opportunity to freely investigate topics of my interest – thank you for being so friendly. I'm grateful to my adviser Bill Holzapfel for giving me a chance to work on this exciting project. Thank you for staying late nights in the lab helping me get my breadboard circuits working. I appreciated having an adviser who is very sharp, outspoken, and direct – qualities I've always wanted to gain more of.

As I worked on my first hardware projects for BICEP, I'd like to thank Nils Halverson for ground shield discussion, Sherry Cho for being smiley, Dave Woolsey for the AutoCAD drawing expertise, John Davis for advices about electronic design, and the machinists – Marco, Steve, Dave, and Abel – for being friendly and approachable. Thanks also to Katalin and Anthony for assisting me with purchases. I also benefited from exchanges with very helpful *WMAP* team members Ed Wollack, Al Kogut, and Gary Hinshaw at NASA Goddard.

Having spent a cumulative 15 months at Caltech/JPL over 25 trips, I was blessed with the opportunity to learn from and work closely with impressive researchers and students. John Kovac was my second mentor – thank you for teaching me to spend $40 on a simple toggle switch :) and for being a role model. Cynthia Chiang was such a pleasant and fun buddy to be around with – thank you for always being so helpful with everything including my analysis, paper, and thesis. Ki Won Yoon was our senior student to look up to – thank you for the fun times and all the quality photos! Denis added a new refreshing flavor to Team BICEP – thank you for all the fun adventures together and for introducing me to paragliding! Evan Bierman was our newest student – thank you for making me feel comfortable to bring up any questions. Christian Reichardt has always been a source of physics and math wisdom – thank you for being open to answering my questions, both at Caltech and Berkeley. I also enjoyed being around Justus Brevik, Greg Griffin, Abby Crites, Ian Sullivan, Jack Sayers, Amy Trangsrud, John Battle, Viktor Hristov, Brendan Crill, Marc Runyan, Walt Ogburn,

and Jeff Filippini. For discussions about noise analysis and systematic effects simulations, I thank Eric Hivon, Nicolas Ponthieu, Clem Pryke, Chao-Lin Kuo, and Graca Rocha. Thanks also to Kathy Deniston and Barbara Wertz for taking great care of me. Finally, our principal investigator Andrew Lange was the one who made the BICEP project possible.

I'm grateful to my friends around the Los Angeles area for helping to keep my transient life during Caltech visits more in balance. I'd like to thank Chris Henderson for putting me up many nights, Phil Venturelli for all the quality times, and Jon Fish for always being so supportive. Thanks also to Joe Kirschvink for generously preventing me from being homeless by welcoming me into his home. Finally, Edmond at http://shuttle4less.com/ saved me so much time by being the most reliable and personable shuttle driver – you'd want to call him if you ever fly into or out of Burbank/LA!

It was a privilege being able to spend a total of 8.5 months at the South Pole; I really appreciated the chance to get to know my teammates better. For the first 2 trips, it was fun being on the first crew with Pete Mason, who is 80+ years old and one of the oldest people to have been at the South Pole. Darren Dowell impressed me with his volleyball skills – thank you for being reliably responsive to my inquiries and for your humility. Jamie Bock helped with the polarization calibrator calculations – thank you for the good times at the Pole. Brian Keating brought a spiritual element to this whole quest – thank you for always being encouraging, friendly, and responsive. Tomo Matsumura was my Japanese-speaking buddy – thank you for thinking with me about the polarization calibrator. Our winterover scientist Steffen Richter was a pure charm. I also appreciate all the fun at the Pole with Bill Jones, Erik Leitch, Hien Nguyen, Rashmi Sudiwala, Joaquin Vieira, Zak Staniszewski, Steve Padin, and John Carlstrom. Finally, I thank the United States Antarctic Program and the Raytheon Polar Services staff and all the "Polies" at the South Pole station for making my experience there the best thing ever in my life. Special thanks to Bob Spotz for machining help, Jim Clash for being friendly and mentioning BICEP in the Forbes magazine, and Steve Durst for being supportive of my work in Antarctica.

Back in Berkeley, I felt blessed with very nice fellow students – Martin Lueker, Tom Plagge, Erik Shirokoff, and Mike Daub – Bill seems to attract the sweetest people! Postdoc Brad Benson was no exception – thank you for being so friendly. I'm also glad to have had Roger O'Brient in our group, a familiar face from Caltech. Thanks also to other lab mates – Mike Myers, Jared Mehl, Ziggy Kermish, and Kam Arnold – for qualifying exam studies and lab support. I'm grateful to Erin Quealy for making me feel comfortable about discussing any things and being supportive of my dreaded qualifying exam. I must thank Bernard Sadoulet and other committee members for letting me pass :). Our visiting student Joseph Martino from Paris was a happy addition to my work experience. I also thank Liz George for brightening up our office and making it much more lively all of a sudden. Other young students – Ben Westbrook, Dan Flanigan, Bryan Steinbach, Toki Suzuki, Nick Harrington, and Ed Young – all inspired me to finish my thesis before they start talking about getting their PhDs. Finally, I owe my happiness to the communities and friends at the International House and Lothlorien Co-op. I'd like to thank the best friends I've had along the way in Berkeley. Nacchan, thank you for taking good care of me. Nick, thank you for letting me feel more free and keeping me in better shape through Capoeira and soccer. Katie, thank you for the many adventures and for balancing out my life during this thesis work.

Chapter 1

How did the universe begin?

When I was 11 years old, at a bookstore I picked up "A Book that Makes Cosmology Fun" (in Japanese) and became absorbed by the wonders of the universe. It inspired me to spend much of my pocket money to buy Stephen Hawking's "A Brief History of Time". When I reread it at age 15, I began to wonder about the origin of the universe and my existence. *Where did everything come from? Why do we and the universe exist?* I read about the Big Bang theory. *If the universe really had a beginning, why did it start? How exactly did it start?* Such sequence of questions is what led me to dedicate my time to go after this fundamental mystery.[1]

How could we try to study how the universe began? The first step may be to get a basic picture of the present universe. In the darkest and clearest sky, we can generally see up to 3000 stars. These turn out to be huge fireballs like the Sun. Then we notice a fuzzy band across the sky, called the Milky Way. Looking through a telescope, we discover that this band is made up of countless faint stars that our naked eyes cannot resolve.

Near the "W"-shaped constellation Cassiopeia opposite from the North Star, we can see a fuzzy elliptical area, called Andromeda. Looking closely through large telescopes, we discover that it is a collection of billions of stars – and that it is far beyond the Milky Way!

We realized that our Sun, our solar system, is part of a huge collection of stars going around a common center in a flat disc, just like the Andromeda Galaxy. The Milky Way band across the sky is just a view of our own galaxy from within. We realized that the countless stars we see in the darkest sky constitute merely 3000 closest neighbors out of about 300,000,000,000 stars in our galaxy. And as many as 100,000,000,000 galaxies seem to exist in the observable universe.

In the 1920s, humans discovered that the universe is expanding. This led physicists to deduce that the universe started out with a "Big Bang" of extremely concentrated energy in a finite past. The leftover radiation from this hot past was discovered in the 1960s. This provided nearly conclusive evidence for the Big Bang theory. The next question of how the Big Bang itself began has a potential answer called "Inflation", proposed in the early 1980s. This model of the universe exponentially inflating during the first tiny fraction of a second explains many outstanding mysteries about the universe, including the origin of structures that eventually created stars and planets like Earth. Now, the challenge is to find more evidence for it.

[1] Since many of my friends expressed interest in reading my thesis, I tried to make this chapter as readable as possible for those without much exposure to science.

1.1 Expanding universe

In the 1920s, astronomers found that most galaxies[2] seem to be receding from us. Moreover, the farther away the galaxies, the faster they appear to be getting away (Figure 1.1).

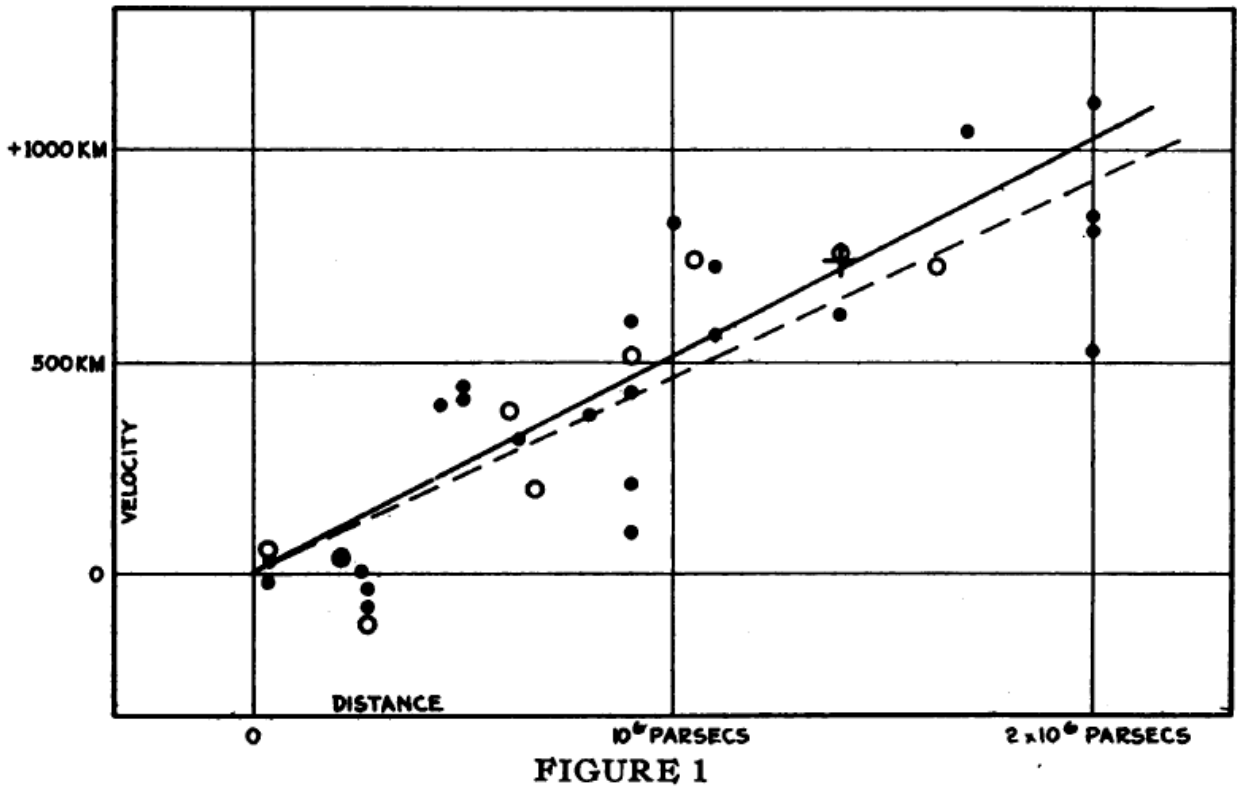

Figure 1.1: Hubble found that the more distant the galaxies (then called "extra-galactic nebulae") the faster they appeared to be receding [19]. The velocity is measured in km/s. "Parsec" is an astronomical distance measure equaling ≈3 light-years. Note: The distance measurements back then were underestimated by a factor of ∼10. So although the velocity-distance ratio here is ∼500 km/s per 10^6 parsecs, we now know it to be ≈70 km/s per 10^6 parsecs.

What could this mean? This suggests that all the galaxies may be getting farther and farther from each other. How could this be? We might first think that everything is getting away from us as if we were at the center of the universe in some pre-existing space.

Until the early 1900s, most people had assumed that the universe was fixed in size. New possibilities opened up in 1915, when Einstein formulated the general relativity theory that described the nature of space, time, and gravity. This theory allowed for expansion or contraction of space. In 1917, astronomer Willem de Sitter applied this theory to the entire

[2]Actually, it was around this time that astronomers found out that most of the fuzzy nebulae, including Andromeda, are objects well beyond the Milky Way.

universe and boldly went on to show that the universe could be expanding [7]. Georges Lemaître reached the same conclusion in a more general way in 1927 [28]. A possible model of the universe is the 3-dimensional surface of a hypersphere that expands like a balloon. Space itself may have been expanding in volume since the beginning, just like the surface of an inflating balloon. The "membrane" of space is stretching, but that does not mean that we or any other matter is also stretching in size (just as a bug or a dust particle on the balloon does not get stretched as we inflate the balloon).

If we were a dust particle stuck on the surface of an inflating balloon, every other dust particles on the surface would appear to be going farther and farther away from us (even if we or any other particles are just stuck on the surface and not moving around... just "riding" on the expanding surface). The farther the dust particle, the faster it would seem to go away from us. This is exactly what Edwin Hubble discovered in the 1920s: all the distant galaxies appear to be going away from us, the more distant ones the faster. In fact, the receding speed seems to be exactly proportional to the distance, which makes sense if space is expanding uniformly everywhere.

If we imagine reversing this trend back in time, all the galaxies must have been closer to each other, as if all the matter was all together at some point in the past. This gave humans a profound realization that the universe is not static; it seems to have evolved from an extreme concentration of all energy and matter. This picture has become known as the "Big Bang". We do not know anything about before the Big Bang, but this was the origin of our present universe.

The expansion rate of 70 km/s per 10^6 parsecs corresponds to $\sim$70 parts per trillion stretch of space per year, meaning that the distance between two locations in space is expanding by this tiny fraction every year. This is equivalent to 2 cm/s per light-year, meaning that the distance to a location currently one light-year away is expanding by 2 cm (about the width of your thumb) every second. To get a feel for how much the universe is expanding, the distance to the Virgo cluster (52,000,000 ly) is expanding at $\sim$1000 km/s.

How has the universe expanded over time? To see this, let's consider a very simple model of a spherically expanding universe with a uniform density everywhere. If the initial expansion happens to be such that the total energy of any test mass happens to be 0, its kinetic energy will always balance its gravitational potential energy:

$$\frac{1}{2}mv^2 = G\frac{mM_r}{r}, \tag{1.1}$$

where $M_r = \frac{4}{3}\pi r^3\rho$ is the mass inside a radius r with density ρ. With $v = dr/dt \equiv \dot{r}$, we can see how the expansion rate changes with time:

$$\left(\frac{\dot{r}}{r}\right)^2 = \frac{8\pi}{3}G\rho(t), \tag{1.2}$$

related to how the density changes as the universe expands.

Instead of talking about an arbitrary distance scale r, we can define the scale factor $a(t)$ as a ratio describing how much smaller this distance scale used to be compared to the present as a result of the universe's expansion: $a(t) \equiv r(t)/r(t_0)$, where t_0 is the present time. For

example, a scale factor of 1/2 means that the universe used to be half the present size at that time. The above expansion rate is called "the Hubble parameter":

$$H(t) \equiv \frac{\dot{a}}{a} = \sqrt{\frac{8\pi}{3} G\rho(t)}, \tag{1.3}$$

proportional to the square root of the density. So, as the universe expanded and became less dense, the expansion became slower and slower.

Thus Einstein's general relativity theory applied to the whole universe indicated that the history of the expansion rate of the universe is directly related to how the energy density in the universe varied over time. For matter, density decreases as it spreads over increasing volume: $\rho_m \propto 1/V \propto a^{-3}$. For radiation, the stretching of space makes the wavelengths of the electromagnetic waves longer and longer, making each photon less and less energetic as the universe expands. So not only does the number density of photons decrease with volume, but also the energy of the photons also decreases: $\rho_r \propto (1/V)(1/\lambda) \propto a^{-4}$.

When was this beginning? We can estimate how long ago this was by dividing the distance to a galaxy by its recessional velocity. This way we estimate how long ago the distance between that galaxy and ours was essentially 0. Inverting 70 parts per trillion per year, all the matter must have been together in a tiny volume about 14 billion years ago. We can calculate more exactly how long it has been since the Big Bang by knowing how the expansion rate of the universe changed over time:

$$H(a) \equiv \frac{da/dt}{a} = H_0 \sqrt{\Omega_{r0}/a^4 + \Omega_{m0}/a^3 + \Omega_{\Lambda 0}}, \tag{1.4}$$

where basically Ω_{r0}, Ω_{m0}, and $\Omega_{\Lambda 0}$ are the fractional energy densities of radiation, matter, and dark energy, respectively, all at the present. Humans have learned that the ordinary matter that makes up everything we see around us (including all the stars and galaxies) sums up to be only 5of the total energy content of the universe. The rest is about 1/4 "dark matter" and 3/4 "dark energy". Dark matter is mysterious, but at least seems to have similar properties as ordinary matter except none of our telescopes can detect its existence directly. Dark energy is even more mysterious: unlike radiation, it seems to have a negative pressure and seems to be responsible for a repulsive anti-gravity effect that has made the universe expand at a greater and greater rate during the last 1/3 of its history. Neglecting radiation because Rearranging the above equation and neglecting radiation because its contribution was negligible for most of the history of the universe,

$$dt \approx \frac{da}{H_0 a \sqrt{\Omega_{m0}/a^3 + \Omega_{\Lambda 0}}}. \tag{1.5}$$

Integrating this from the Beginning (when the scale was nearly zero) to the present (when the scale factor is 1), and with the knowledge that $\Omega_{m0} \approx 0.27$ and $\Omega_{\Lambda 0} \approx 0.73$, the cumulative time since the Big Bang is:

$$t_0 \approx \frac{1}{H_0} \int_0^1 \frac{da}{a\sqrt{\Omega_{m0}/a^3 + \Omega_{\Lambda 0}}} = \frac{2\mathrm{Sinh}^{-1}\sqrt{\Omega_{\Lambda 0}/\Omega_{\mathrm{m0}}}}{3H_0\sqrt{\Omega_{\Lambda 0}}} = 13.8 \times 10^9 \mathrm{years}, \tag{1.6}$$

about 3 times the age of the Earth.

1.2 Remnant radiation from the Big Bang

When all the energy in the universe was concentrated in a tiny volume, the energy density must have been enormous; it must have been very hot. In 1946, George Gamow suggested that nuclear fusion must have taken place when the universe was so hot in the beginning [11]. Out of an initial sea of energetic protons and neutrons, this process, called the "Big Bang nucleosynthesis", would have created deuterium (nucleus made of one proton and one neutron) and helium as well as trace amounts of light elements like lithium and beryllium. In 1948, Gamow predicted that the radiation from the Big Bang nucleosynthesis must still be filling the universe [12]. He noted that the temperature at the time of deuterium formation must have been $\sim 10^9$ K (dissociation energy of deuterium nuclei) and based on the observed abundance of helium, he and his colleagues estimated that the temperature of this radiation would have lowered to only ∼1-10 K above absolute zero in the present universe [3]. Most theorists at that time, including them, thought that such radiation would be too weak to detect.

However in 1964, radio astronomers Arno Penzias and Robert Wilson were struggling to get rid of a constant background "noise" from their radio antenna signals [40]. Their efforts included catching pigeons that nested inside the horn-shaped antenna, and cleaning what they called "white dielectric material" produced by the pigeons on the antenna surface. After a year, they still could not remove the background noise. They learned that this constant signal was precisely uniform in every direction, whether they pointed the antenna toward the Sun or the Milky Way or the more empty parts of the sky. This meant that the signal was coming from even beyond our Galaxy, permeating throughout the universe; otherwise it would not be so uniform in all directions. The high degree of isotropy indicated that the signal originated very far away, or equivalently, very early in time. The source must have been enormously powerful for it to be detectable. Physicists immediately inferred that this must have been from the immense fireball of radiation at the Big Bang [8]. But how could we be sure that this was really what they were detecting? After all, they were observing only one small part of the frequency spectrum of radiation.

If the radiation was from the Big Bang, it would have a type of spectrum called the "blackbody" spectrum. Radiation has a blackbody spectrum if it is emitted by anything that absorbs and re-emits light freely but does not reflect it. According to the Big Bang model, the universe at the beginning must have been crowded with particles and radiation, and must have been very hot. In that environment, the particles were constantly bumping into light, absorbing and re-emitting it. With so much energetic radiation around, negatively charged electrons could not bind to positively charged protons without getting knocked off by photons. The universe was filled with hot plasma where free electrons kept scattering light. Radiation from such an environment would have a blackbody spectrum, and the spectrum's characteristic shape would have been preserved while the light traveled through the expanding space. In a blackbody spectrum, there is a contribution to the intensity at every wavelength. The amount of contribution varies continuously across the wavelengths in a characteristic way that depends only on the temperature of the emitting body. Therefore astronomers could verify that a spectrum is that of a blackbody by measuring the intensity of the radiation at different wavelengths.

During the 1970s, various groups observed the background radiation at various microwave and infrared wavelengths. They all confirmed that this radiation has a blackbody spectrum with a characteristic temperature of about 3 K. It has come to be called the cosmic microwave background (CMB) radiation. Relatively recently in 1991, a satellite observatory called *COBE* (Cosmic Background Explorer) made a precise measurement of the CMB from Earth's orbit and the data fit the blackbody spectrum perfectly (Figure 1.2).

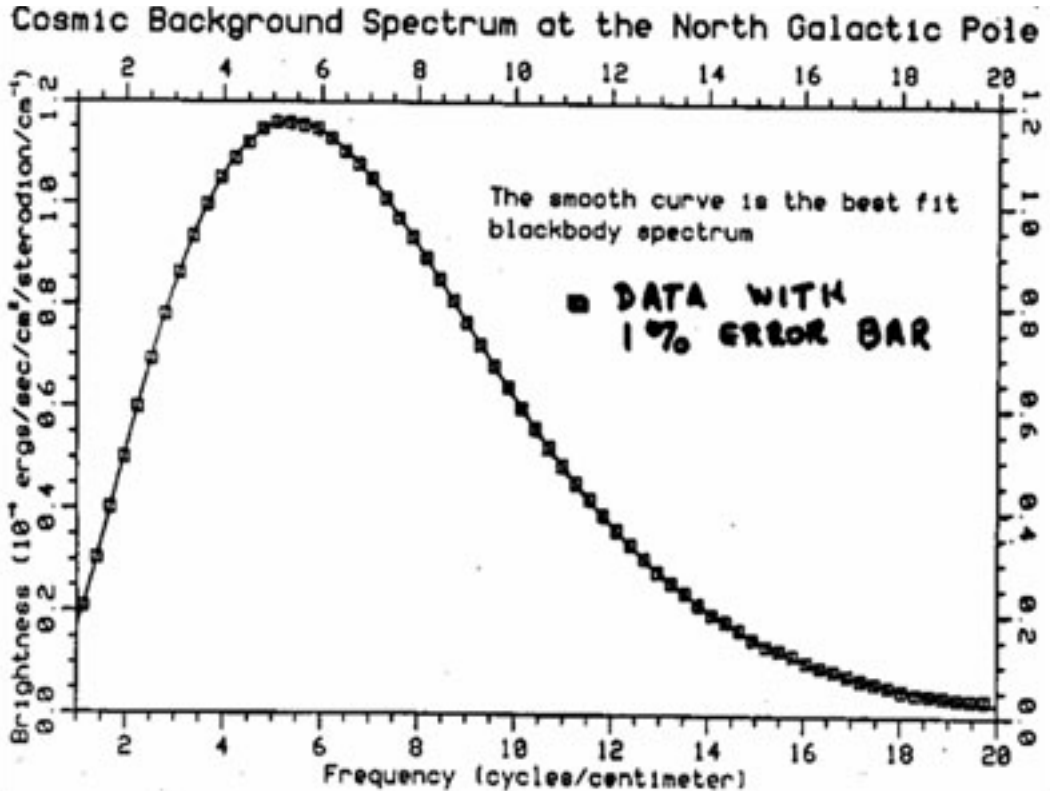

Figure 1.2: Blackbody spectrum of the CMB measured by *COBE* [34].

COBE measured the characteristic temperature of the CMB to be 2.73 K. This temperature is significantly lower than the original temperature of the radiation because the expanding universe stretched the wavelength by many factors, making it much less energetic. It took practically the entire age of the universe for the radiation to reach us. We now know that the expansion of the universe during this time stretched out the wavelength of the radiation by about 1000 fold. The afterglow of the Big Bang comes from when the universe was only about 400,000 years old when it cooled enough for electrons and protons to combine into hydrogen atoms. This makes the CMB radiation the oldest thing humans have ever observed; the universe was embryonic compared to its 14,000,000,000 year age. We are almost viewing the event of the Big Bang.

We can still "see" the leftover radiation from the Big Bang.[3] By studying the CMB radiation, along with other cosmological data sets, we learned that:

[3]In fact, about a % of the static you see on television when it's not tuned into any channel comes from the CMB! `http://background.uchicago.edu/~whu/beginners/properties.html`

* The universe began 13.8±0.1 billion years ago.
* The universe is expanding at a rate of 70±2 km/s/Mpc.
* The observable universe has no overall curvature; its geometry appears flat.
* The universe consists of: 73% dark energy, 23% cold dark matter, and 4% ordinary matter.
* The CMB radiation comes from 380,000 years after the Big Bang when the universe was 1090 times smaller.
* The first stars lit up 200 million years after the Big Bang.
* The average energy density of the universe today is equivalent to only 6 protons/m^3.
* The current temperature of the CMB radiation is 2.725±0.001 K.
* There are 410 photons / cm^3 left over from the Big Bang. (About a % of the TV snow)
* The universe will apparently expand forever.

1.3 Inflationary beginning of the Big Bang

Having learned that the universe began with the Big Bang, the next question is: *How did the Big Bang itself begin?* The early Big Bang theory itself also had some shortcomings, not able to explain why the CMB is so isotropic ("smoothness problem"), why the universe appears so close to having no global curvature ("flatness problem"), and why the universe has structures (like galaxies, galaxy clusters, and superclusters) instead of being uniform.

In 1981, Alan Guth came up with a scenario called "Inflation" to address the smoothness and flatness problems [14], a year later modified by Linde [31] and Albrecht & Steinhardt [2]. The idea was that the Big Bang began with a brief moment (less than 10^{-30} second) of enormous expansion, called inflation. The universe inflated so fast that one small region of it has blown up to be larger than our observable universe. Parts of the universe went away from each other faster than the speed of light. Also, space stretched so much that it came to look flat within our observable universe, just like the Earth is so large that it looks flat within the circle of visible area.

Inflation could also explain the origin of structures in the universe. Back in 1967, Sachs and Wolfe had predicted anisotropies in the CMB that would have evolved to cause the lumpiness in the present universe [46]. In 1992, the *COBE* observatory indeed detected such anisotropy in the CMB [49]. According to the inflation scenario, the origin of this inhomogeneity could have been the zero-point energy fluctuations in the vacuum, governed by quantum mechanics. Inflation is thought to have been driven by the potential energy of a scalar field called "inflaton" with a negative pressure. Right after the Big Bang, this inflaton potential energy dominated the total energy density of the universe and quantum fluctuations in the inflaton field gave rise to fluctuations in the energy density. Quantum

mechanical effects normally have little influence on large scales, but an exponential expansion of the universe during inflation could have stretched the quantum fluctuations by many orders of magnitude.

A typical model of inflation suggests that the potential energy of the scalar field drove rapid inflation of the universe between the cosmic times around $t = 10^{-35}$ s and $t = 10^{-33}$ s. During this short period, the causal horizon size (red line in Figure 1.3) did not have a chance to increase much at all, whereas the fabric of space and any comoving scales within it (blue line) expanded by tens of orders of magnitude. The expanding space stretched each Fourier modes of the quantum fluctuations past the causal horizon at the first purple point. After exiting the horizon (when $a(t) = ck/H$), the fluctuations no longer evolved quantum mechanically because their scales increased beyond causal connection. The fluctuations became frozen in to become super-horizon metric perturbations; they became a classical quantity after leaving the horizon. Much later, the horizon (the Hubble radius) expanded enough (at the second purple point) for the perturbations to begin growing. These density perturbations, through gravitational effects, are thought to have eventually resulted in the large-scale structures of the universe.

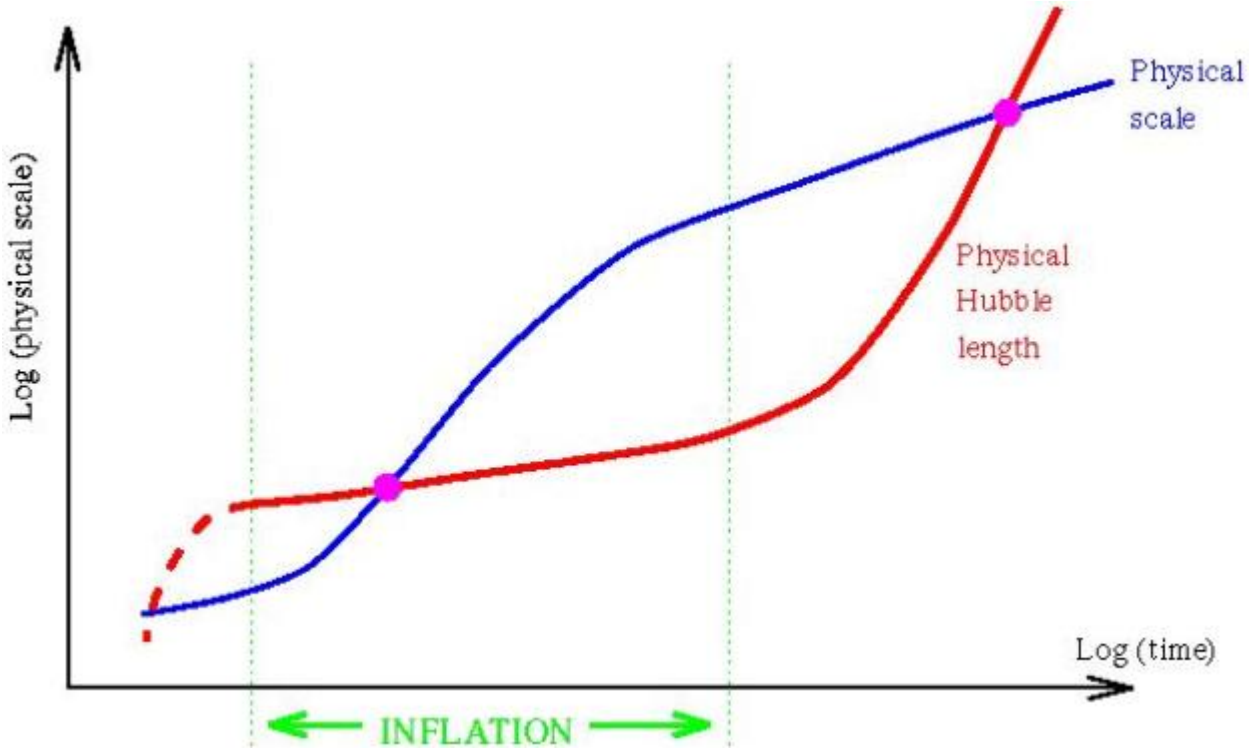

Figure 1.3: A comoving scale relative to the causal horizon size, during and after inflation, shown using physical coordinates [30].

1.4 Evidence for inflation

Inflation seems to be a great idea that has not been ruled out, but more direct evidence would increase our confidence about this. Moreover, if we could constrain the energy scale of inflation, we can begin to obtain clues about what kind of physics was responsible for this start of the Big Bang.

According to the observations of the CMB radiation, the perturbations seem to be ideally Gaussian (their Fourier modes are uncorrelated). This suggests that the perturbation has a quantum mechanical origin: each Fourier mode evolved independently of others like a quanta governed by the commutation relations. Also according to the CMB observations, the power spectrum seems to be ideally scale-invariant (the degree of fluctuations per decade in wavenumber is constant). Physically this is because the horizon size c/H was nearly constant as the Fourier components exited the horizon during inflation. Soon, the spectral index n, defined as in $P(k) \propto k^{n-1}$, could be measured with a precision of $\Delta n \sim 0.01$. The scale-invariance imply fractal-like structures, as might be observed in the large-scale structures of the universe. Finally, the observed distribution of galaxies and isotropy of the CMB suggest that the relative amplitude of the density perturbations should be $10^{-5} - 10^{-4}$.

Shortly after the theories of inflation were developed in the early 1980s, cosmologists predicted that inflation would have generated ripples in space, or gravitational waves.

1.4.1 Inflationary gravitational waves

Although inflation is mind-boggling, it is actually testable by observations. In 1982, Rubakov et al noted that inflation would have created gravitational waves and that they would have had effects on the CMB [44]. The amplitude of the gravitational waves is expected to be proportional to the expansion rate H during inflation, which in turn is proportional to the inflationary energy scale squared. Searching for them allows us to explore unimaginable energy scales near 10^{16} GeV, where the grand unified theory is thought to be in effect. Constraining the energy scale of inflation will help us better explore the physics of inflation. Relativity theory predicts gravitational waves, but they have never been directly detected yet. In 1985, Polnarev noted that the gravitational waves would have induced polarization in the CMB [41].

1.4.2 Cosmic microwave background polarization

The CMB radiation is polarized because it was scattered off of free electrons during matter-radiation decoupling. When an electromagnetic wave is incident on a free electron, the scattered wave is polarized perpendicular to the incidence direction. If the incident radiation were isotropic or had only a dipole variation, the scattered radiation would have no net polarization. However, if the incident radiation from perpendicular directions (separated by 90°) had different intensities, a net linear polarization would result (Figure 1.4). Such anisotropy is called "quadrupole" because the poles of anisotropy are $360°/4 = 90°$ apart.

At radiation decoupling when photons last scattered off of electrons, there was temperature inhomogeneity. When enough electrons bound to protons such that photons from hot

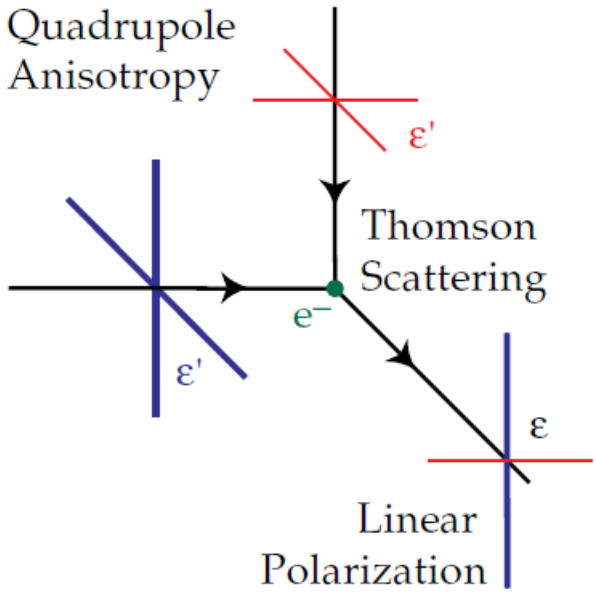

Figure 1.4: Thomson scattering of radiation with a quadrupole anisotropy generating polarization (thick lines represent hot and thin lines cold radiation) [18].

and cold regions could meet to be scattered by the same free electron, the scattered radiation was polarized. This photon diffusion into regions of different temperatures was possible only when the plasma became optically thin enough during hydrogen formation. Also, these diffused photons could scatter only while there were still free electrons left. Thus, polarized radiation could be produced only during a short period near the end of decoupling. Only about 10% of the CMB radiation is therefore polarized.

Free electrons at different locations would result in different polarization orientations and magnitudes. As observed today, the CMB polarization varies across the sky. The quadrupole anisotropies at decoupling are projected into CMB polarization pattern. Since photons could not travel too far, polarization does not vary much across very large angular scales.

The quadrupole anisotropy, which produced CMB polarization, could arise from 3 types of perturbations (Figure 1.5):

- Scalar: Energy density fluctuations in the plasma (resulting in hotter and colder regions) cause velocity distributions that are out of phase with the acoustic density mode. The fluid velocity from hot to colder regions causes blueshift of the photons, resulting in quadrupole anisotropy.

- Vector: Vorticity in the plasma induced by defects or strings cause Doppler shifts resulting in the quadrupole lobes in the figure. However, vorticity would have been damped by inflation and is expected to be negligible.

- Tensor: Gravitational waves stretch and squeeze space in orthogonal directions (as shown by the test circles in the figure). This also stretches the wavelength of radiation, therefore creating quadrupole variation in the incoming radiation temperature. Gravitational waves from inflation would be a tensor perturbation.

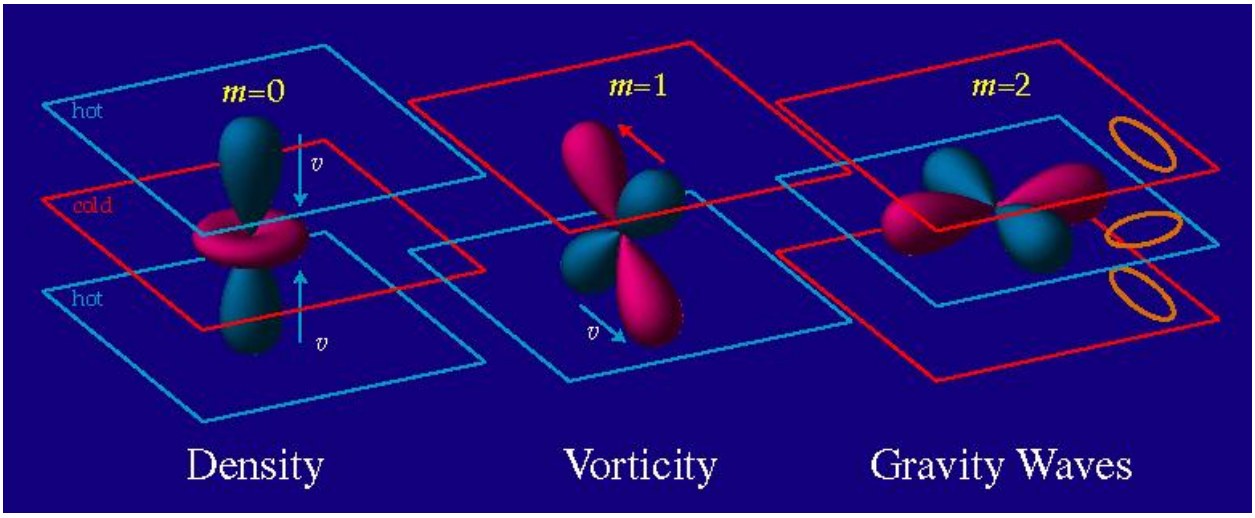

Figure 1.5: Three perturbation types resulting in quadrupole anisotropy that generates CMB polarization [18]. Lobes indicate the directions of the hot and cold photons. Planes represent the fluctuation in intensity of the underlying plane wave fluctuation.

1.4.3 Curl-mode polarization

We can decompose the polarization pattern on the sky into 2 components:

- Curl-free component, called "E-mode" (electric-field like) or "gradient-mode", with no handedness.
- Grad-free component, called "B-mode" (magnetic-field like) or "curl-mode", with handedness.

The E-mode may be due to both the scalar and tensor perturbations, but the B-mode is due to only vector or tensor perturbations because of their handedness.

Once we have maps of the E- and B- components (and the temperature anisotropy), we can analyze them by decomposing them in terms of spherical harmonics. For example, for temperature anisotropy $\Theta(\hat{\mathbf{n}}) = \Delta T/T$ where $\hat{\mathbf{n}}$ is the direction on the sky:

$$\Theta_{lm} = \int d\hat{\mathbf{n}} Y^*_{lm}(\hat{\mathbf{n}})\Theta(\hat{\mathbf{n}}). \tag{1.7}$$

We use the multipole moments Y_{lm} to define the various power spectra:

$$\langle E^*_{lm} E_{l'm'}\rangle = \delta_{ll'}\delta_{mm'} C_l^{EE}, \tag{1.8}$$
$$\langle B^*_{lm} B_{l'm'}\rangle = \delta_{ll'}\delta_{mm'} C_l^{BB}, \tag{1.9}$$
$$\langle \Theta^*_{lm} E_{l'm'}\rangle = \delta_{ll'}\delta_{mm'} C_l^{\Theta E}. \tag{1.10}$$

(The B-mode is not expected to correlate with E or Θ because of its handedness.) Each of these can be scaled to give a corresponding magnitude in temperature scale (Figure 1.6):

$$\Delta_T^2 \equiv \frac{l(l+1)}{2\pi} C_l T^2. \tag{1.11}$$

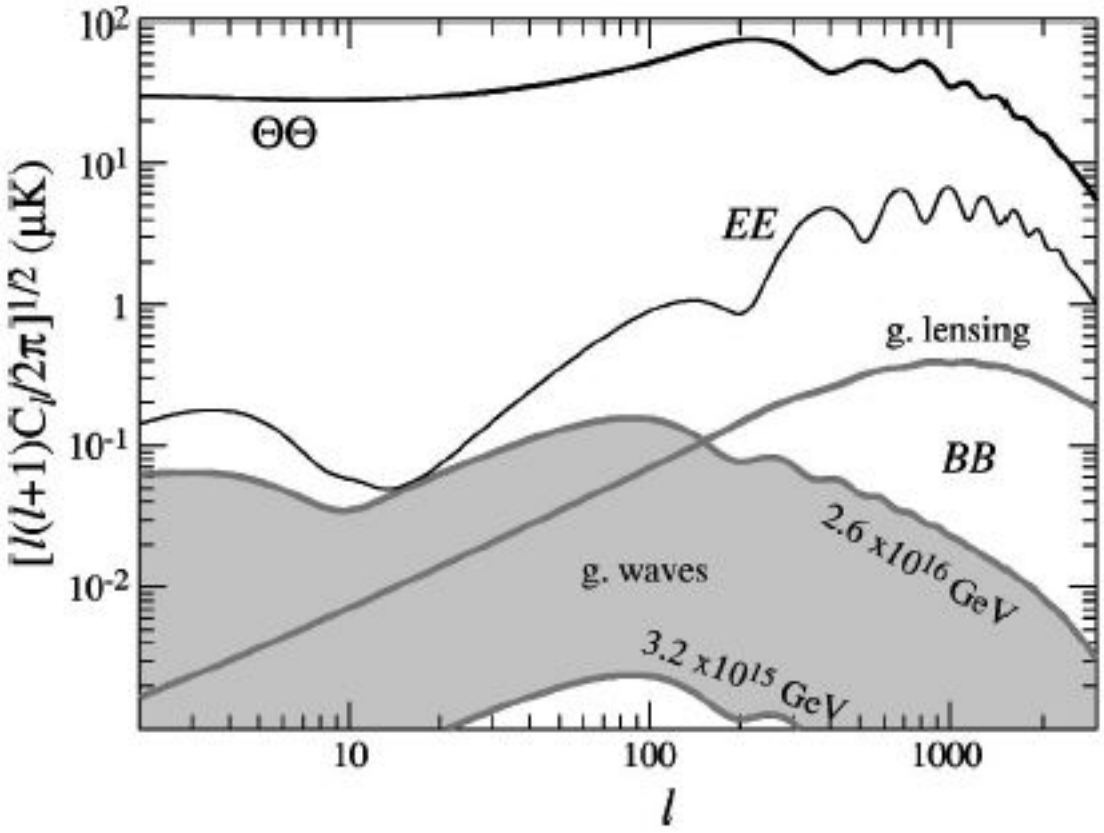

Figure 1.6: CMB angular power spectra [17]. (The multipole index ℓ corresponds to angular scales of $180°/\ell$.) The upper spectrum ($\Theta\Theta$) is temperature anisotropy, with amplitude 5 orders of magnitude smaller than the CMB temperature of 3 K. The polarization signals (EE, BB) are smaller by an additional 1–2 orders of magnitude because the polarized radiation was produced only near the end of decoupling. BB has two components: one due to gravitational lensing of EE by intervening large scale structures, and another due to inflationary gravitational waves. The polarization spectra decline at large angular scales (low ℓ) because photons could not travel so far before the end of decoupling. Since the E- and B- polarization modes come from different physics, the anisotropy spectra for the two components are expected to have different shapes and amplitudes.

Since the velocity gradients in the plasma (which is out of phase with the density fluctuations) produced the E-mode polarization, the polarization spectrum is directly out of phase with the temperature anisotropy spectrum. These two spectra are therefore correlated. The E-mode peaks around an angular scale corresponding to the photon mean free

path at decoupling. The E-mode was first detected in 2002 by DASI [26]. The signal level was consistent with the prediction based on the measured temperature anisotropy. TE correlation was first measured by *WMAP*, matching the predicted spectrum and showing the reionization signature [24]. Re-scattering of the CMB photons during reionization added to the polarization spectrum at large angular scales ($\ell < 10$). The observation indicated that reionization happened at redshift around z_r=11–30.

The most profound discovery will be the detection of B-mode polarization due to gravitational waves from inflation at the beginning of the universe. Based on *WMAP* data, all we know is that the energy scale of inflation must have been $< 2 \times 10^{16}$ GeV [25]. When we detect the gravitational wave signal, we will be able to find the energy scale of the very first major event less than 10^{-30} second after the creation of our universe.

Chapter 2

BICEP experiment concept

A strong indication of an inflationary origin of the universe would be a detection of the curl component ("B-mode") in the polarization of the CMB arising from gravitational wave perturbations [9]. This primordial B-mode polarization is expected to peak at angular scales of $\sim 2^\circ$, and the magnitude of the power spectrum is described by the ratio r of the initial tensor-to-scalar perturbation amplitudes, a quantity directly related to the energy scale of inflation. The best published upper limit is $r < 0.22$ at 95% confidence, derived from *WMAP* CMB temperature anisotropy measurements at large angular scales combined with constraints from Type Ia supernovae and baryon acoustic oscillations [25]. These temperature measurements have already reached the limit imposed by cosmic variance, and the CMB temperature based r constraints are also limited by a strong degeneracy with the scalar spectral index n_s. The inflationary B-mode spectrum, however, suffers little from cosmological parameter degeneracies at degree scales, and its amplitude depends primarily on r. Upper limits on the B-mode polarization amplitude, $\sqrt{\ell(\ell+1)C_\ell^{BB}/2\pi}$, of ~ 0.8 μK rms have been placed by *WMAP* at a multipole moment of $\ell \sim 65$ and by QUaD at $\ell \sim 200$, respectively [37, 43]. These limits are still well above the expected levels of confusion from either polarized Galactic foregrounds in the cleanest regions of the sky or from gravitational lensing that converts the much brighter CMB gradient ("E-mode") polarization to B-modes at smaller angular scales.

Bicep (Background Imaging of Cosmic Extragalactic Polarization) is an instrument designed to target the expected peak of the gravitational-wave signature at angular scales around 2°. Using proven bolometric technologies and selecting the cleanest available field for observation, this instrument was designed, given sufficient observation time, to be capable of measuring a polarization signal of 0.08 μK rms at $\ell \sim 100$ corresponding to the BB signal expected for a tensor-to-scalar ratio of r=0.1.

We began our telescope installation work at the South Pole in November 2005, cooled down the cryostat in December, and captured first astronomical light a month later. Following calibration measurements and tests of the observing strategy, Bicep began CMB observations in February 2006. The instrument operated nearly continuously until the end of the experiment in December 2008.

The rest of this chapter gives an overview of the instrument and the observing strategy, also described in [51, 21].

2.1 Design summary

The goal of targeting the sub-μK B-mode polarization signal that peaks at $\sim 2^\circ$ angular scales led to an experiment design specifically optimized for sensitivity and control of systematic errors. BICEP (Figure 2.1) was a compact on-axis refractor with 49 pairs of polarization-sensitive bolometers (PSBs) [20] operating in atmospheric transmission windows near the CMB peak at 100 and 150 GHz with 0.9° and 0.6° beams, respectively (Table 2.1). We observed in two main frequency bands to differentiate between the spectra of CMB anisotropies and of potential Galactic foreground contamination.[1] We chose the Amundsen-Scott South Pole Station, at an elevation of 2800 meters, for its atmospheric transparency, stable weather, and constant availability of the best observing field on the sky. Achieving one-degree resolution at 2–3 mm wavelengths requires only a 25-cm aperture, which is compatible with a compact forebaffle and simple implementation of calibration measurements.

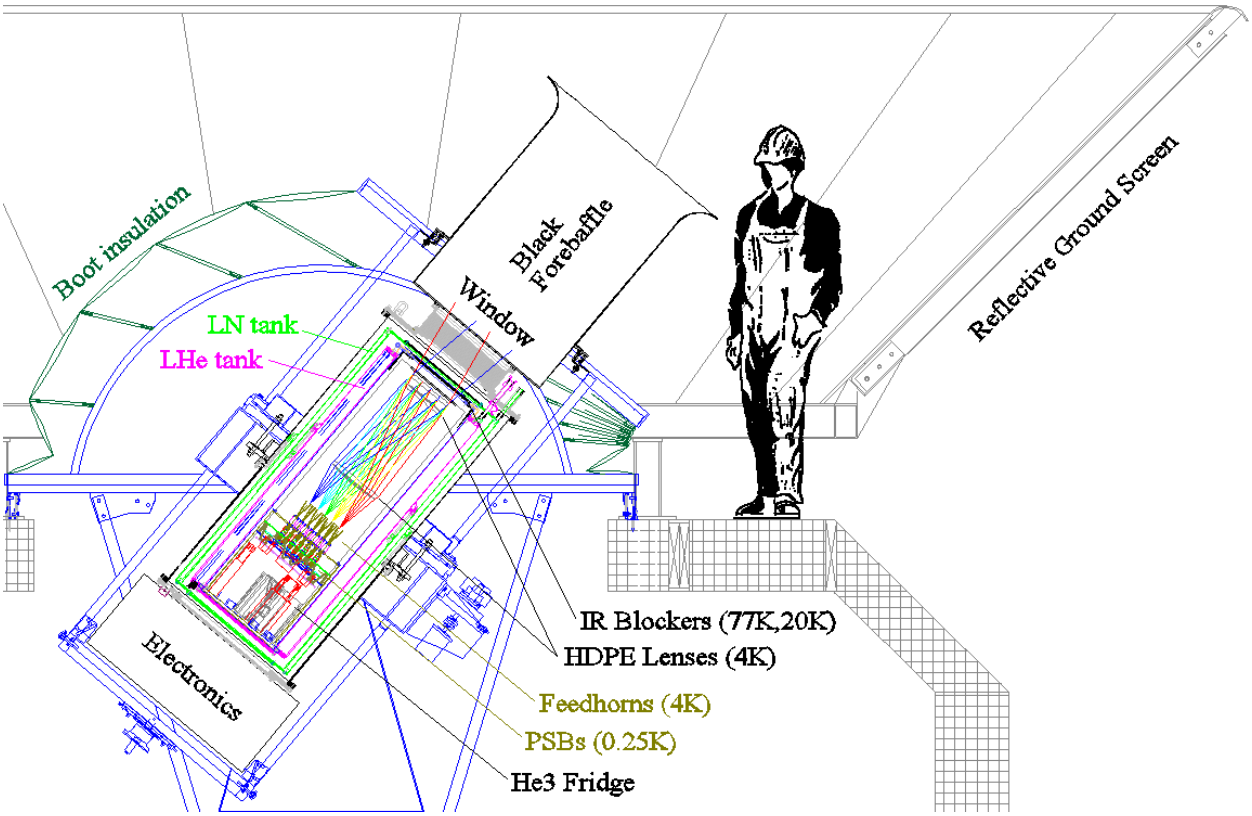

Figure 2.1: BICEP telescope on a 3-axis mount at its lowest elevation limit of 50°, looking out through the roof of the Dark Sector Laboratory (DSL) building located 800 meters from the geographic South Pole. A cryostat with toroidal liquid nitrogen and liquid helium tanks encloses the entire 4 K optics, including two high-density polyethylene lenses and corrugated feedhorns. The polarization-sensitive bolometers are cooled with a ^{4}He/^{3}He/^{3}He adsorption refrigerator to 250 mK.

[1] We later added two PSB pairs at 220 GHz for further Galactic studies.

The bolometers use neutron transmutation doped (NTD) germanium thermistors to measure the optical power incident on a polarization-sensitive absorber mesh. After adjusting for relative responsivities, orthogonal PSBs within a pair are summed or differenced to obtain temperature or polarization measurements. Because the orthogonal PSBs detect the CMB through the same optical path and atmospheric column with nearly identical spectral passbands, systematic contributions to the polarization are minimized. A detailed description of the BICEP instrument is in Ki Won's thesis [52].

Table 2.1: BICEP instrument summary

Band Center	Band Width	Beam FWHM[a]	PSBs	NET[b] per detector
96.0 GHz	22.3 GHz	0.93°	50	530 $\mu K_{CMB}\sqrt{s}$
150.1 GHz	39.4 GHz	0.60°	48[c]	450 $\mu K_{CMB}\sqrt{s}$

[a] Full width at half maximum, average over all the beams.

[b] Noise equivalent temperature; see §5.4.

[c] After the first year, we converted two of the 150 GHz pairs to 220 GHz.

2.2 South Pole site

We chose the South Pole station as the telescope site, located on the ice plateau of Antarctica at an altitude of 2800 m. The extremely dry and stable sky above the South Pole results in 150 GHz opacity τ of 0.03–0.04. The South Pole station is one of the best available sites on Earth for millimeter-wave observation, offering low humidity, stable atmospheric conditions, and excellent infrastructure. The telescope was located in the Dark Sector Laboratory (89.99° S, 44.65° W).

The South Pole site also makes it possible to track a given field continuously at constant elevation angle. The sky that is accessible for observation from the Pole includes some of the largest regions of minimal Galactic foreground emission on the celestial sphere. These characteristics of the South Pole make it the ideal location for the long, deep integrations needed to study the CMB polarization signal. BICEP is designed to exploit these advantages in the course of long integrations on selected fields. The design of the telescope also reflects the particular environmental challenges at the South Pole. During the 6 months of the year when the Sun (the strongest contamination source) is below the horizon, presenting optimal observing conditions, the average ambient temperature is -60 °C. Very long integration times demand a design that can ensure reliable telescope performance during this period.

Antarctica is the most remote continent on Earth, with no permanent inhabitants. No part of it was sighted until the 1820s. It is a continent roughly 4000 km across (comparable to the Moon's 3500-km diameter). The first time a human reached the South Pole was in 1911; however, 45 years had elapsed before humans returned to the Pole and set up what has today become a vibrant research base. Since the 1950s, numerous countries have established stations across the continent, overcoming many challenges similar to those involved in space exploration. Today, there are over 100 Antarctic research facilities by 28 countries, with summer and winter populations of roughly 4000 and 1000, respectively.

Among the various fields of research, astrophysics finds many advantages in Antarctica. The continent hosts many observatories, including neutrino detectors and telescopes at various wavelengths. Being at such a remote location, the site is devoid of unwanted interference. Especially during the 6 months at the South Pole, the Sun stays below the horizon, providing an extended period of ideal observing conditions. To fully take advantage of this unique condition, observatories like BICEP are situated in the "Dark Sector", designated to be free of radio transmitters (Figure 2.2). Being on the rotation axis, the polar locations allow uninterrupted observation of astronomical targets in the constantly available sky.

Figure 2.2: South Pole Dark Sector and LC-130. (Photo by Steffen Richter)

The South Pole experiences temperatures lower than -70 °C, not far from the freezing point of carbon dioxide (-78.5 °C). This required designing instruments capable of operating at such low temperatures. We chose to enclose most of the instrument in a room-temperature air space, exposing only the telescope aperture and the baffle surrounding it. A flexible bellows was used as an environmental seal that permits telescope motion.

Difficult transportation, scarce resources, limited communications, and lack of developed infrastructure have all made Antarctic operations nontrivial and risky. The South Pole was initially an endless desolation, where going there – let alone working there – seemed daunting. However, since 1956, the United States has constructed and maintained a permanent station that today has an impressive infrastructure.

Today, going to the South Pole typically takes about 3 days. With the United States Antarctic Program, a passenger first goes to Christchurch, New Zealand at least a day before the Antarctic flight to prepare all the extreme cold weather gear and ensure that the total mass, including that of the passenger, is within the limit. From New Zealand, passengers typically fly to Antarctica on a jet cargo aircraft C-17 along with up to 77 tons of cargo. The flight is about 5 hours to the coastal McMurdo station, where we stay overnight for another flight to the Pole the next day. Flights between McMurdo and the Pole are on ski-equipped LC-130 propeller aircraft, whose hydraulic fluid for landing gear is rated for temperatures only above -50 °C. This prohibits any flights in and out of the South Pole Station from mid-February to the end of October. The limited accessibility requires careful planning of all the necessary items and contingencies.

Being at such a remote location, communication with the rest of the Earth is a major challenge. The South Pole Station uses three old geostationary satellites (*TDRS, MARISAT, GOES*) that have wobbled off of their original orbits enough to be visible from the Pole for several hours a day. Together, they provide 11.5 hours a day of data link, allowing ∼15 GB/day of data transfer at 5 MB/s as well as 5–35 KB/s internet connection.[2] Additionally, the *Iridium* satellites are used to transfer electronic mail throughout the day and for emergency telephone connection. BICEP transferred 3.5 GB/day of data to California.

2.3 Instrument

The BICEP receiver consists of a two-lens telescope coupled to a focal plane of 49 orthogonal pairs of polarization-sensitive bolometers (PSBs) [20]. The beam width at 100 and 150 GHz is 0.93° and 0.60°, respectively. The entire focal plane and optics assembly is housed in a cryostat with toroidal liquid nitrogen (LN_2) and liquid helium (LHe) tanks. The clean optical path and azimuthal symmetry minimize instrumental polarization.

Table 2.2: Number of detector pairs for each observing year

	2006	2007/2008
100 GHz bolometers	25 (19 unflagged)	25 (22 unflagged)
150 GHz bolometers	24 (14 unflagged)	22 (15 unflagged)
220 GHz bolometers	0	2
Dark bolometers	6	6
Thermistors	6	8
Resistors (5 MΩ)	6	5

In addition to bolometers behind feedhorns, along the perimeter of the focal plane are "dark" bolometers not coupled to radiation, un-etched modules used as thermistors, and fixed resistors for diagnostic purposes.

2.3.1 Polarization sensitive bolometers

BICEP measures radiation with orthogonal pairs of silicon nitride micro-mesh polarization sensitive bolometers (PSBs, Figure 2.3) [20]. The incident optical power is measured as a temperature change in the absorber sensed by measuring the resistance of the neutron transmutation-doped germanium (NTD Ge) thermistor: $R(T) = R_0 e^{-\sqrt{\Delta/T}}$, where typically $R_0 = 100\ \Omega$ and $\Delta = 42$ K. Because of its wide bandwidth, the same bolometer design works for both 100 and 150 GHz bands, in detector housings tuned for band-specific $\lambda/4$ backshort. PSBs are cooled to 250 mK to achieve background-limited sensitivities. After adjusting for the relative responsivities, we sum or difference the pair signals to measure the total intensity or polarization. Because the orthogonal PSBs measure the CMB through the same optical path and atmospheric column with nearly identical spectral pass bands, systematic errors in polarization measurements are minimized.

[2] *MARISAT* was deorbited in October 2008, reducing the data link period to 9.5 hr/day.

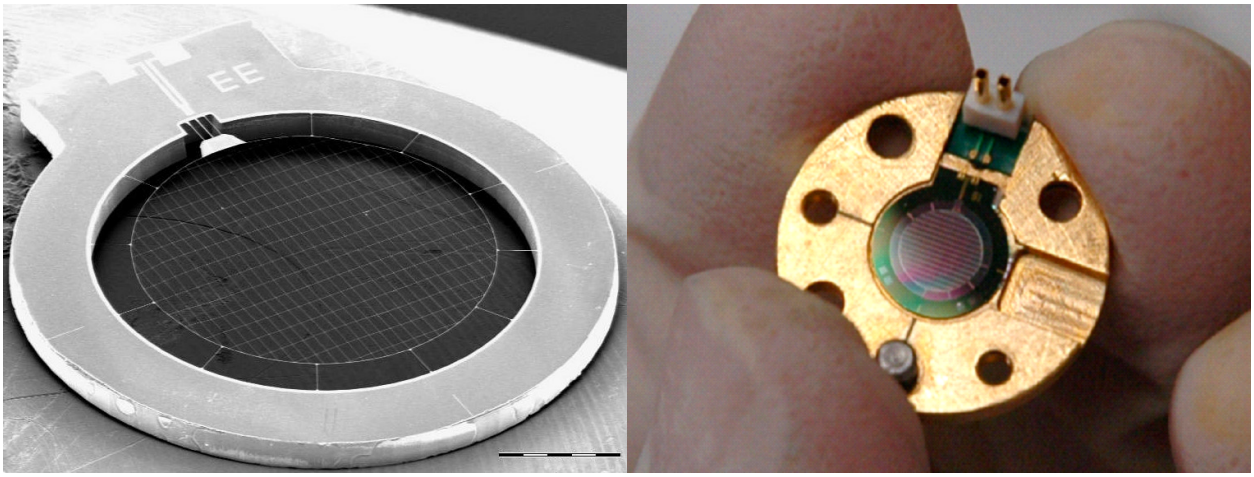

Figure 2.3: A polarization-sensitive bolometer used by BICEP, designed for minimum cross section to cosmic rays. The 4.5-mm diameter grid is etched from a Si_3N_4 layer for rigidity of the suspended structure, and the longitudinal lines spaced at 0.15 mm has gold deposited for polarization sensitivity. The perimeter is also metalized to conduct the absorbed energy to the NTD Ge thermistor at the edge of the absorber, placed outside the coupling area to the incoming waves to minimize cross polarization response. The trimmable legs on either side of the central signal leads allow for tuning of the thermal conductance to the 250 mK bath, depending on expected total loading on the bolometer.

When properly tuned, NTD Ge bolometers can offer background photon noise limited sensitivity in low loading conditions. We adjust the thermal conductance G between the thermistor and the 250 mK bath for the expected total loading to limit phonon noise. The conductance is dominated by the signal leads and a pair of adjacent metalized legs, which can be laser-trimmed to change the final conductance to $\{40, 50, 67\}\%$ of its maximum value. With high optical efficiencies (and thus higher fractional photon noise contribution), a wide range of G is acceptable for low-noise performance. With a degraded optical efficiency, however, we must adjust the thermal conductance for maximum sensitivity. Based on achieved optical efficiency during testing and expected atmospheric loading for observing conditions, we trimmed both of the adjustment legs to tune the PSB thermal conductance to $G \approx 60$ pW/K at 300 mK for both bands.

Bolometer's optical time constant $\tau \sim C/G$ determines the maximum desirable scanning speed $\approx \theta_{\rm FWHM}/3\tau_{\rm MAX}$. Single-pole equivalent median τ was measured to be 21 ms, with 97% of the bolometers under 45 ms. This allows for azimuth scanning at up to 5°/s without significant signal smearing.

Several CMB experiments have used PSBs. Detectors similar in design were used in the 2003 flight of BOOMERANG at 145 GHz [33], providing the first bolometric measurement of CMB polarization. PSB modules identical to BICEP's have been used in QUAD [15], targeting CMB polarization at an order of magnitude smaller angular scales. In addition, *Planck* mission's High Frequency Instrument (HFI) incorporates 4 PSB pairs at each of 100, 143, 217, and 353 GHz bands.

A PSB pair can be installed in either boresight "Q" or "U" orientation on the focal plane, defined with respect to the radius from the center (Figure 2.4). We chose the PSB layout such that a 180° rotation about the boresight completely exchanges the polarization coverage on the sky.

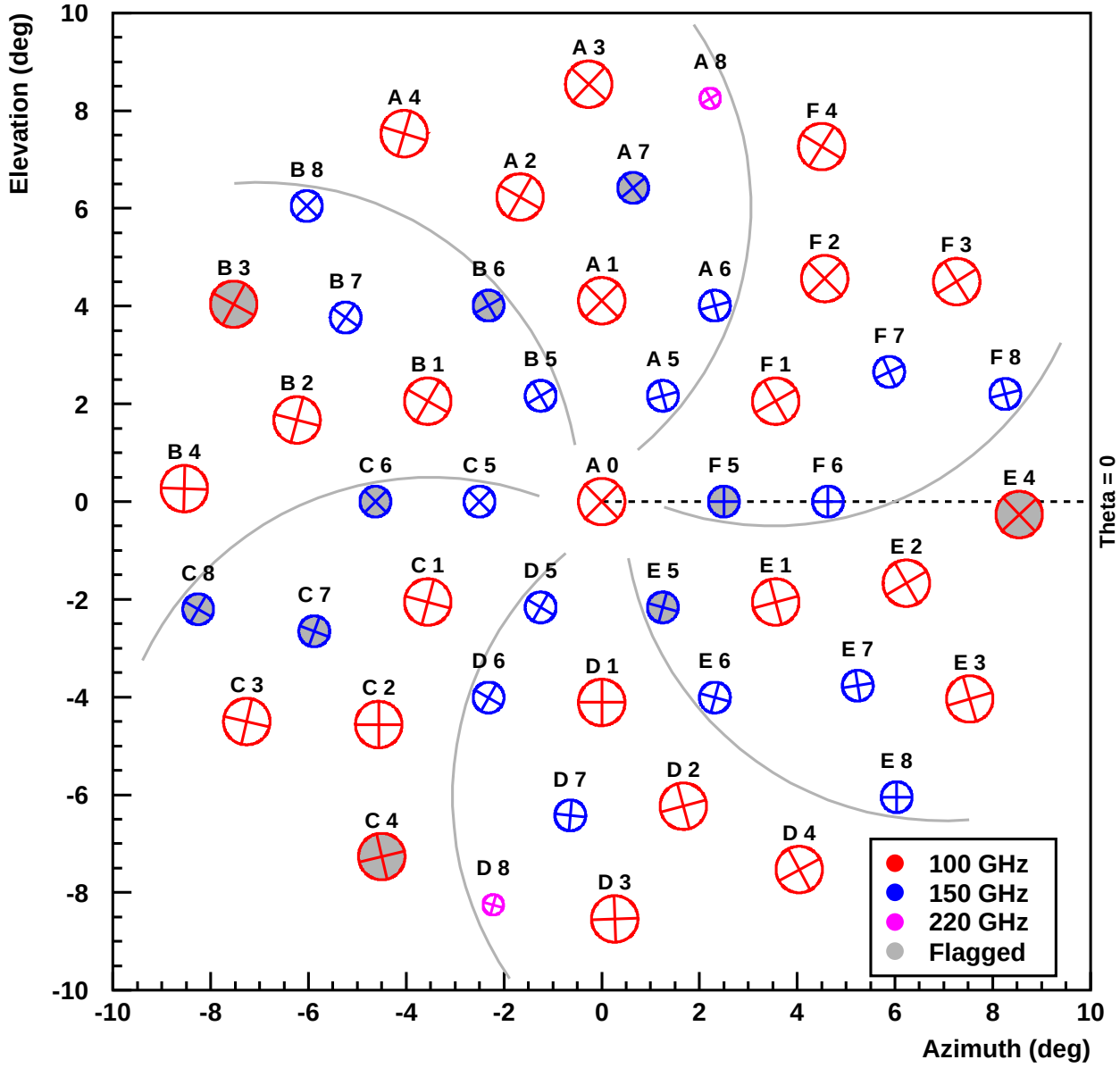

Figure 2.4: 2007/2008 layout of the BICEP beams with nominal locations, FWHM, and polarization orientations. There are six sectors (separated by gray curves) having alternating "Q" or "U" PSB orientations with respect to the center. BICEP observed with focal plane orientations of $-45°, 0°, 135°$, and 180° counterclockwise about the boresight, providing two independent and complete polarization coverage of the field to allow jackknife tests. A 180° boresight rotation provides complete coverage of Q and U Stokes parameters on the sky at each beam location.

At the end of the first year, in November 2006, we added prototype 220 GHz feedhorns in place of two of the 150 GHz ones along with the appropriate filters. We also replaced four bolometers because of their slow temporal response, high noise level, or poor polarization efficiency. We have omitted these and other problematic PSB pairs from CMB analysis for each observing year. After this refurbishment, BICEP remained cold and operated without interruption until the completion of observations in December 2008.

A printed circuit board on the backside of the detector focal plane routes the individual PSBs of each sector to the six load resistor modules on the perimeter for readout by the JFET amplifier stage. The entire focal plane, from the 4 K back-to-back throat section down to the output of the JFET modules, resides within a tightly sealed Faraday cage, preventing any stray radiation from coupling to the bolometers.

The focal plane is cooled to 250 mK by a 3-stage ^{4}He/^{3}He/^{3}He adsorption refrigerator filled with 32/16/2 L (STP) of gas (Figure 3.14). We automated the cycling of the refrigerator via the control system, and it takes $\sim$5 hours to reach 250 mK from the 4 K starting point. At the 2800-m altitude South Pole, where LHe temperature is 3.8 K, the hold time at the operating temperature is $\sim$65 hours. The refrigerator is cycled every 48 sidereal hours, providing an 89% duty cycle.

2.3.2 Filters and feedhorns

In front of the bolometers are low-pass metal mesh filters and beam-defining feedhorns, designed to couple the incoming radiation to the bolometers with high polarization fidelity and optical efficiency, as well as well-defined spectral pass bands (Figure 2.5). The filter sets the short wavelength edge of the spectral pass band while the feedhorn's waveguide cut-off sets the long wavelength edge.

The metal mesh photolithographed on a dielectric substrate blocks frequencies higher than a cut-off set by the grid size [1]. The filters have leaks at multiples of the cut-off frequency, so we stacked several filters with different cut-offs. Since atmospheric emission increases quickly with frequency, even small leaks can cause pair relative gain errors and excess optical loading. BICEP used edge-defining filters with cut-off frequencies of 109 and 177 GHz for 100 and 150 GHz bands, respectively, along with 2 additional blocking filters with slightly higher cut-offs for each band.

The design of the throat section of the feedhorns directly influences the allowed modes of electromagnetic propagation, affecting the illumination pattern and polarization characteristics of the beams on the sky. The throat sections of the PSB feedhorns define the lower edges of the bands. The design cut-ons were placed at 83 and 130 GHz for the two bands. The aperture diameters of the primary feedhorns were simply the largest that still allowed for the detector density to be driven by the minimum achievable size of the PSB modules. The minimum achievable feedhorn aperture diameter was 14 mm at 150 GHz, giving 21 mm at 100 GHz by direct scaling to keep the aperture illumination the same for both bands.

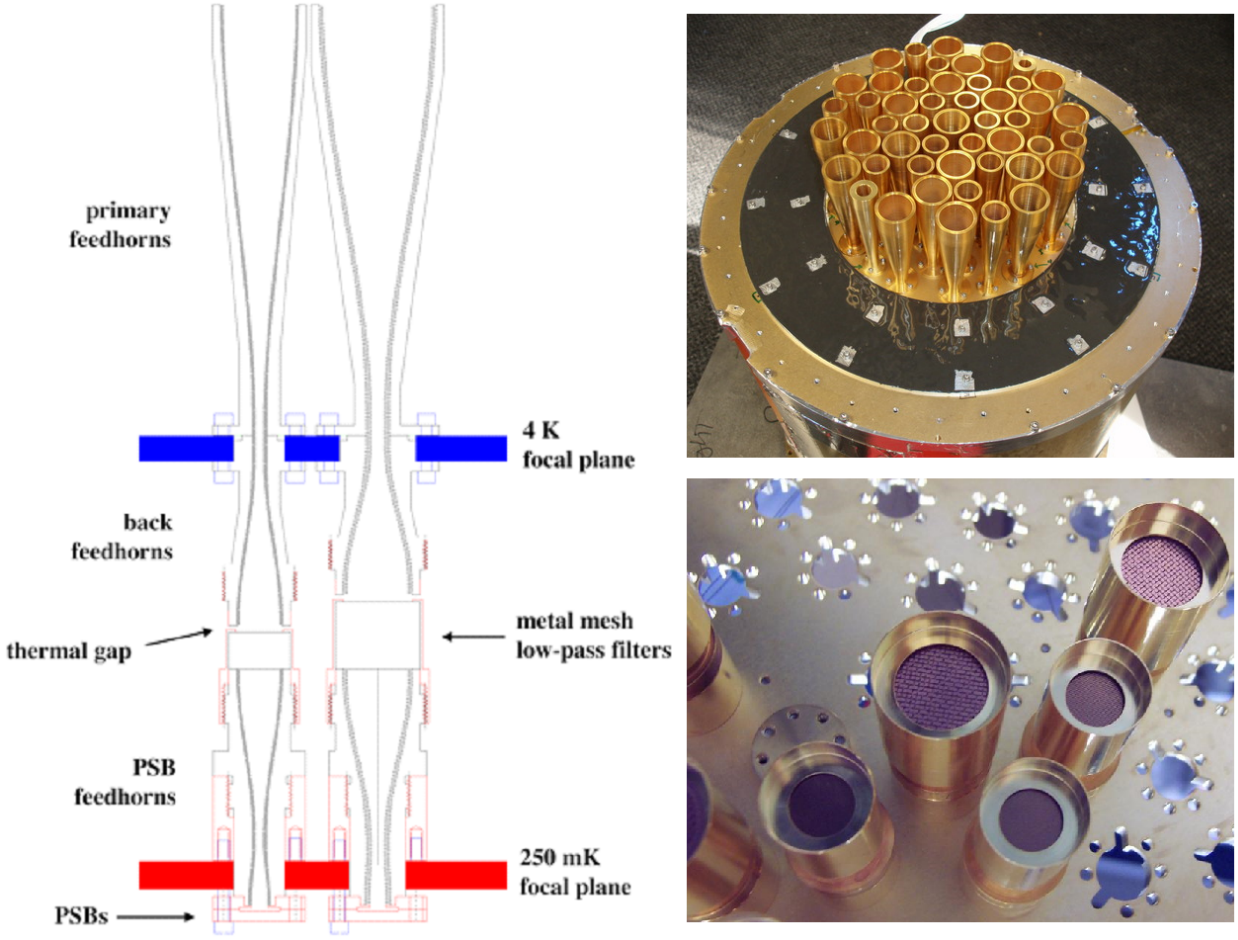

Figure 2.5: Feed configuration (left, by Ki Won), with low-pass filters (bottom) and profiled corrugated feedhorns (top). Each feed consists of 4 K primary and re-expanding feedhorns, followed by a small thermal gap to the 250 mK low-pass filter stack and a PSB coupling feedhorn. This arrangement separates the design considerations between band and beam definitions, and is similar to that used in ACBAR, BOOMERANG, and *Planck* HFI.

2.3.3 Cold HDPE lenses

The incoming radiation is focused onto the feedhorns with 2 biconvex lenses at 4 K, with the top objective lens providing the 25-cm aperture stop for degree-scale resolution.

BICEP's axisymmetric refractive optical design eliminates potential polarization contaminations associated with off-axis designs or on-axis secondary mirror structures. Because the entire optics is internal to the cryostat and cooled to cryogenic temperatures, instrument optical loading is minimized and is dominated by the ambient temperature vacuum window. The measured upper limit on the instrument loading was $<$ 4-5 K_{RJ}, consistent with the expected loading of 3.5 K_{RJ} in both frequency bands.

The positions and focal lengths of the two lenses (4 parameters) were chosen to provide telecentricity for a flat focal plane, focus at infinity, and the entrance pupil at the top lens (3

constraints). The remaining degree of freedom was chosen to minimize optical aberrations. A -20 dB edge taper of the primary feedhorn beams at the main aperture was chosen to minimize far-field sidelobes and loss from internal spill over. With the feedhorn aperture diameters constrained by the efficient packing density of the detector modules on the focal plane, this edge taper required an effective focal ratio of $f/2.3$ for the lenses. The plate scale of the focal plane was then $1/fd_{\rm A} \approx 1^\circ/{\rm cm}$ where $d_{\rm A}$ is the diameter of the main aperture. The 170 mm diameter focal plane covered a 17° region on the sky.

High-density polyethylene (HDPE) was chosen for the lenses over other candidates like silicon and fused silica because of low reflection loss and machining ease. The refractive index was measured to be 1.57 at cryogenic temperatures. Both sides of the lenses were anti-reflection coated with Zitex, using a technique described in the next section for coating the infrared blockers. Physical optics simulations on the design predicted a cross polarization of order 10^{-5} over the field of view, and induced linear polarization at the edge of the field of 0.8% without the anti-reflection coatings, and less with the coatings.

Figure 2.6: Optics tube housing two lenses at 4 K. Flexible braided copper straps were attached from the lenses to the 4 K base of the telescope enclosure for heat sinking, and the LHe vapor-cooled Teflon filter minimized the incident radiation. The edge of the top lens was measured to equilibrate at <8 K so negligible emission was expected from the lenses. Circular apertures located at the lenses and in two intermediate locations within the telescope were blackened with epoxy loaded with carbon black or iron filings to minimize stray light.

2.3.4 Infrared blockers

To keep the lenses cold and the thermal loading on the LHe stage low, BICEP used two infrared blockers in front of the objective lens, one cooled to 20 K with LHe boil-off vapor, and another attached to the 77 K LN_2 stage.

Application as an absorptive infrared-blocking filter ideally requires effective blocking above 3 THz, high thermal conductivity to dissipate absorbed energy to the edge, low refractive index or ease of anti-reflection coating, and good in-band transmission. Attenuation below 3 THz provides negligible mitigation of the thermal loading onto 4 K. We chose PTFE (Teflon) for its low in-band loss, a relatively low refractive index, and a thermal conductivity sufficient to dissipate the expected absorbed radiation to avoid excess heating of the filters beyond their usefulness. Its infrared attenuation properties are excellent with negligible transmission beyond 3 THz. Teflon blockers of thicknesses 1.5 cm and 2.0 cm were used at the 77 K and 20 K stage, respectively.

Since Teflon incurs ∼3% reflection per surface, we coated the blockers with a porous Teflon sheet, Zitex, which is available in many thicknesses and densities. Zitex has a typical refractive index of $n = 1.2$ (compared to ∼1.4 for regular Teflon), making it ideal for anti-reflection coating. Each surface used a single layer of Zitex to achieve good transmission over both 100 and 150 GHz bands, with ∼0.5% reflection per surface. We bonded the Zitex layers to Teflon by press-heating them together with a 50-μm low density polyethylene film in-between that melts at 120 °C. With the two Teflon blockers installed, the quiescent loading was expected to equate to 15 L/day of LHe consumption, compared to measured 10 L/day when the cryostat was blanked off.

The entire assembly described so far was enclosed in a LHe/LN_2 cryostat. The 110-L toroidal LHe tank conductively cooled the receiver via a single bolt circle at its base and surrounded the refracting optics. Thermal loading on the LHe consisted of 0.25 W from the refrigerator's parasitic losses, 0.1 W from the large optical aperture, and 45 mW from the JFET amplifiers. This resulted in a hold time of 4+ days in the field, while the 55-L toroidal LN_2 tank had a hold time of 3 days.

2.3.5 Readout electronics

Each bolometer is read out by AC biasing it at 100 Hz across two 20 MΩ load resistors in series and demodulating the signal, eliminating $1/f$ electronics noise above 0.01 Hz. The signals from the high impedance bolometers are immediately directed into JFET amplifiers, operating at ∼120 K, protecting the bolometers from electromagnetic interference. The output exits the 4 K radio-frequency tight cage through radio-frequency filtered connectors and is routed inside another cage at room temperature to pre-amplifiers that applies a gain of 200. The amplified signal is then low-pass filtered to prevent aliasing before being digitized. The digitized signal is multiplied by sine and cosine synchronized to the bolometer bias, averaged, and filtered using a digital Gaussian finite impulse response filter. The demodulated signals from all the bolometers are converted into an optical fiber signal and sent to the acquisition computer through a boresight axis slip ring.

2.4 Galactic foregrounds and sky coverage

The continuous visibility of the target field from the South Pole enables uninterrupted observation and deep integration. The mount is capable of observing down to a boresight elevation of 50°, providing access to the minimum foreground regions available from the South Pole. We selected as our primary CMB field an 800 deg^2 region of low dust emission outlined in Figure 2.8, in a right ascension and declination range of roughly $|\alpha| < 4$ hr and $-70° < \delta < -50°$. BICEP spent 18 hours per day on this field.

Polarized emission from our Galaxy will likely set the ultimate limit to detecting primordial B-mode polarization at large angular scales. The two dominant components of the diffuse polarized foreground emission are synchrotron radiation and Galactic dust. Galactic emission at frequencies below 90 GHz is generally dominated by synchrotron and free-free mechanisms in ionized gas, which decreases with frequency. Above 90 GHz, it is dominated by thermal emission from vibrational and rotational modes of dust. In typical high-Galactic latitude regions, the sum of synchrotron and dust contributions has a minimum around 60-100 GHz.

Synchrotron radiation comes from relativistic electrons spiraling in Galactic magnetic fields, and is polarized. The emission goes approximately as ν^{β_s} (in Rayleigh-Jeans temperature), where β_s is around -3 and varies spatially, generally steepening toward high Galactic latitudes and high frequencies. *WMAP* measurements characterized the emission by $\beta_s = -3.0$ and an angular power spectrum falling toward small scales as $\sim \ell^{-0.6}$ [39]. Free-free emission is intrinsically unpolarized, although rescattering by the electrons in H_{II} regions can make the cloud edges appear polarized. Still, the effect would be small compared to other galactic emissions.

Dust emission is thermal and can be polarized due to alignment of the dipole moment of the dust grains with the Galactic magnetic field. The dust emissivity does not seem to follow a simple power law in frequency, and a single temperature does not seem to describe it well. For example, the most widely used template for unpolarized dust emission is FDS model 8, a two-component model fit to IRAS, DIRBE, and FIRAS data [10]. They interpret the components as ∼100 nm silicate grains and ∼10 nm graphite grains with average temperatures of about 9 K and 16 K, respectively. However, the dust emission is not well understood: the model used data limited in frequency, and the fit accuracies varied over the sky. Although FDS is likely not a perfectly accurate physical model, measurements by *Archeops* and BOOMERANG matched the FDS template in typical high-Galactic latitude regions to 20% precision at 350 GHz and $\lesssim$30% precision at 245 GHz, respectively [42, 36]. The polarization properties of the dust are even less understood, but we can estimate the polarized emission from FDS model intensity and polarization orientations derived from observations of dust-polarized starlight. *Archeops* was able to measure the polarization fraction of several extended dust clouds near the Galactic plane. These clouds, believed to be representative of those at higher latitudes, exhibited polarization fractions of 5–10% [42]. *WMAP* data indicated a maximum fractional polarization of ≈5% and polarized dust emission also falling as $\sim \ell^{-0.6}$ toward small angular scales.

Given adequate sensitivity, the optimum sky coverage for detecting the gravitational wave signature is a sufficiently large one that minimizes B-mode polarization from Galactic

foregrounds. Galactic foregrounds vary significantly in intensity over the sky, especially for the dust emission. The larger the observing field, the more difficult it is to find a clean patch. We therefore restricted the target CMB field to ∼2% of the sky (800 deg^2) that is among the lowest in Galactic foregrounds available of that size over the entire sky, and the best region accessible from the South Pole. Using the FDS dust brightness model with an assumed uniform 5% polarization fraction, and the *WMAP* K-band polarized intensity map extrapolated to 150 GHz as an indicator for the synchrotron emission, we selected a region with the lowest angular power spectra contributions from both dust and synchrotron foreground polarization (Figure 2.7). The angular power spectrum of dust emission at ℓ=30–100 in this region was >100× lower than the median over the sky. With the above assumptions, the B-mode contamination at 150 GHz from dust emission for this region was expected at the level of r∼0.02, well below BICEP's target. Synchrotron B-mode in this field was too faint to be well-constrained by existing data; the *WMAP* 23 GHz signal in this region only marginally exceeds the noise floor, but implies a level comparable to the dust foreground at 150 GHz, assuming a spectral index -3.0. This region in the sky thus offers a window for the extragalactic signal that will allow us to probe to r∼0.03 at 150 GHz in the range $50 < \ell < 150$ before Galactic foreground confusion becomes important.

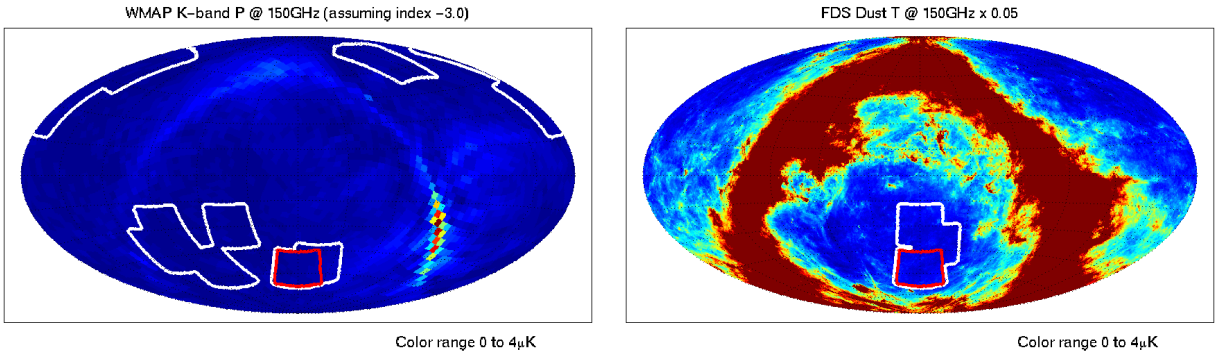

Figure 2.7: All-sky maps of expected levels of polarized foregrounds at 150 GHz. The projection is centered on α, δ = (0,0). *Left*: The *WMAP* K-band polarized intensity map is extrapolated to 150 GHz assuming a synchrotron spectral index of -3. *Right*: The FDS total intensity dust map is multiplied by an assumed dust polarization fraction of 5%. Outlined in white are all the trial fields found to be as good or better than BICEP's chosen field, which is outlined in red.

Although the emission from the Galaxy at millimeter wavelengths is a potential contaminant for CMB observations, it is also a rich source of astrophysical information. The composition and emission spectrum of the Galaxy vary across the sky, presenting an opportunity to study our Galaxy. We can study such spatial variations with multi-band observations in the infrared and millimeter wavelengths measuring continuum emission, spectral lines, and polarization. The gas and dust density in the interstellar medium (ISM) varies from <1 particle/cm^3 in diffuse regions to >10^6 particles/cm^3 in molecular clouds and complexes (collections of star-forming cloud cores of similar ages).

The ISM emission is partially polarized. Star light is polarized due to dust grains aligned by the Galactic magnetic field preferentially absorbing light perpendicular to the Galactic plane; this probes ISM's diffuse component. Dust grains aligned by the magnetic field emit predominantly in the millimeter band preferentially along their orientation axis, resulting in thermal dust emission polarized orthogonal to the Galactic magnetic field unlike starlight polarization. Millimeter band measurements could probe a wide range of ISM densities while near-infrared measurements could better resolve medium to high density ISM regions. The desire to characterize the ISM motivates microwave continuum polarimetry imaging of the

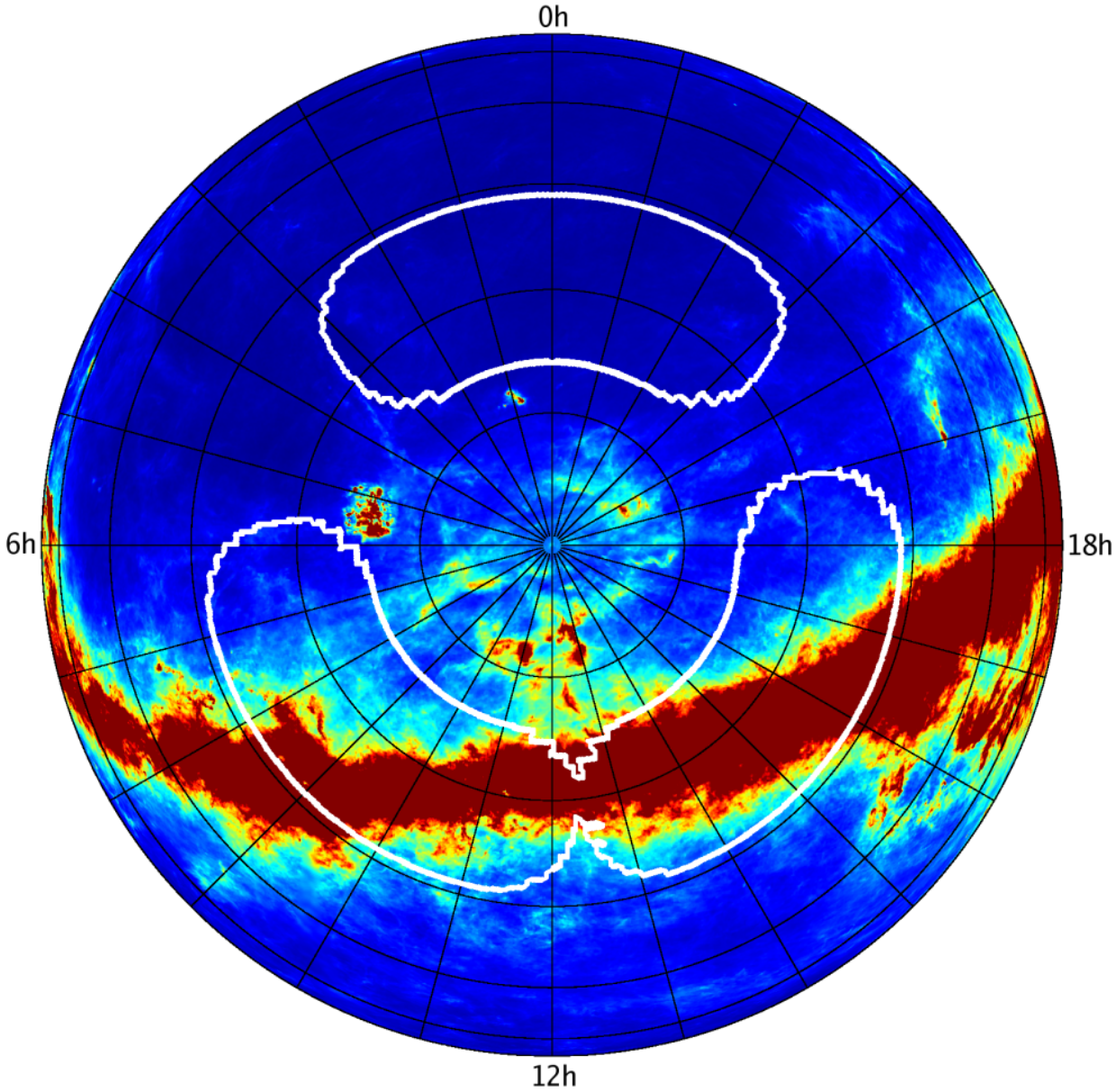

Figure 2.8: BICEP's CMB and Galactic fields outlined on the 100 GHz FDS model 8 prediction of dust emission [10].

Galaxy, as maps of dust, ionized gas, and magnetic fields from these bands can probe a wide range of ISM densities and compositions. Only a few experiments have explored Galactic polarization properties at frequencies near 100–150 GHz, such as QUaD, *Archeops*, and *WMAP*.

To study polarization on and off of the Galactic plane, Bicep spent 6 hours every other day mapping two additional fields covering the Galactic plane (Figure 2.8). The secondary field was centered at $\{\alpha = 9$ hr, $\delta = -57.5°\}$, encompassing the bright Eta Carinae region. In addition, we used a third field centered at $\{\alpha = 15{:}42$ hr, $\delta = -55.0°\}$, in a significantly brighter part of the Galactic plane as a daily calibration source, performing repeated fixed-elevation scans for 10 min at the beginning and end of every 9-hr observing block. To gain additional information about emission from sources other than the CMB, we added to Bicep a third frequency band at 220 GHz from the 2nd year.

Between the 2007 and 2008 observing years, the original plan was to warm up the cryostat and leave it dormant during the month of December. Instead, Bicep dedicated its time to integrating deeper into the Galactic fields and mapping regions at higher Galactic latitudes. In addition, we mapped a region overlapping with the Boomerang field to cross correlate with their high frequency data to study dust. These observations increased the final amount of Galactic data by ∼30%.

2.5 Observing strategy

With a field of view spanning 17°, Bicep mapped an 800 deg^2 field daily by scanning the boresight in azimuth over a 64° range at 2.8°/s with hourly 0.25° steps in elevation from 55° to 60°. At each elevation step, the telescope completed 50 back-and-forth azimuth scans, or 100 "half-scans," making up a "scan set". We selected the scan speed such that our target angular scales ($\ell \sim 30$–300) appear at 0.1–1 Hz, above a significant portion of the $1/f$ atmospheric noise, while limiting motion-induced thermal fluctuations at the detectors.

Azimuth scanning was chosen over the initial proposal of boresight rotation with a simple fixed-azimuth mount. Azimuth scanning keeps the atmospheric column density fixed, reducing possibilities for false signal due to changing background loading. It also allows us to limit the observation to regions of the sky with exceptionally low foreground confusion.

The temperature stability of the focal plane varied with azimuth scan speed as well as the cryostat orientation about its axis. We investigated the stability under a variety of telescope operating conditions, including scan speeds in a range of 1.0°/s – 4.0°/s, and 16 evenly spaced boresight rotation angles. Based on the minimum variance of the scan-synchronous thermistor signals, we selected the 2.8°/s nominal scan speed (Figure 2.9) and four cryostat orientations about the boresight: $\{-45°, 0°, 135°, 180°\}$.

Bicep operated in a 48 sidereal-hour observing cycle (Figure 2.10), with each cycle at one of the four fixed boresight rotation angles. A 45° rotation about the boresight exchanges the polarization coverage on the sky, providing two independent pairings of angles, ($\{-45°, 135°\}$ and $\{0°, 180°\}$), each with complete polarization coverage per overlapped sky pixel. The two sets rotated by 180° also help to average down systematic effects like pointing offset between PSB pair.

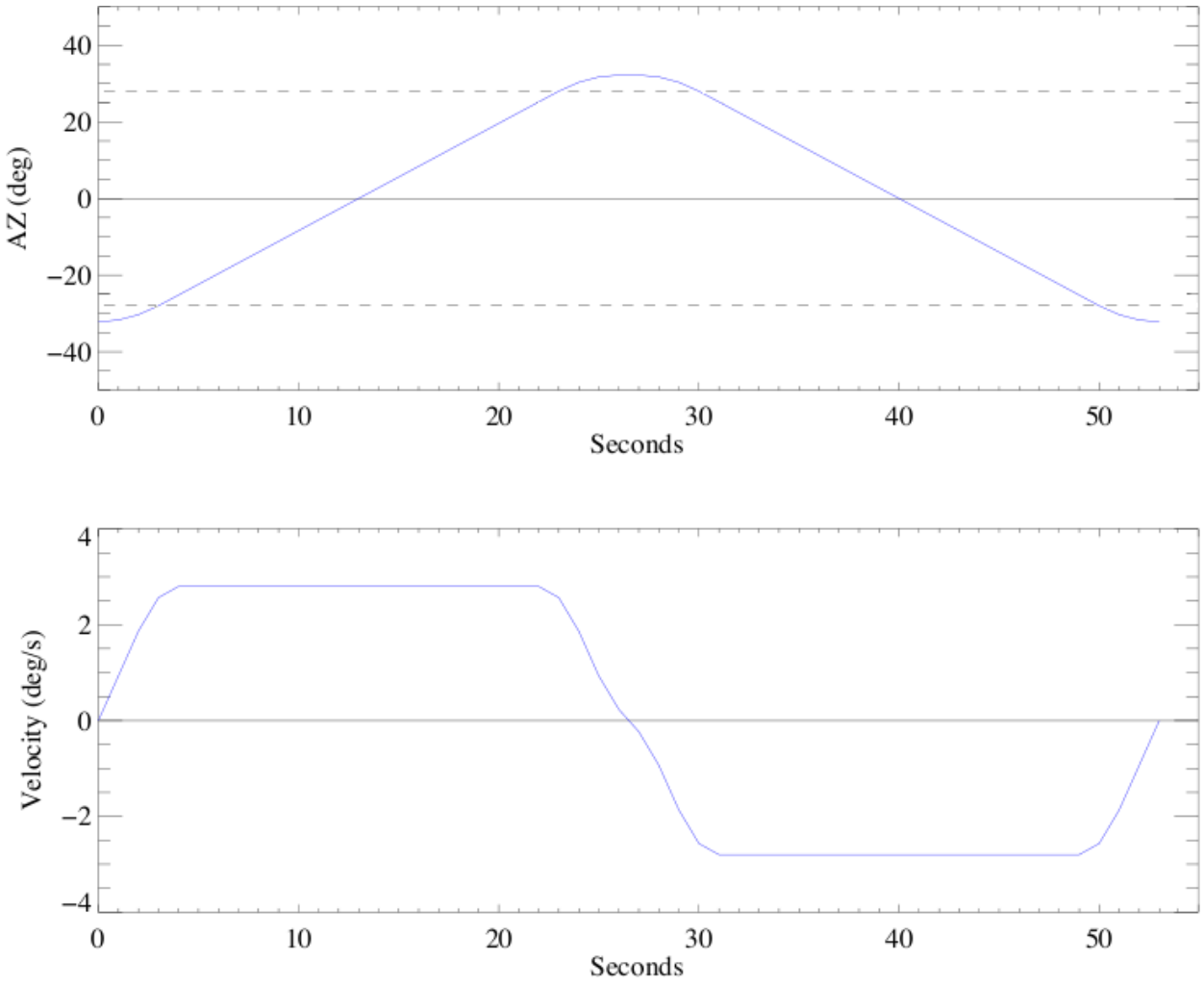

Figure 2.9: A 2.8°/s azimuth scan profile used in mapping the CMB field. The acceleration during turn-arounds is limited to 1.4°/s^2; the jerk is limited to 0.47°/s^3. We used a 20-s portion of mostly constant-velocity scan for each direction, resulting in 75% scan efficiency.

Each 48-hr cycle began with 6 hr allocated for recycling the refrigerator, filling LN_2 (every 2 days) and LHe (every 4 days), and performing optical star-pointing calibrations along with a mount tilt measurement. The CMB field was completely mapped once each day in two 9-hr blocks, with the scan order of the upper and lower halves of the elevation range switched such that the azimuth ranges for the two days were offset. Differencing the first and second days of a given 48-hr observing cycle tests for potential azimuth-fixed contamination. BICEP achieved overlapping coverage of the sky from detectors with various polarization orientations by scanning in azimuth, stepping in elevation, and rotating the telescope with respect to the boresight every 2 days.

Each scan set at a given elevation was fixed with respect to a given azimuth range instead of tracking the field center over the hour-long period. This scan strategy allowed for a straightforward removal of any azimuth- or scan-synchronous contamination. For each

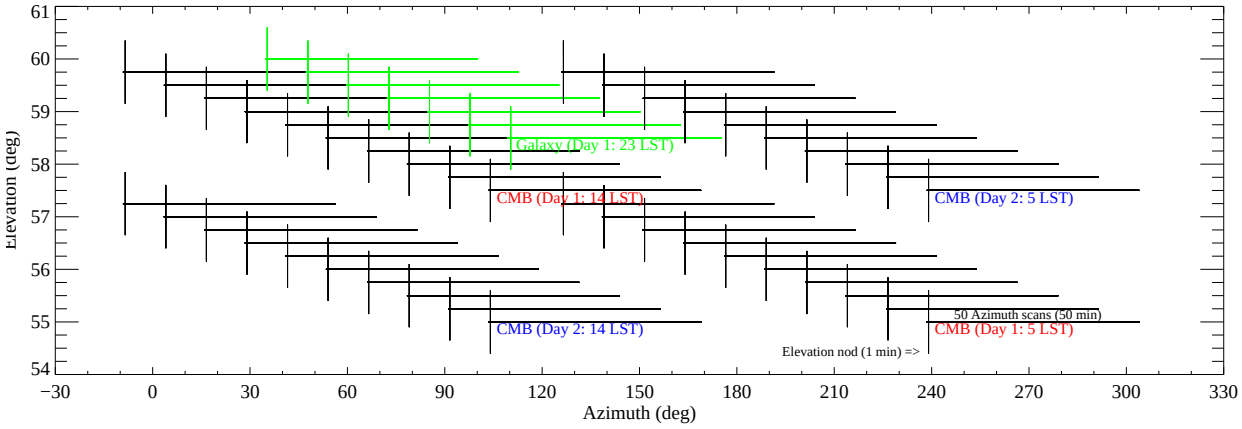

Figure 2.10: A 48-hr observing cycle consisted of 6 hr for recycling the refrigerator (not shown), two 9-hr blocks of raster scans on our main CMB field on the first day, a 6-hr block of similar raster scans on the Galaxy, and two more 9-hr blocks on the main CMB field on the second day. Each of the upper and lower halves of the elevation range was scanned in different azimuth ranges between the two days, allowing a jackknife test for ground contamination. At the beginning and end of each set of 50-min azimuth scans, a $\pm 0.6°$ elevation "nod" was performed to measure relative gains of every bolometer. We repeated this 48-hr cycle at different boresight rotation angles: $\{-45°, 0°, 135°, 180°\}$.

scan set and each of the two scan directions, the entire timestream was simply binned in azimuth to form a template signal which was subtracted from each half-scan.

Relative detector responsivities were measured at the beginning and end of each one-hour fixed-elevation scan set by fitting the detector response to a small change in line-of-sight airmass ("elevation nods"), described in §4.2.2. An elevation nod consisted of a rounded triangle wave motion of the telescope with a 1.2° peak-to-peak elevation change, the detector voltages varying in response to the changing line-of-sight air mass. We performed the nod over a 45-s period to reduce thermal disturbances on the focal plane, and any thermal effects were accounted for by using mirror-image elevation nods at the beginning and end of each scan set (up-down-return and down-up-return).

Chapter 3

Hardware development

During my first 2 years I worked on various components of the telescope, mostly external to the receiver cryostat since it was at JPL/Caltech and I was the only one in Berkeley with Bill. My hardware contributions, some of which are illustrated in Figure 3.1, included the vacuum window, ground shield, polarization calibrator, telescope mount and its motion control system, optical star-pointing camera, and refrigerator electronics.

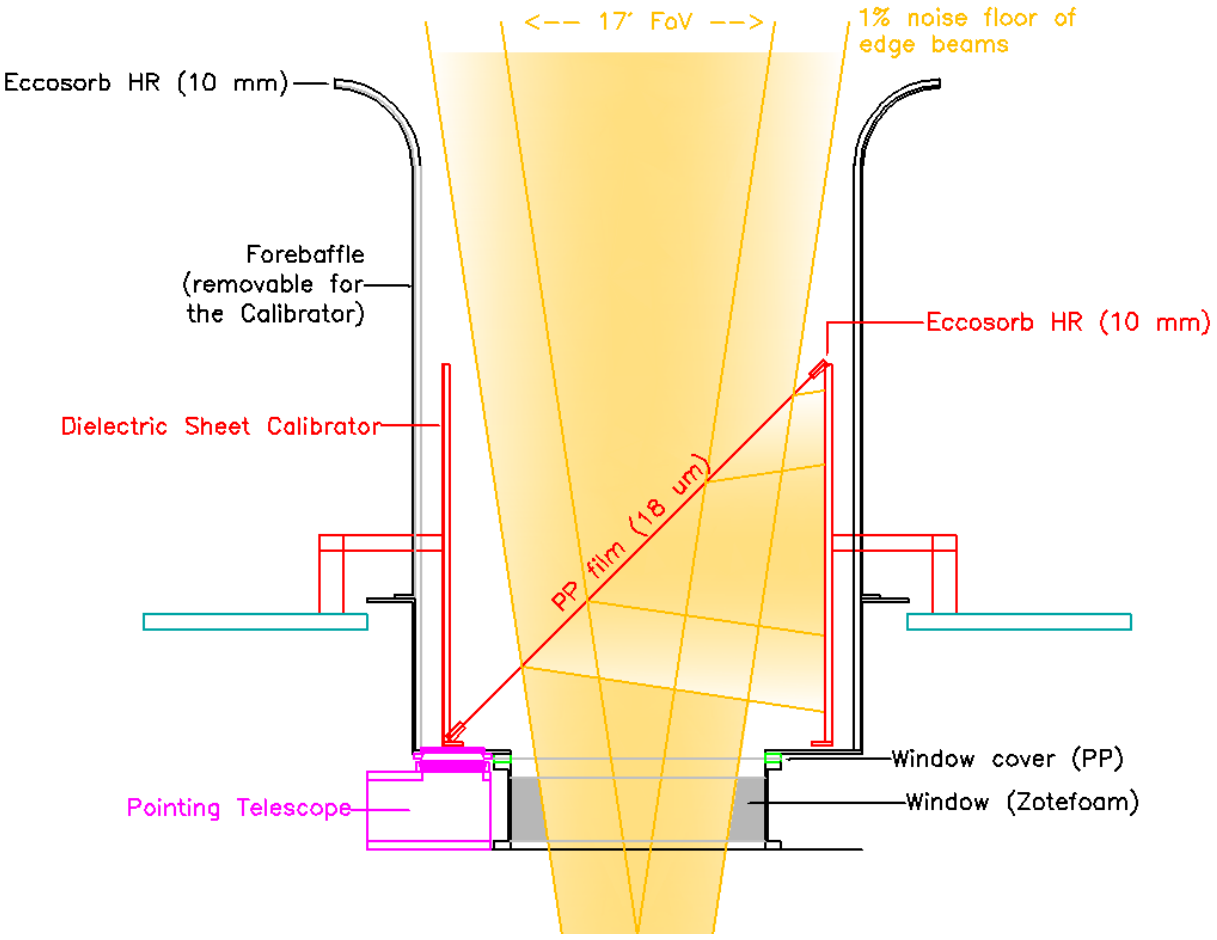

Figure 3.1: Diagram of vacuum window on top of the cryostat, forebaffle, polarization calibrator, and optical star-pointing camera.

3.1 Vacuum window

The vacuum window was my first hardware project. It had to hold vacuum at the cryostat's 30 cm aperture while being transparent in the observing wavelength bands. We used four layers of closed-cell nitrogen expanded polypropylene foam (Zotefoam PPA30[1]), heat-laminated to form a single 10-cm thick slab and sealed to an aluminum frame using Stycast epoxy. A similar low-loss Zotefoam window was used in ACBAR, using a 2.5-cm thick foam for an 11-cm diameter window. To maintain the same amount of shear on the foam, its thickness needed to scale linearly with the window diameter. Scattering at mm wavelengths is very low due to the small cell size (0.3 mm) and low density (30 mg/cm^3). In addition, the foam is opaque to much of infrared radiation, limiting the radiation loading on the cryostat.

To measure Zotefoam's transmission, thermal radiation from liquid nitrogen, chopped at 5 Hz, was collimated with a parabolic mirror and then refocused with another parabolic mirror into a feedhorn through filters and guided to a bolometer in a cryostat. I used four filters for this measurement: wavenumbers 5.9/cm, 8.0/cm, 8.6/cm, and a high-frequency blocking filter. I measured the filters' transmission spectra using a Fourier transform spectrometer with a 0.25-mm Mylar as the beam-splitter. I also measured the spectrum of the blocking filter up to 2000 GHz to ensure no leakage. While sampling the bolometer output with a lock-in amplifier, I inserted in and out a 10-cm thick Zotefoam large enough to completely intercept the collimated portion of the beam every other 10-s interval. Averaging over 16 insertions, the loss was only 1% at 150 GHz and is expected to be even smaller at longer wavelengths. This is expected to add 2-3 K_{RJ} of optical loading on the detectors.

We cut out a 40-cm diameter piece of Zotefoam with a hot wire and a rotatable mount, and carefully glued it in the aluminum frame with Stycast. I constructed several spare windows, but the same window held vacuum for all 3 years of operation at the South Pole.

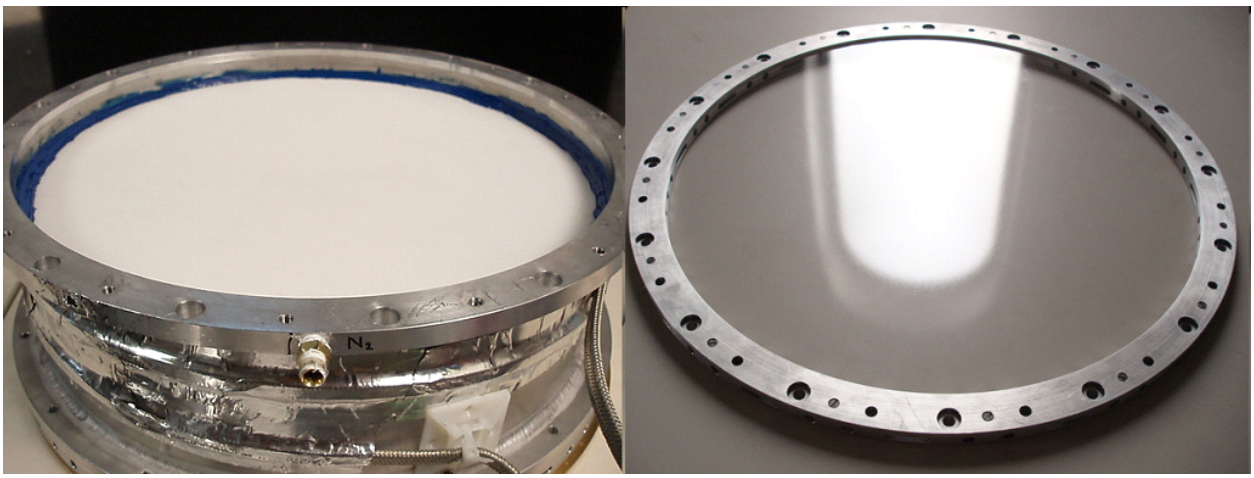

Figure 3.2: Vacuum window made of 10-cm thick Zotefoam (left) and a polypropylene window cover for keeping snow off (right).

[1]Propozote PPA30, `http://zotefoams.com/pages/en/datasheets/PPA30.htm`

Because the foam window is radiatively cooled to below ambient temperature from both sides, frost can form from residual moisture in the air. To prevent this, we have installed a taut 18-μm polypropylene film as a cover, with the air space between the cover and the Zotefoam window slightly pressurized and continuously purged by warm dry nitrogen gas to sublimate away any snow that lands. This film is expected to have a negligible reflection of 0.05 % and 0.1 % at 100 and 150 GHz, respectively.

To monitor the window, we installed an infrared camera near the window. When BICEP began observations in 2006, we noticed that snow landed on the window cover almost every day and stayed there for many hours. To mitigate this, we tried drilling 32 holes (6-mm diameter) radially around the window cover ring so that warm air from the building flows out onto the top of the window cover. The window images for the next 10 days indicated that this was working to sublimate the snow more quickly, so we doubled the number of holes at the end of April. During May 2006, the window had snow on 7 occasions for a total of 95 hours over 36 days, translating to 10% of the time (not necessarily during observation). Also, the times when snow was on the window correlated with high atmospheric opacity.

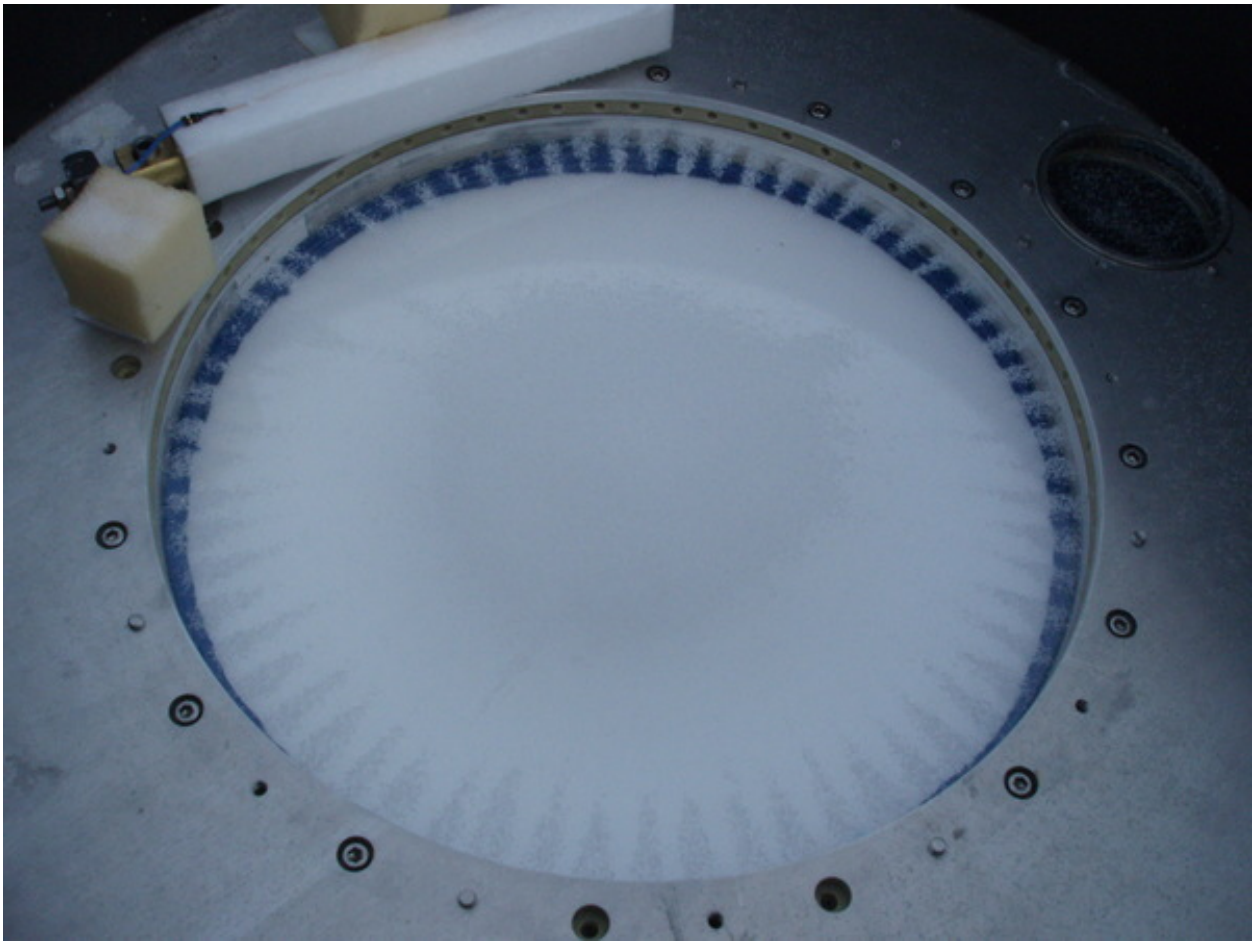

Figure 3.3: Snow on the window cover sublimating due to warm air blowing out of the holes in the window cover holder.

3.2 Ground screen and forebaffle

For BICEP to detect <0.1 μK level polarization signal, the ground radiation must be attenuated by at least 9 orders of magnitude before it enters the window through diffraction. We chose to use two levels of shielding against ground radiation: an absorptive forebaffle fixed to the cryostat and a large stationary reflective screen surrounding the telescope structure, modeled after the POLAR experiment [22]. The shields had to work for the telescope's elevation range of $50° - 90°$. I designed the geometry so that any radiation from the ground must be diffracted at least twice before entering the window in any telescope orientation.

The forebaffle is an aluminum cylinder lined with a microwave absorber to minimize reflected radiation into the telescope. At BICEP's lowest nominal CMB observing elevation of 55°, the forebaffle is long enough (107 cm) to prevent radiation from sources, particularly the Moon, at elevations up to 27° from entering the window directly. The Moon rises above this elevation (up to 28°) only one day a month. The baffle is wide enough to clear 99% of the edge pixel beam power. Beyond that, the Zotefoam window is expected to scatter up to 1% of the total power nearly isotropically, so making the baffle wider has diminishing benefits. Integrating the predicted beam pattern 1 m above the window (Fig. 3.4) indicated

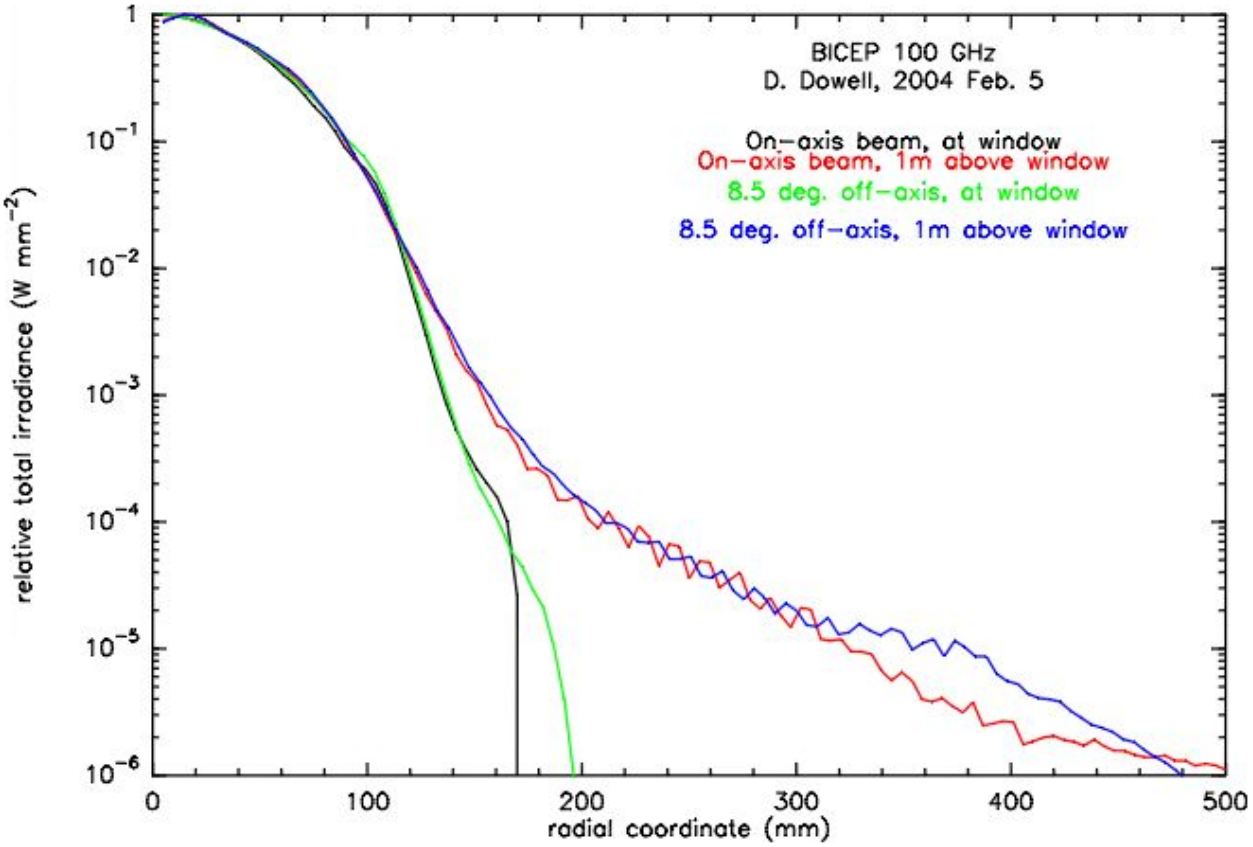

Figure 3.4: Predicted beam patterns, at the base of the window and 1 m above the window, not accounting for scattering due to the Zotefoam window. At the window base, the effect of truncation by the pupil is visible. At 1 m, the beams are still in the near field.

that 99% of the total power is within a 13-cm radius. This suggested that the lip of a 1-meter forebaffle should be at least 13 cm from the center of the off-axis beam at the edge of the focal plane. The forebaffle aperture lip was rounded with a 13-cm radius to reduce diffraction of the diffuse beam sidelobes. These forebaffle dimensions also ensured that any radiation from the projected South Pole Telescope (SPT) ground shield must diffract around the lip of the forebaffle before entering the window.

For the microwave absorber, I explored and tested many materials, some of which are listed in Table 3.1. I used a tunable Gunn oscillator (83–115 GHz), a diode detector, and a movable mirror (onto which I can mount Eccosorb to be tested) in a lock-in system using a chopper. The most important criterion is low reflectivity. Another consideration is that the material should be immune to snow accumulation. One approach for snow mitigation is to keep the absorber surface at least 1 K above ambient temperature to sublimate away any snow that lands. For this purpose, I searched for materials with higher thermal conductivity or a very smooth surface.

Table 3.1: Microwave absorbers candidates for forebaffle

Eccosorb	TE reflectivity [a]	Thermal conductivity [b]	Notes
HR-10	$< 1\%$ @ 100/150 GHz	$\sim$0.005 W/K/m	Foamy
ANW-72	1-3% / 5-15% @ 100/150 GHz	0.027 W/K/m	Foamy
BSR	20-30% @ 150 GHz	0.8 W/K/m	Smooth, adhesive
CRS/MFS	30-90% @ 100 GHz	0.9 W/K/m	Castable/rubbery

[a] Measured transverse-electric reflectivity at 45° incidence, when placed over aluminum.

[b] `http://www.eccosorb.com/america/english/page/63`

In the end we chose a 10-mm thick open-cell polyurethane foam sheet (Eccosorb HR[2]), which had the lowest measured reflectivity of <3% at 100 and 150 GHz when placed over a metal surface (150 GHz results by [32]). To prevent snow from accumulating in the porous

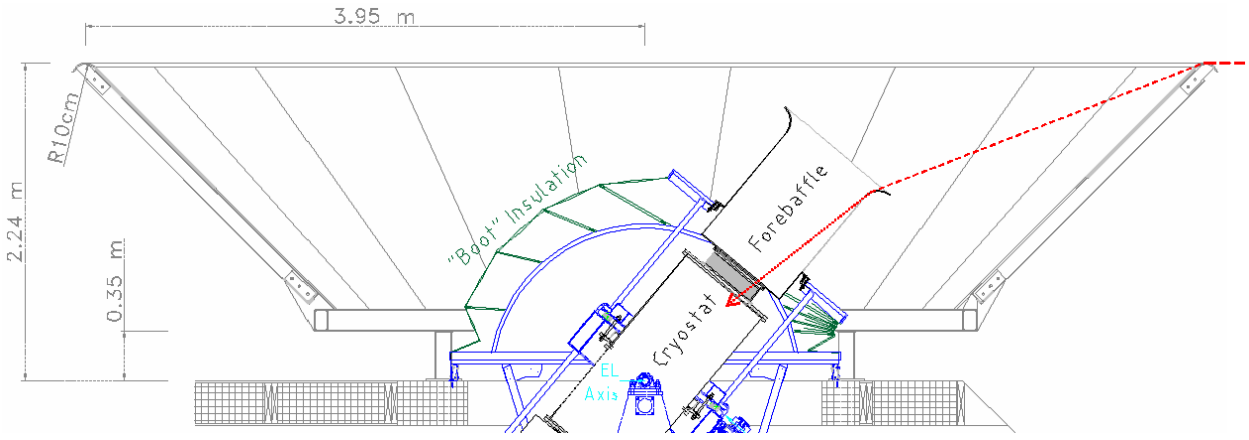

Figure 3.5: Schematic of outer ground screen and inner forebaffle.

[2] `http://www.eccosorb.com/products/40/`

Eccosorb foam, I covered it with a 1.6-mm thick smooth polyethylene foam (Volara[3]), gluing it on with a silicone sealant. The combined Eccosorb HR / Volara stack was measured to reflect ∼5% of 100 GHz radiation incident at 45°.

A self-regulating heat cable is wrapped around the outside of the baffle to sublimate any snow on the baffle surface, if necessary. For snow to sublimate, the shield needs to be at least 1-2 K above the ambient temperature. Heating an exposed metal surface at the South Pole requires ∼50 W/m^2/K [35]. Since the forebaffle has a surface area of ∼6 m^2, this amounts to ∼300 W/K. The measured additional loading on the bolometers due to emission from the forebaffle was ∼1 K_{RJ}. Since the absorptive baffle is fixed with respect to the detectors, its thermal emission is expected to be stable against the modulated sky signal.

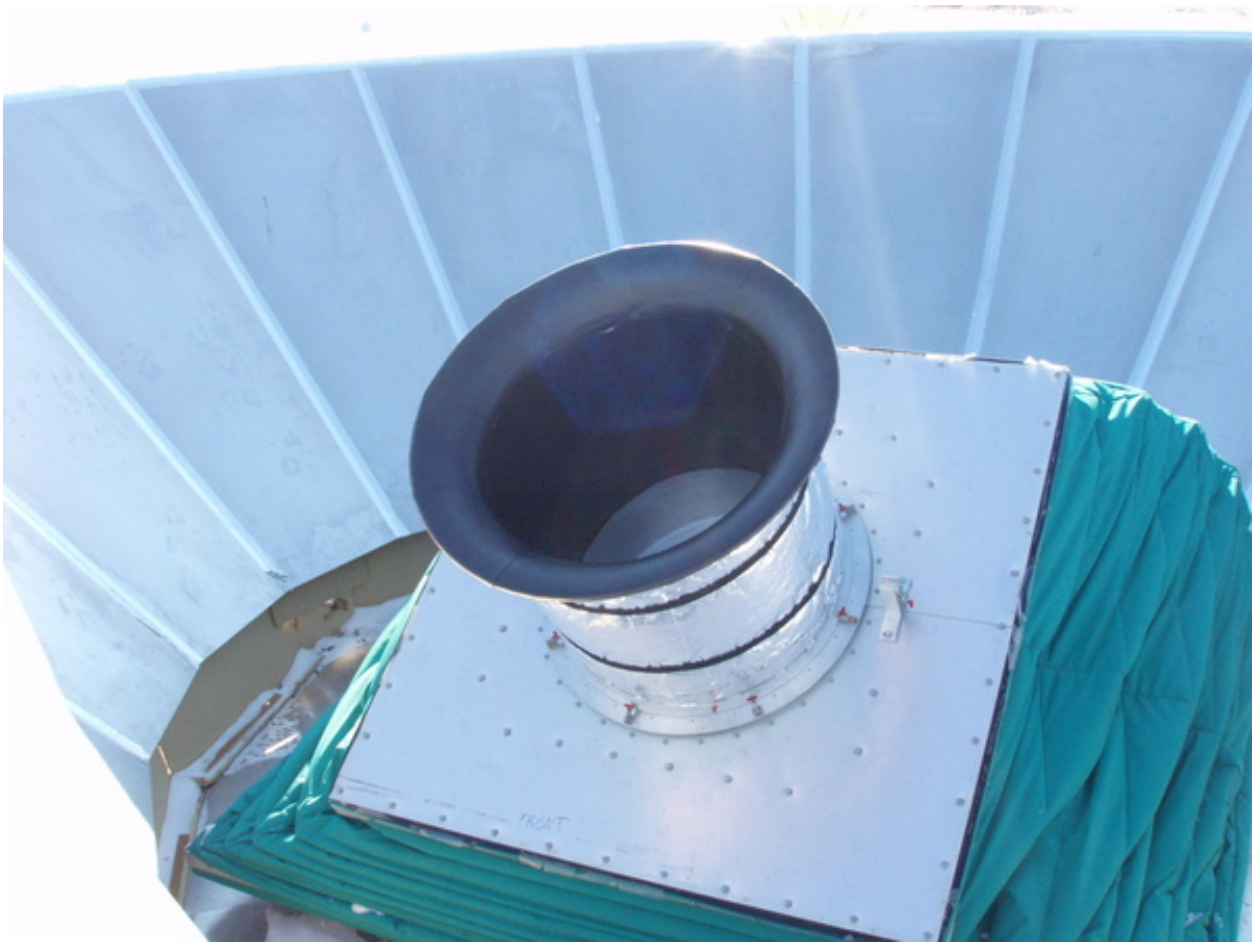

Figure 3.6: Photograph of absorptive forebaffle and reflective ground screen.

The outer screen is tall enough (2.2 m) to shield the forebaffle from the ground radiation even when the telescope is vertical. The sloped aluminum surface with low emissivity and high reflectivity presents the beam spillover with a reflection of relatively homogeneous cold sky. The 8-m top diameter is wide enough for the diffracted ground radiation to never

[3]Volara; Sekisui Voltek, `http://www.sekisuivoltek.com/products/volara.php`

directly hit the window even when the telescope is at its 50° elevation lower limit. The 1.5-m bottom radius is just enough to clear the square footprint of the boot-type enclosure (2.7 m on a side). This creates a gap for snow to fall through and made the shield slope ∼50°, steep enough to allow snow to slide down and shallow enough to direct most sidelobes to the sky.

The edge of the outer screen is also rounded with a 10-cm radius to reduce diffraction. I estimated the attenuation from the outer screen using the geometrical theory of diffraction [23]. With a 10-cm radius edge, the attenuation just barely in the shadow is -20 dB and the power is attenuated by -6 dB per 10° change in the propagation direction. Since the ground radiation must diffract by at least 17° to reach the forebaffle, the outer screen is expected to provide at least -30 dB of attenuation. The calculated performance improved only slightly with increasing radius of curvature, as long as it is much greater than the wavelength.

The measured sidelobes with and without the forebaffle are in Figure 4.15 in the sidelobe rejection section (§4.6). The forebaffle achieved a sidelobe performance of -70 dB to the outer screen lip even at the lowest observing elevation. Together with the outer screen, the ground shield system successfully met the -90 dB goal.

3.3 Polarization calibrator

We measured the PSBs' polarization orientations using a rotatable dielectric sheet, modeled after the one used by POLAR [38]. A small partially polarized signal of known magnitude is created by using a dielectric sheet in front of the telescope aperture oriented at 45° from the optical axis. The sheet acts as a beam splitter transmitting most of the sky radiation but reflecting a small polarization-dependent fraction of the radiation from an ambient load perpendicular to the beam. The polarized signal is small compared to the unpolarized sky background so that it can provide an absolute responsivity calibration in optical loading conditions appropriate for normal observations.

We used this polarization calibrator by putting it in the place of the forebaffle and fixing it to the azimuth mount. With the telescope pointed at zenith, rotating the device with respect to the cryostat modulates the polarization signal for each detector while keeping the beams stationary with respect to the sky. With this method, we can use the telescope mount's axis encoders to precisely record the orientations of the cryostat and the calibrator to obtain absolute PSB orientations. The off-axis beams see complicated, but calculable, deviations from the nominal sinusoidal modulation.

We can compute the expected calibrator signal by calculating the transmission of the sky radiation (T_{C}) through and the reflection of the ambient load (T_{H}) off of the dielectric, treating transverse electric (TE) and transverse magnetic (TM) separately (Figure 3.7). The expected Stokes Q signal at a PSB, as a function of the relative angle φ with the calibrator, was calculated as follows, where $I_{x',y'}$ are the brightness temperature of the radiation along

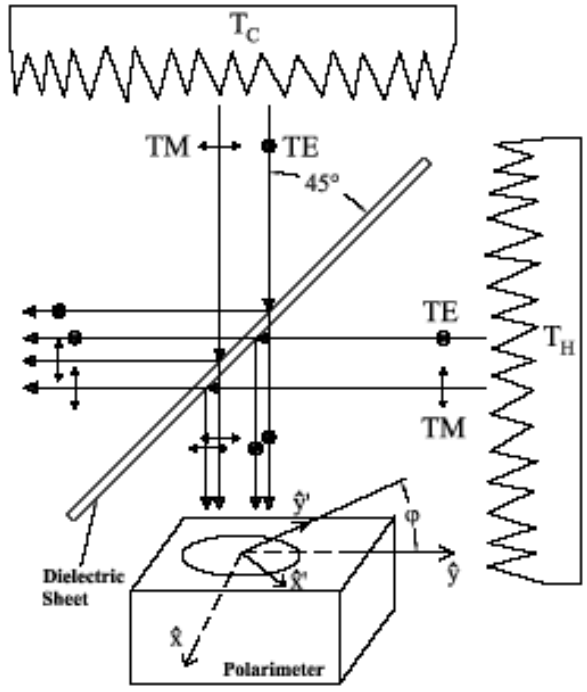

Figure 3.7: Dielectric sheet calibrator diagram [38].

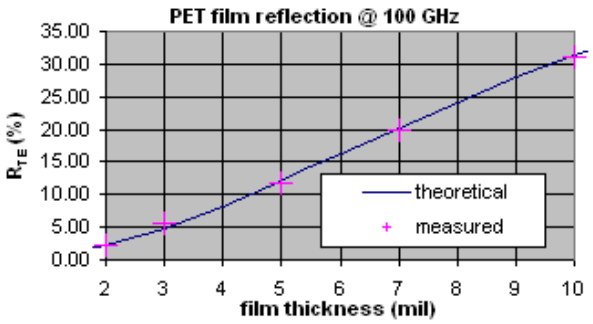

Figure 3.8: TE reflectivity of Mylar sheets of various thicknesses at 100 GHz and 45° incidence. The lab measurements confirmed the validity of the calculated theoretical expression (Equation 3.10).

(x') and perpendicular to (y') the PSB, respectively:

$$Q(\varphi) = (I_{x'} - I_{y'})/2. \tag{3.1}$$
$$I_{x'} = T_{\rm C}T_{x'} + T_{\rm H}R_{x'}, \tag{3.2}$$
$$I_{y'} = T_{\rm C}T_{y'} + T_{\rm H}R_{y'}, \tag{3.3}$$

where $T_{x',y'}$ and $R_{x',y'}$ are the transmittance and reflectivity for radiation incident along the respective directions. With $T_{x'} = 1 - R_{x'}$ and $T_{y'} = 1 - R_{y'}$, the expression simplifies to:

$$Q(\varphi) = (T_{\rm H} - T_{\rm C})(R_{x'} - R_{y'})/2. \tag{3.4}$$
$$R_{x'} = R_{\rm TE}f^2_{\rm x'TE} + R_{\rm TM}f^2_{\rm x'TM}, \tag{3.5}$$
$$R_{y'} = R_{\rm TE}f^2_{\rm y'TE} + R_{\rm TM}f^2_{\rm y'TM}, \tag{3.6}$$

where $R_{\rm TE,TM}$ are the reflectivity along TE and TM, and $f_{\rm x'TE}$ is the coupling fraction of TE radiation onto x' direction, and so on. From orthogonality, $f^2_{\rm x'TM} = 1 - f^2_{\rm x'TE}$ and $f^2_{\rm y'TM} = f^2_{\rm x'TE}$. The expression then reduces to:

$$Q(\varphi) \approx (T_{\rm H} - T_{\rm C})(R_{\rm TE} - R_{\rm TM})(f^2_{\rm x'TE} - 1/2). \tag{3.7}$$

The coupling fraction was computed from geometry as follows, with $\hat{\mathbf{b}}$ being the direction of the beam making an angle θ_b from the boresight, and $\hat{\mathbf{n}}$ being the direction normal to the dielectric sheet tilted at an angle $\theta_t \approx 45°$ and making an angle φ with respect to the PSB.

The TE direction would be $\hat{\mathbf{b}} \times \hat{\mathbf{n}}$ and the cosine of the beam incident angle θ_i would be $\hat{\mathbf{b}} \cdot \hat{\mathbf{n}}$.

$$
\begin{aligned}
f_{\mathrm{x'TE}} &= \hat{\mathbf{x}}' \cdot \frac{\hat{\mathbf{b}} \times \hat{\mathbf{n}}}{|\hat{\mathbf{b}} \times \hat{\mathbf{n}}|} \qquad\qquad \hat{\mathbf{b}} = \begin{bmatrix} 0 \\ \sin\theta_b \\ \cos\theta_b \end{bmatrix}, \quad \hat{\mathbf{n}} = \begin{bmatrix} \sin\theta_t \sin\varphi \\ \sin\theta_t \cos\varphi \\ \cos\theta_t \end{bmatrix}, \quad \hat{\mathbf{b}} \cdot \hat{\mathbf{n}} = \cos\theta_i, \\
&= \begin{bmatrix} \cos\theta_p \\ \sin\theta_p \\ 0 \end{bmatrix} \cdot \begin{bmatrix} \sin\theta_b \cos\theta_t - \cos\theta_b \sin\theta_t \cos\varphi \\ \cos\theta_b \sin\theta_t \sin\varphi \\ -\sin\theta_b \sin\theta_t \sin\varphi \end{bmatrix} / \sin\theta_i \\
&= (\cos\theta_p(\cos\theta_b \sin\theta_t \cos\varphi - \sin\theta_b \cos\theta_t) + \sin\theta_p \cos\theta_b \sin\theta_t \sin\varphi) / \sin\theta_i, \qquad (3.8)
\end{aligned}
$$

and where

$$
\theta_i = \mathrm{Cos}^{-1}(\hat{\mathbf{b}} \cdot \hat{\mathbf{n}}) = \mathrm{Cos}^{-1}(\sin\theta_b \sin\theta_t \cos\varphi + \cos\theta_b \cos\theta_t). \qquad (3.9)
$$

The TE and TM reflectivity was computed from superposition of the reflection off of the front and back surfaces of the dielectric of thickness d:

$$
R_{\mathrm{TE,TM}} = \frac{r_1^2 + r_2^2 + 2r_1 r_2 \cos\beta}{1 + (r_1 r_2)^2 + 2r_1 r_2 \cos\beta}, \qquad (3.10)
$$

where $r_{1,2}$ are the amplitude reflection coefficients off of the front and back surfaces, respectively:

$$
\mathrm{TE}: \quad r_1 = \frac{\cos\theta_i - n\cos\theta_n}{\cos\theta_i + n\cos\theta_n}, \qquad r_2 = \frac{n\cos\theta_n - \cos\theta_i}{n\cos\theta_n + \cos\theta_i} = -r_1. \qquad (3.11)
$$

$$
\mathrm{TM}: \quad r_1 = \frac{\cos\theta_i - \frac{1}{n}\cos\theta_n}{\cos\theta_i + \frac{1}{n}\cos\theta_n}, \qquad r_2 = \frac{\frac{1}{n}\cos\theta_n - \cos\theta_i}{\frac{1}{n}\cos\theta_n + \cos\theta_i} = -r_1. \qquad (3.12)
$$

Here, $\theta_n \equiv \mathrm{Sin}^{-1}(\sin\theta_i/n)$ is the refracted angle inside the dielectric of refractive index n, and $\beta = 4\pi n d \cos\theta_n/\lambda$ is the phase difference between the waves reflected off of the front and the back surfaces. To verify the reflectivity expression, I measured the reflectivity of Mylar for various thicknesses and compared with the theoretical value (Figure 3.8).

This setup produces a partial polarization of amplitude: $Q \propto (T_{\mathrm{H}} - T_{\mathrm{C}})(R_{\mathrm{TE}} - R_{\mathrm{TM}})$, where the signal varies not only with the rotation angle φ about the boresight but also with the reflectivity difference between TE and TM, which turns out to be proportional to $\nu^2 d^2 n^4$. To achieve 10% accuracy in absolute gain calibration, the thickness must be known and uniform to within 4–5% and refractive index to within 2%.

To make T_{H} similar to the ambient temperature, I designed to surround the beam splitter with an aluminum cylinder whose inside surface is lined with a good microwave absorber (10 mm Eccosorb HR). I covered the absorber with a 1.6 mm thick sheet of closed cell expanded polyethylene foam exactly as in the forebaffle (§3.2), the combination of which had ∼95% emissivity at 100 GHz.

For accurate knowledge of $(R_{\mathrm{TE}} - R_{\mathrm{TM}}) \propto \nu^2 d^2 n^4$, I tried to choose a strong dielectric material that can maintain a uniform thickness and has a well known refractive index. Table 3.2 lists the primary candidates.

Table 3.2: Dielectric sheet material candidates for polarization calibrator

	Refractive index @ 100 / 150 GHz [27]	Notes
PP (polypropylene)	1.50168 / 1.50165	
PETP (Mylar)	1.74 / 1.83	Loss tangent ≈ 0.01 [a]
PTFE (Teflon)	1.439 / 1.433	Thickness easily varied

[a] Emission not negligible if thickness is <50 μm [38].

To work well at South Pole temperatures, I tried to select materials for the calibrator carefully, taking into account their relative thermal contraction and thermal conductance. Any materials used to keep the dielectric sheet taut would contract when taken outside to South Pole temperatures, possibly loosening the sheet. Table 3.3 lists the thermal contraction coefficients of the primary dielectric candidates as well as those of the sheet holder material candidates. For the sheet holder, I considered materials with smaller contraction coefficients than aluminum, but fortunately PP and PETP had higher contraction coefficients. Therefore I simply chose aluminum, which is relatively inexpensive and the easiest to machine. When tested in a refrigerator, the sheet holder made of aluminum shrank by 2 mm at about -60 °C, and made both the PP and PETP sheets loose even though these polymers should have contracted about twice more. I discovered that when the assembly is first exposed to the cold temperature, the dielectric contracts quickly and becomes taut, but then the aluminum

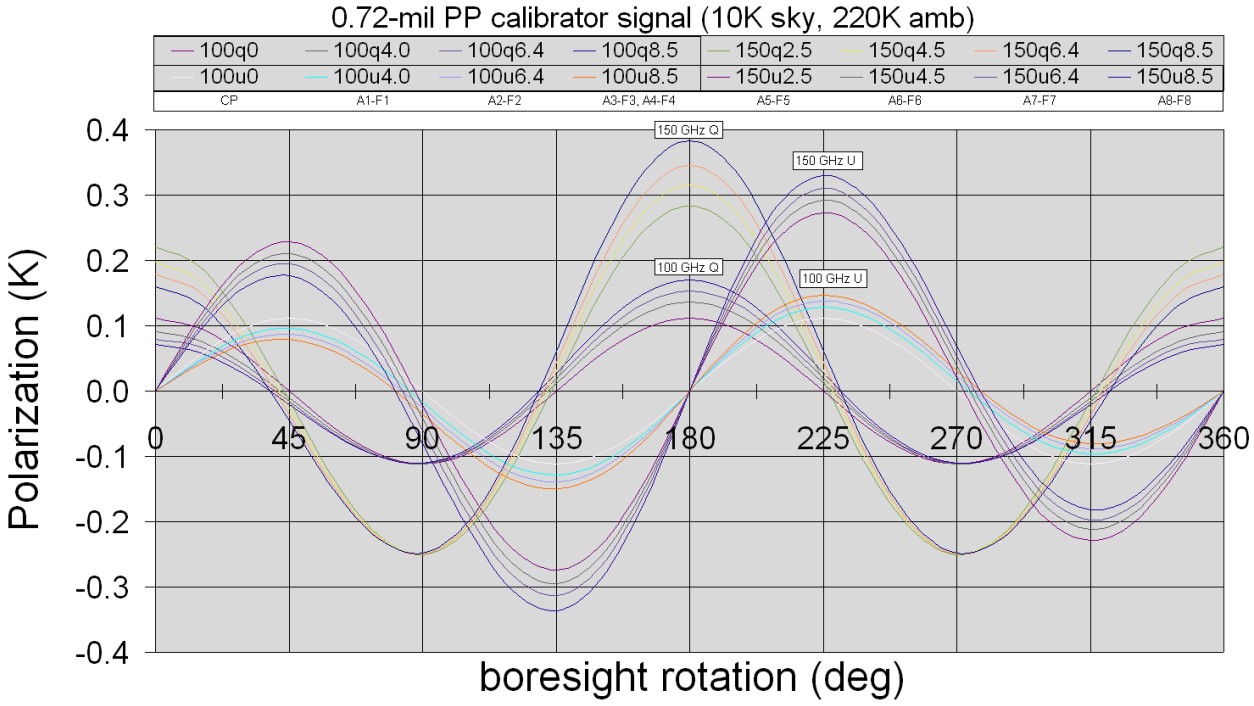

Figure 3.9: Expected polarization signal from a dielectric sheet calibrator using 18-μm PP sheet, as a function of rotation about the boresight. Curves were computed for the two frequency bands, different PSB orientations (Q, U) with respect to the focal plane radius, and different beam directions from the boresight ($0°, 2.5°, 4.0°, 4.5°, 6.4°, 8.5°$).

contracts more gradually and loosens the sheet again. We were able to resolve this issue by reheating the dielectric only with a heat gun and let it contract once again.

Table 3.3: Thermal contraction coefficient of candidate dielectrics and sheet holder materials for polarization calibrator

	Thermal contraction coefficient
PP (polypropylene)	6×10^{-5} / K
PETP (Mylar)	5×10^{-5} / K
Aluminum	3×10^{-5} / K
Phenolic	2×10^{-5} / K
Stainless steel	1-2$\times 10^{-5}$ / K
Invar	1×10^{-5} / K

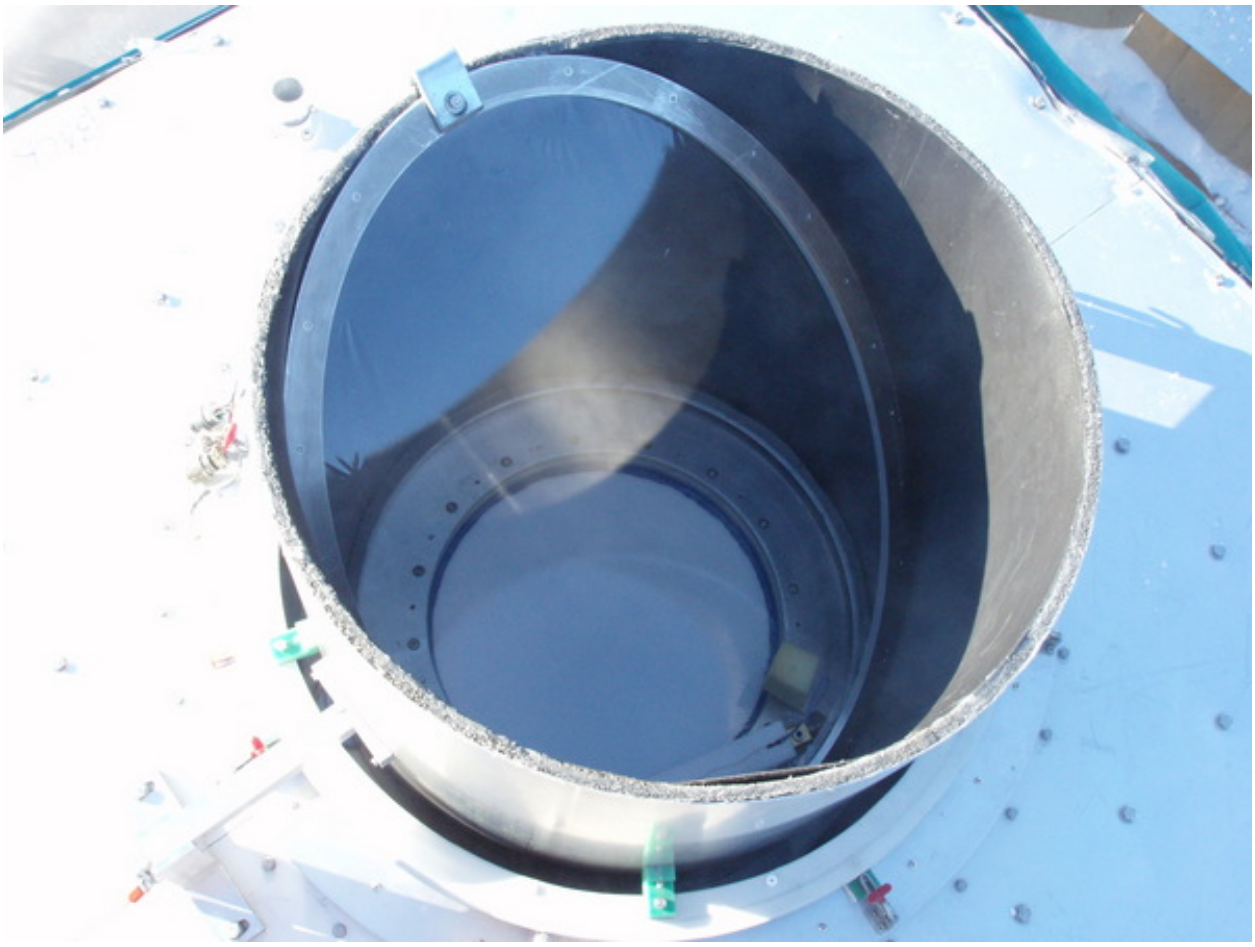

Figure 3.10: Dielectric sheet calibrator for measuring PSB orientations consists of a beam-filling polypropylene sheet and an ambient load made of a highly emissive black lining, subjecting the beams to partially polarized radiation. The device is mounted on the azimuth stage, which can rotate about the telescope's boresight when pointed at zenith.

With an 18-μm polypropylene film and a typical temperatures of $T_{\rm H} = 220$ K and $T_{\rm C} = 10$ K, the signal amplitude is $\sim$100 mK at 100 GHz and $\sim$250 mK at 150 GHz, small enough to ensure that the bolometer response remains linear (Figure 3.9).

This rotatable calibration device needed to not only work mechanically in extremely low temperatures, but also be simple to set up and operate safely by a human in the cold and the dark. The bearing for the rotation stage needed a special type of grease[4] that continues to perform at South Pole temperatures. Prior to field deployment, I tested the device using a large refrigerator that cooled to -70 °C. Also, I designed the device to be easy to handle even with thick gloves and bulky gears. Finally, I tried to design the calibration procedures with maximal automation and minimal necessity for outdoor labor. As discussed in §4.4, this calibration device worked well, allowing us to measure polarization angles with 0.1° rms repeatability.

3.4 Motion control system

The receiver is supported in an azimuth-elevation (AZ-EL) mount with a third degree of rotational freedom about the boresight. For reliable operation at the South Pole, the telescope mount design (Figure 2.1) keeps indoor all serviceable components except for the receiver window itself. The mount allows telescope steering and tracking through a full range in azimuth (400°), elevation ($50° - 90°$), and continuous rotation about the boresight.

The mount stands on the upper floor of the Dark Sector Laboratory. The telescope observes through the roof and is sealed against the building with a flexible enclosure, leaving most of the instrument accessible in a room temperature environment. The insulated fabric bellows permits motion in the elevation axis and together with brush seals at the azimuth and boresight axes forms an environmental seal that maintains at room temperature the cryostat, control electronics, and mount drive assemblies. The enclosed laboratory space is kept at a slight positive pressure, so that a constant outward air flow through the brush seals and special vents directed toward the window eliminates ice buildup there.

We engineered and fabricated the BICEP mount in cooperation with TripointGlobal / VertexRSI. Lightweight box steel construction offers extreme rigidity and immunity to flexure; the combined mass of the telescope, when fully equipped and operational, is 3400 kg. It is supported on a steel and wood platform attached to the structural beams of the building. Continuous tilt monitoring and periodic star pointing have confirmed short term stability and blind pointing accuracy of the combined mount/platform structure to meet our pointing specification of $< 20''$. Long term drifts of $\sim 1'$/month appear to be dominated by settling of the building.

The mount allows rapid scanning, up to 5°/s, about the azimuth and boresight axes while maintaining precise pointing with minimal vibration. These axes employ ultra-quiet crossed roller bearings and gearless cycloidal motor reducers. Integrated testing with the BICEP receiver drove a choice of toothed belt drives for the azimuth and boresight axes, further reducing high drive speed microphonic excitation to levels well below our detector noise floor.

[4]MOLYKOTE 33 `http://www.dowcorning.com/applications/search/default.aspx?R=387EN`

Figure 3.11: 3-axis telescope mount, interlock system, and manual controller.

I worked with John Kovac to integrate the amplifiers, motors, and encoders. I built a manual controller and a safety interlock system to be used with limit switches and emergency stops (Figure 3.11 and 3.12).

3.5 Optical star-pointing camera

Pointing errors greater than 1% of the Gaussian beam width could contaminate polarization at the $r{\sim}10^{-4}$ level [17]. Although this effect is far below BICEP's sensitivity target, we developed a star-pointing camera to achieve a 1% accuracy, or $10''$, to be able to compare maps with *WMAP* and *Planck*. Such an accurate derivation of the sky coordinates from the telescope's axis encoder readings requires a precise knowledge of the dynamic state of the mount, including flexure, axis tilts, and encoder offsets. Encoder coordinates for the three mount axes are recorded synchronously with the bolometer timestreams and get translated to sky coordinates using a pointing model.

The pointing model was established using a compact optical star-pointing camera with a $2''$ resolution mounted beside the main window on top of the cryostat and co-aligned with the boresight rotation axis (Figure 3.13). There are 10 dynamic parameters: AZ

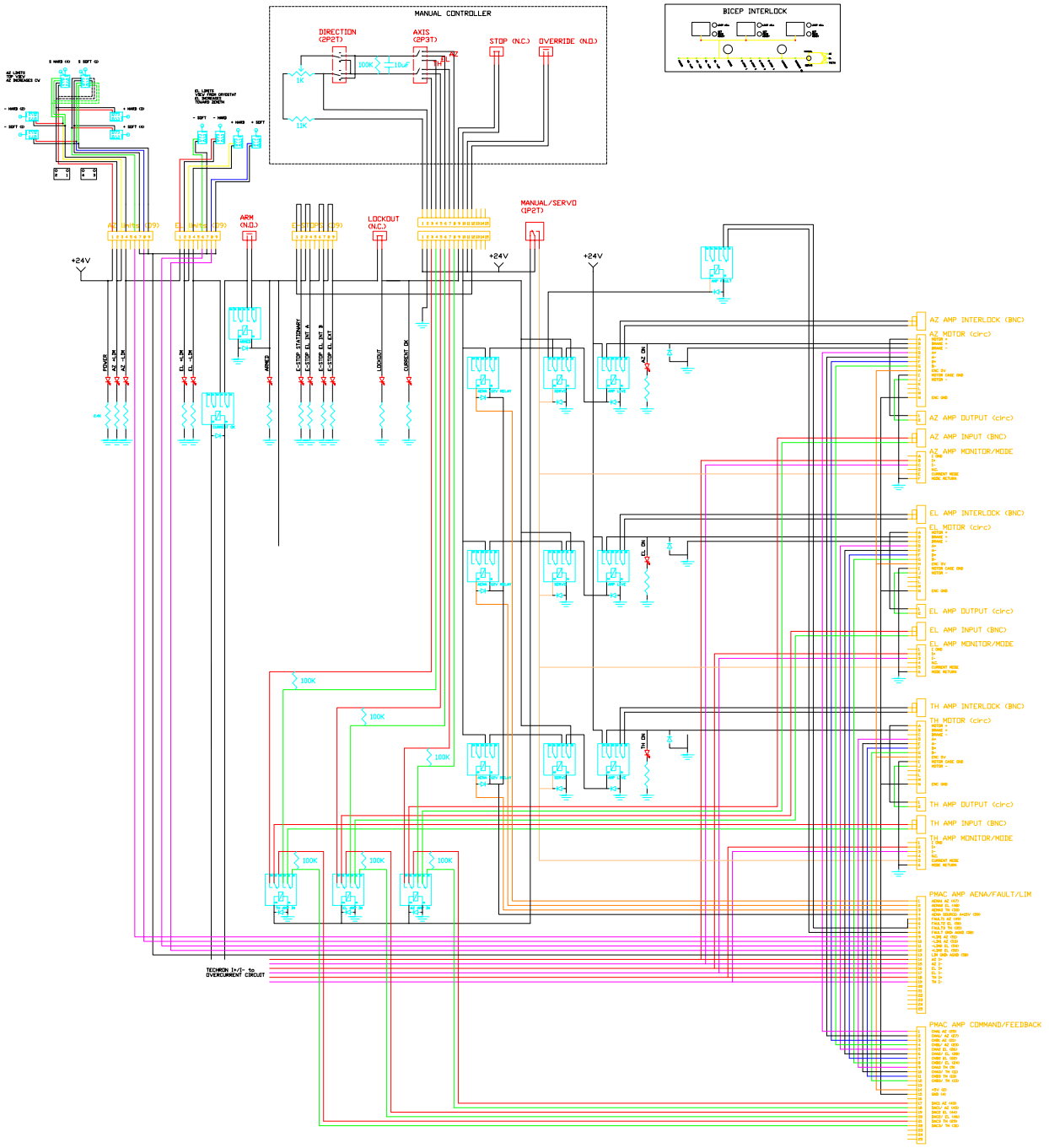

Figure 3.12: Motion control interlock scheme

axis tilt magnitude and direction, EL axis tilt, the 3 encoder zeros, amount of telescope flexure $\propto \cos(EL)$ and $\propto \sin(EL)$, and magnitude and direction of the collimation error of the pointing camera itself. Since there are 10 dynamic parameters, a complete calibration requires observation of at least 20 stars.

To establish a pointing model during the Antarctic summer, we designed the pointing camera to be sensitive enough to detect magnitude +3 stars in daylight. For maximum contrast against the blue sky, we used a sensor with enhanced near infrared sensitivity[5] and an infrared filter cutting off below 720 nm. We used a 100 mm diameter lens that was color-corrected and anti-reflection coated for 720–950 nm. Its 901 mm focal length results in a small 0.5° field of view to keep the sky background low. Careful adjustments of the CCD camera and the mirrors reduced the optical camera's collimation error to 2.4′. During our first Antarctic summer season, we successfully captured 26 stars down to magnitude +2.9 in an elevation range of 55°–90°. More details on the pointing calibration results are in §4.5.

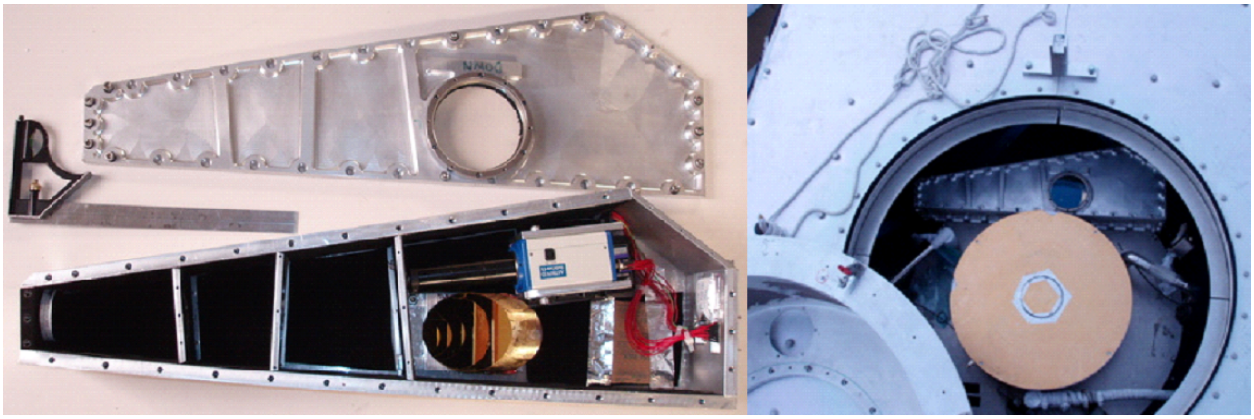

Figure 3.13: Optical star-pointing camera.

3.6 Refrigerator electronics

I was responsible for developing electronics related to keeping the detectors cold at 250 mK and electronics for driving the Faraday polarization modulators (innovative solid-state devices with no moving parts). I designed and produced compact printed circuit boards for operating the ^{3}He/^{3}He/^{4}He refrigerator (Figure 3.14), monitoring the temperatures of various cryogenic parts of the instrument and reading the LHe tank level. Electronics design for the South Pole involved considerations somewhat similar to those for space missions, including reliability, size restrictions, electrostatic protection in dry environment, and heat dissipation in low pressure.

Resistance thermometers are used to monitor the temperatures of the adsorption pumps, gas-gap heat switches, and evaporators for all 3 refrigerator stages, as well as the thermal strap to the focal plane, the center and edge of the 250 mK focal plane, and the 350 mK

[5]Astrovid StellaCam EX with EXview HAD CCD, `http://www.astrovid.com/prod\_details.php?pid=7`

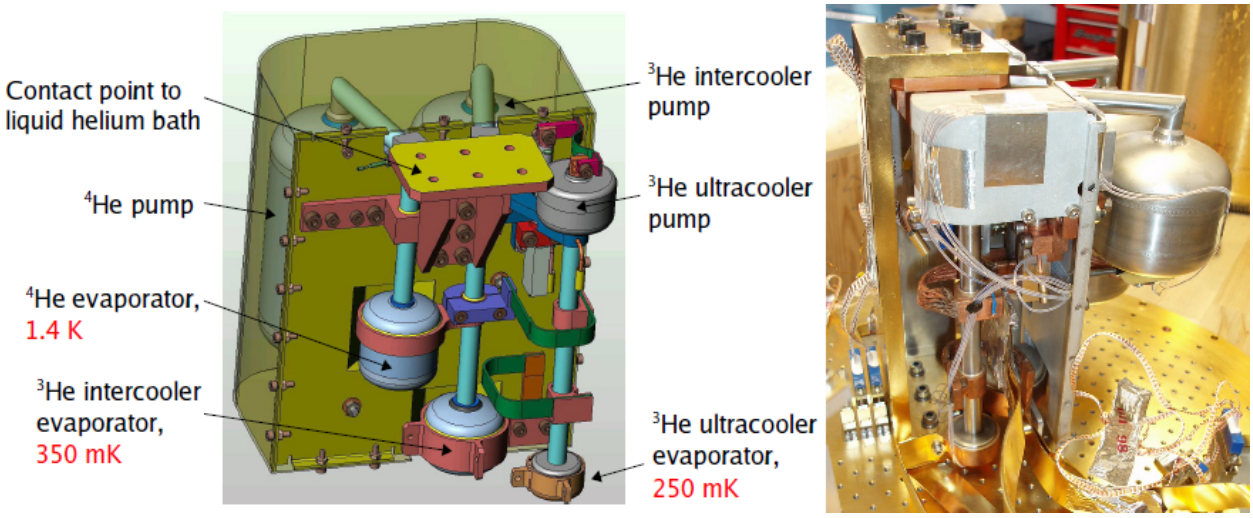

Figure 3.14: Three-stage adsorption refrigerator, showing the pump and evaporator of each stage (^{4}He, ^{3}He intercooler, and ^{3}He ultracooler). The large ^{4}He and ^{3}He intercooler adsorption pumps are cooled by gas-gap heat switches and housed in a light-tight shield. The small ^{3}He ultracooler pump is separately shielded. The adsorption unit mounts to the main LHe tank by a copper flange (4 K contact), which connects directly to the ^{4}He condensation point.

intermediate buffer stage. These thermometers (Cernox and GRT) have resistance up to 100 kΩ at the lowest temperatures near 250 mK, so the readout must use minute excitation to prevent depositing too much heat. We used a 0.2 mV AC excitation, generating only about a pW of heat (Figure 3.15). This meant reading a 3 nA signal at a required 1% accuracy. Moreover, the circuit needed to be able to read out a wide range of thermometer resistances from 20 Ω to 100 kΩ at 1% accuracy and provide an analog output within the 0–5 V range to be converted to digital with a 12-bit resolution. To accommodate this dynamic range, I designed in an alternate output in logarithmic scale.

Resistors are used as heaters for operating the adsorption pumps and the heat switches, for controlling the temperature stability of the 350 mK and 250 mK focal plane stages, and for heating up the JFET amplifiers to its 130 K operational temperature (Figure 3.16). The LHe level sensor readout involves measuring the resistance of a filament in the tank that becomes superconducting when in contact with LHe (Figure 3.17).

The lack of water molecules in the air allows electrostatic charges to accumulate easily, increasing the likelihood of sparks that can damage electronics and other sensitive equipment. In designing electronic boards for telescope operations, we tied inputs and outputs to electrostatic discharge protection circuits.

Another factor that affects electronics designs is the thin air due to the 2800-m altitude. With less air molecules, the ability to dissipate heat is reduced, making computers and electronics susceptible to over heating. We had a tight constraint on the volume and mass for the electronics boards, forcing us to design small circuit boards, increasing the heat mitigation challenge. I calculated the expected heat dissipation and incorporated generous

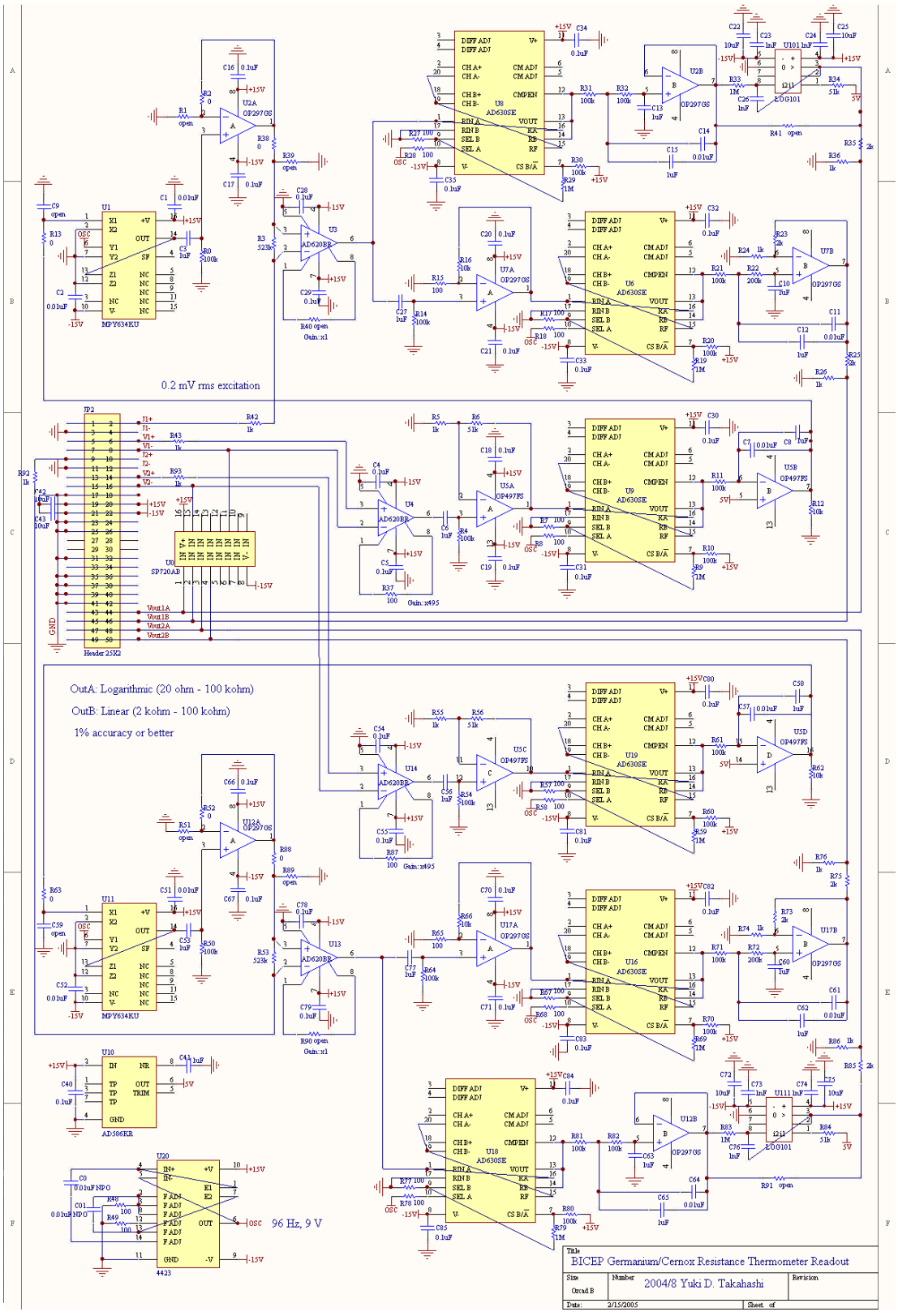

Figure 3.15: Electronics schematic for resistance thermometer readout.

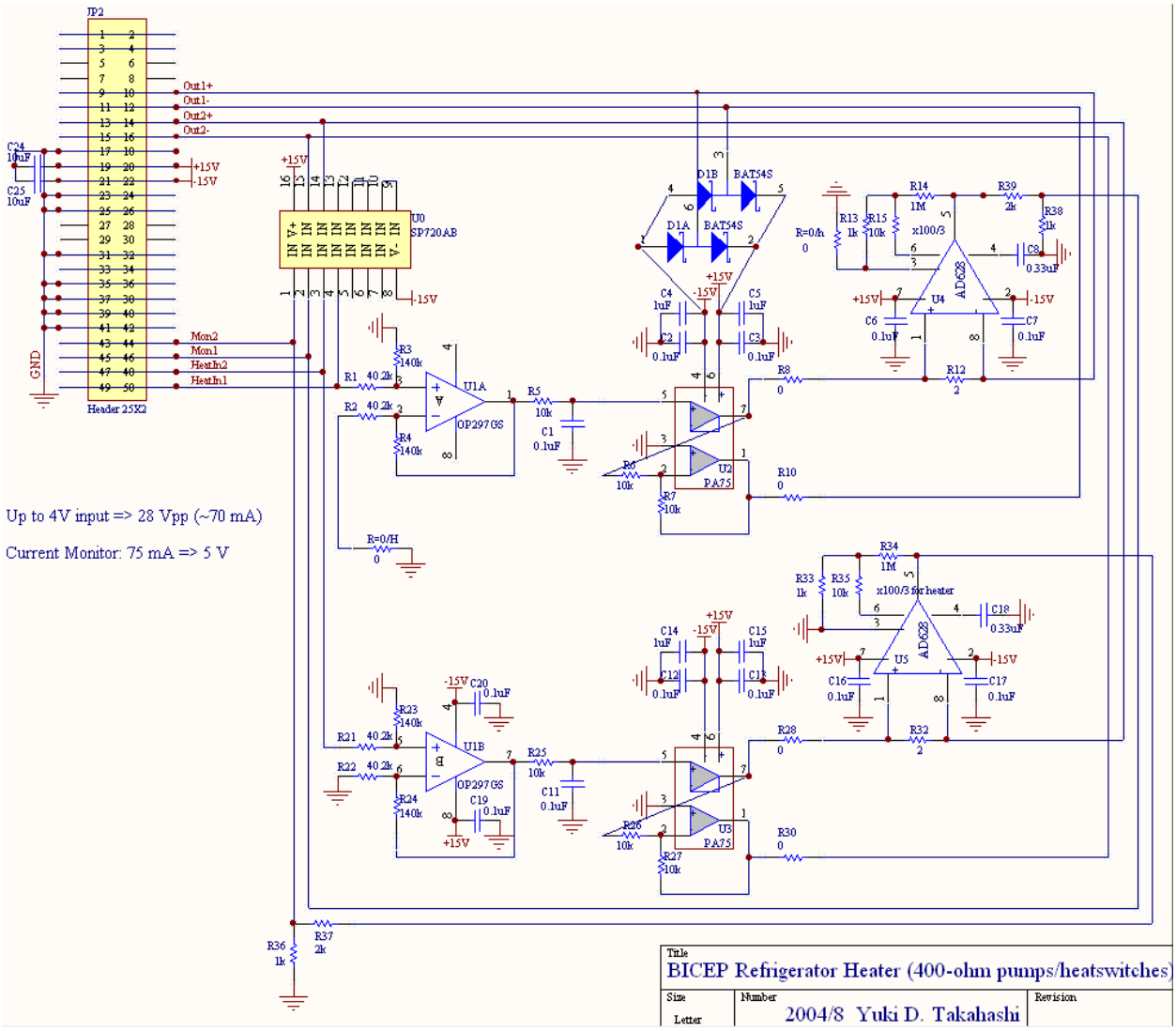

Figure 3.16: Electronics schematic for heater drivers.

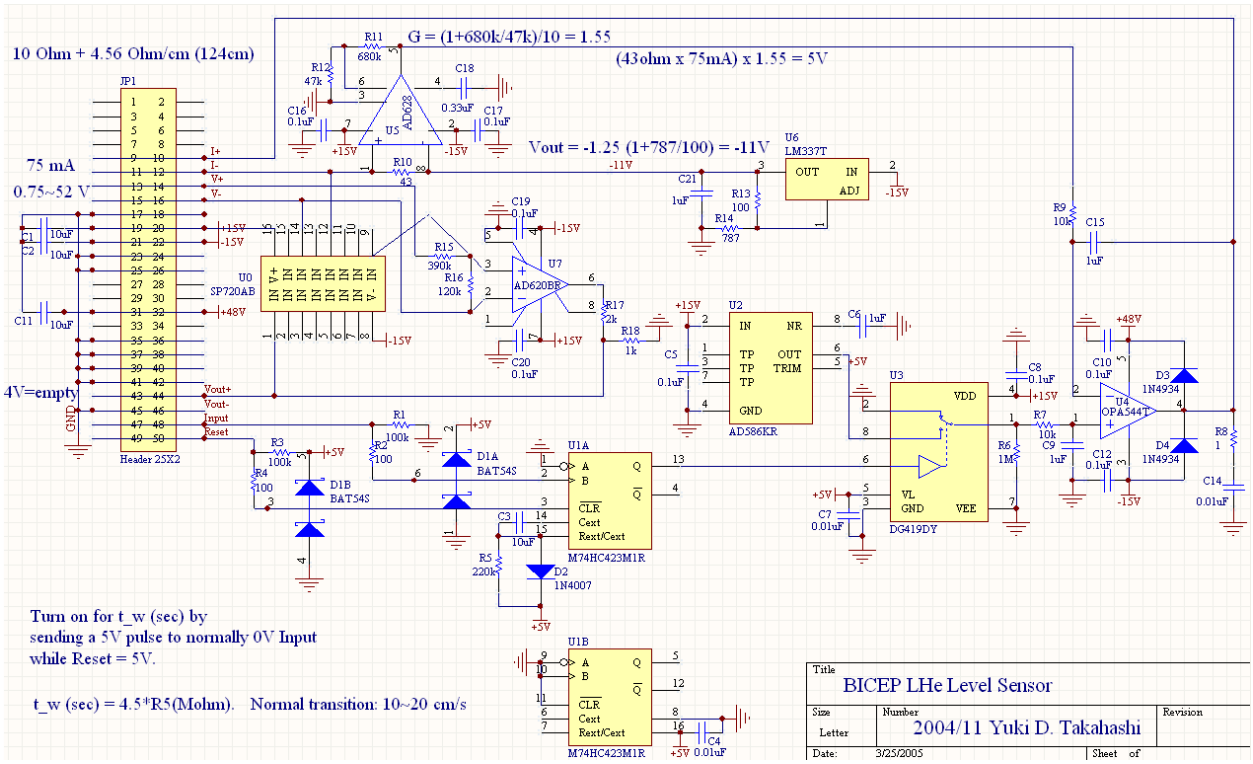

Figure 3.17: Electronics schematic for LHe level sensor readout.

amounts of heat sinking. Copper's thermal conductivity is ∼4 W/cm/K. With the power amplifier (like PA75) dissipating 4 W, the temperature gradient was expected to be ∼40 K/cm for 3-cm wide 76-μm thick copper layer (ignoring dissipation into the air). To prevent high temperatures, I included a heat sink as well as a large exposed ground plane.

Figure 3.18 shows the three boards. All the boards worked well for all 3 years without requiring any replacement, and the same cards or designs are used in next generation experiments like BICEP2 and Keck Array.

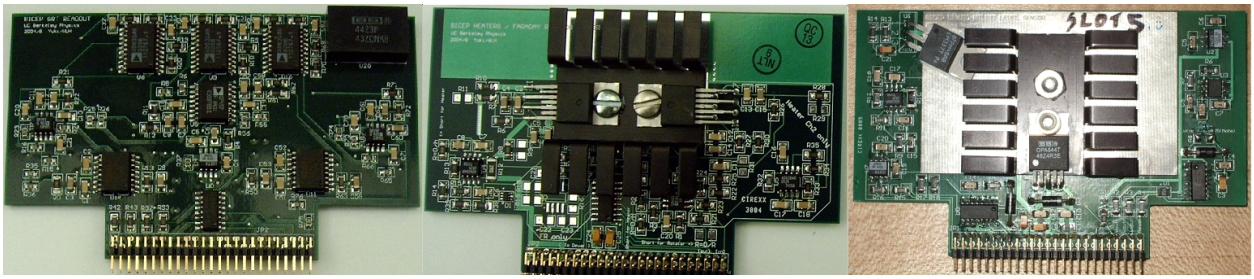

Figure 3.18: Front side of GRT readout, heater driver, and LHe level sensor readout boards.

3.7 Deployment

The BICEP mount was installed at the South Pole in November 2005, the cryostat was first cooled in December, and the instrument captured first astronomical light a month later. Following calibration measurements and tests of the observing strategy, BICEP began CMB observations in February 2006. The instrument operated nearly continuously until December 2008, when it was decommissioned to prepare for its replacement by BICEP2 on the same mount in late 2009. I had the privilege to work at the South Pole for a total of 8.5 months, from setting up a laboratory in an empty new building to shutting down the observatory after 3 years of observations and taking down the instrument.

Table 3.4: BICEP deployment timeline

2005/10/15	Shipped out the instrument.
2005/11/15	First crew to South Pole.
2005/11/30	Telescope mount installed.
2005/12/20	Cryostat mounted.
2006/ 1/15	First light (on Eta Carina).
2006/ 2/15	Began CMB mapping.

Chapter 4

Instrument characterization

BICEP was designed to be capable of measuring a polarization signal of 0.08 μK rms at $\ell\sim100$ corresponding to the BB signal expected for a tensor-to-scalar ratio of r=0.1. The CMB temperature anisotropy has much larger amplitude of $\sim$50 μK rms at these angular scales, and imperfect rejection of it in the polarization measurement could result in a residual false signal. In addition, errors in polarization orientations and pointing could mix the $\sim$1 μK E-mode CMB polarization signal into spurious B-modes. This experiment therefore requires careful instrument characterization and calibration to minimize systematic contamination in the polarization measurement.

The instrumental characterization reported here shows that all studied sources of potential systematic errors are controlled at the $r\approx0.1$ level and are not a limiting factor in our analysis. In fact, most sources contribute to the uncertainty in the measurement at a level of $r \lesssim 0.01$. The error sources that we have been able to control to this level include differential beam size, differential ellipticity, polarization orientation uncertainty, telescope pointing, sidelobes, and thermal stability. The three largest sources of systematic error are pair relative gains, differential pointing, and possibly the noise estimation, and may require more sophisticated removal or analysis techniques in the future. In addition, properties that impact the overall calibration of the polarization spectra, including the absolute gain, cross-polarization response, and relative polarization orientation, have been characterized well enough to ensure that calibration uncertainty is a small fraction of our error budget.

Of the largest three error sources, the noise has been estimated with sufficient accuracy to limit the uncertainty contribution to $r < 0.1$, a number that will improve asb we add more dat. The differential pointing of the PSB pairs is small enough to meet our r=0.1 benchmark without correction, but will need to be taken into account to achieve lower limits on r. The current uncertainty in the method we use to verify our calibration of the PSB pair relative gains leads to an upper limit in possible error on r that slightly exceeds our r=0.1 benchmark. The uncertainty will improve as we include more data, and a different approach may be needed if we measure any significant relative gain errors. By employing a more sophisticated analysis that allows for imperfectly-corrected relative gains of the PSB pairs and that includes the measured differential pointing, we expect to be able to control all studied sources of potential systematic errors to levels far below r=0.1.

The first section describes the simulations that determine the impact of the instrumental parameter characterization on the cosmological results. The remaining sections describe each of the instrumental properties and how we calibrate them.

4.1 Calibration goals and systematic error simulation

To process the timestreams into co-added polarization maps with systematic errors tolerable for our target sensitivity, an accurate characterization of the detectors and their beams is essential. Imperfections in the experiment and its characterization can result in false B-mode polarization signal. Many of these systematic effects depend in a complex way on the scan strategy, so analytic estimates of the impact of an instrumental uncertainty on the final power spectra serve only as a rough guide. Using the actual analysis pipelines, we have simulated the most significant instrumental uncertainties to establish benchmarks for how precisely we must measure each property. Table 4.1 summarizes the results. Table 4.2 summarizes calibration uncertainties that affect only the power spectrum amplitudes but do not cause false polarization signals.

We are most concerned with systematic errors that mix temperature anisotropy and E-mode polarization signals into B-mode polarization. Instrumental properties that must be characterized are discussed in detail in the following sections. The response of a PSB to radiation characterized by Stokes $\{T, Q, U\}$, which are functions of frequency ν and direction Ω, can be modeled as:

$$d(t) = K_t * \left\{ n(t) + g \int d\nu A_e F(\nu) \int d\Omega \; P(\Omega)[T + \frac{1-\epsilon}{1+\epsilon}(Q\cos 2\psi + U \sin 2\psi)] \right\}, \quad (4.1)$$

where ψ is the polarization orientation angle of the PSB, ϵ is the cross-polarization response, $P(\Omega)$ is the beam function, $F(\nu)$ is the spectral response, A_e is the effective antenna area, g is the DC responsivity, $n(t)$ is noise, and K_t is the time-domain impulse response associated with the detector's frequency transfer function. The temporal response function of each bolometer must be measured to deconvolve it from the raw timestream. Then the relative gain of each PSB pair must be determined for differencing. Since we derive relative gains from atmospheric signal in elevation nods, we must verify that each PSB pair has well matched spectral response. In addition, pair differencing requires that the two PSBs have well matched beam shapes and pointing. Finally, construction of the polarization map requires the knowledge of the detector polarization angles and the telescope pointing.

We established our calibration benchmarks based on BICEP's design goal to be capable of measuring polarization down to levels corresponding to a tensor-to-scalar ratio r=0.1 without being limited by systematic effects. At r=0.1, the B-mode polarization power spectrum, C_ℓ^{BB}, would have a peak amplitude of $\ell(\ell+1)C_\ell^{BB}/2\pi = 0.007\ \mu\mathrm{K}^2$ at $\ell = 70$–110. The benchmarks for the instrumental properties and characterization correspond to the values that result in spurious B-mode signal at the level of r=0.1 in the simulations.

The simulation procedure uses the same data processing pipelines as the main CMB power spectrum analysis, and is basically identical to the signal-only simulations used in determining the ℓ-space filter function. We verified the simulation results using our two independent pipelines: one using QUAD's pseudo-C_ℓ estimator on a flat sky, and the other using `Spice` [6] on a curved sky.

We began the procedure with a ΛCDM model generated by `CAMB` [29], using cosmological parameters derived from *WMAP* 5-year data [16] and r=0. From this model, we generated an ensemble of simulated CMB skies using `synfast` [13]. We then simulated observations of

Table 4.1: Systematic errors potentially producing false B-mode polarization

	Benchmark [a]	Measured	Reference
Relative gain uncertainty: $\Delta(g_1/g_2)/(g_1/g_2)$	0.9%	$< 1.1\%$ [b,c]	§4.2
Differential pointing: $(\mathbf{r_1} - \mathbf{r_2})/\sigma$ [d]	1.9%	1.3% [e]	§4.3
Differential beam size: $(\sigma_1 - \sigma_2)/\sigma$	3.6%	$< 0.3\%$ [b]	§4.3
Differential ellipticity: $(e_1 - e_2)/2$	1.5%	$< 0.2\%$ [b]	§4.3
Polarization orientation uncertainty: $\Delta\psi$	2.3°	$< 0.7°$ [b]	§4.4
Telescope pointing uncertainty: $\Delta\mathbf{b}$	$5'$	$0.2'$ [f]	§4.5
Polarized sidelobes (100, 150 GHz)	-9, -4 dBi	-26, -17 dBi [g]	§4.6
Focal plane temperature stability: $\Delta T_{\rm FP}$	3 nK	1 nK [h]	§4.7
Optics temperature stability: $\Delta T_{\rm RJ}$	4 μK	0.7 μK [h]	§4.7

[a] Benchmarks correspond to values that result in a false B-mode signal of at most r=0.1 and are all lower limits. For r=0.01, all benchmarks would be lower by $\sqrt{10}$.

[b] Upper limit, rms error over the array.

[c] If relative gain errors are detected, we anticipate removing their effects in future analyses using a CMB temperature template map.

[d] $\sigma = FWHM/\sqrt{8\ln(2)} = \{0.39°, 0.26°\}$ at {100, 150} GHz.

[e] Average, each repeatedly characterized to 0.4% precision. This measurement of differential pointing could be used in future analyses to remove the small predicted leakage of CMB temperature into polarization maps.

[f] Fit residual rms in optical star pointing calibration.

[g] Response at 30° from the beam center.

[h] Scan-synchronous rms fluctuation on $\ell\sim100$ time scale.

Table 4.2: Calibration uncertainties affecting the power spectrum amplitudes only

	Benchmark[a]	Measured
Absolute gain $\Delta g/g$	5%	2%
Cross-polarization response $\Delta\epsilon$	0.026	0.01
Relative polarization orientation $\Delta(\psi_1 - \psi_2)$	9°	0.1°

[a] Benchmarks correspond to 10% uncertainty in the polarization power spectrum amplitude.

the BICEP field on these `synfast` skies using pointing data from the actual scan patterns. We varied instrumental parameters for the PSB pairs with a distribution across the array corresponding to the given uncertainty, but constant in time. For differential pointing, we used the actual measured quantities in the simulations.

To simulate the coupling between non-ideal beams and the sky, we followed the formalism in [4]. A PSB timestream sample is expressed as a convolution of the beam with a second-order Taylor expansion of the sky signal around the pointing center – the first and second derivatives of simulated T, Q, and U maps are calculated with `synfast`. This technique enables quick simulation of the beam convolution while using the exact scan trajectory of each detector, which is essential in quantifying the beam mismatch effects, as these depend on the scan strategy and on the combination of detectors with different characteristics. This

formalism also allows simulation of the impact of uncertainties in the knowledge of PSB orientations and cross-polarization response.

We performed the simulated observation at each of the 4 boresight rotation angles and with the appropriate instrument configuration for each observing year. We fed the simulated signal-only timestreams through the pipelines to be filtered and co-added into maps with exactly the same weights as with the real data. A baseline set of spectra were computed without any simulated errors to (1) determine the amount of E-B leakage due to timestream filtering and any other effects intrinsic to the pipeline, and (2) obtain the transfer functions to be applied to the raw spectra.

We compared the power spectra of maps made with simulated errors with those without any errors, and attributed any differences to systematic errors – in particular, excess B-mode polarization power that has leaked from T or E. We performed the simulations with at least 10 realizations of input CMB maps.

Table 4.1 summarizes the instrument properties and r=0.1 benchmark levels for their characterization, as well as the results of measurements described in the following sections. We have succeeded in characterizing each instrumental property to a level of precision at least comparable to the r=0.1 benchmark and in most cases much better.

Finally, some calibration uncertainties affect only the scaling of the spectra but do not result in spurious polarization signals (Table 4.2). We calculated these effects analytically, as described in the following sections. We set the benchmark for each of these uncertainties such that the contribution to the calibration of power spectrum amplitudes is $\Delta C_\ell/C_\ell \leq 10\%$, a standard easily met by our instrument characterization.

We used the benchmarks found in the previous section to guide our program of characterizing the instrumental performance. To reach the required level of precision, we designed and implemented a number of techniques for the calibration measurements. The following sections describe the measurements for relative gain calibrations, beam characterization, polarization calibration, telescope pointing, far sidelobes, and thermal stability and compares the results with the benchmark values leading to a reference level of uncertainty in BB power spectrum. The characterization of the instrument noise and its implications for uncertainty in the power spectrum is discussed in §5.4. We have measured all the instrumental quantities with sufficient accuracy for the sensitivity achieved with the first 2 years of data.

4.2 Relative detector gains

Polarization measurement with BICEP relies on PSB pair differencing. We must thus determine the relative gains within each pair accurately to prevent unpolarized signal from leaking into the polarization measurement. The relative amplitudes of the CMB temperature and polarization anisotropies place stringent requirements on the relative gain calibration of the differenced detectors. Simulations of relative gain errors suggest that the level of false polarization depends strongly on how gain errors are distributed across the PSB array. With the best estimated distribution of the measured gain uncertainties described in §4.2.2, the simulations indicate that relative gains need to be accurate to 0.9% rms to limit the leakage of CMB temperature anisotropy into B-mode power at a level corresponding to r=0.1.

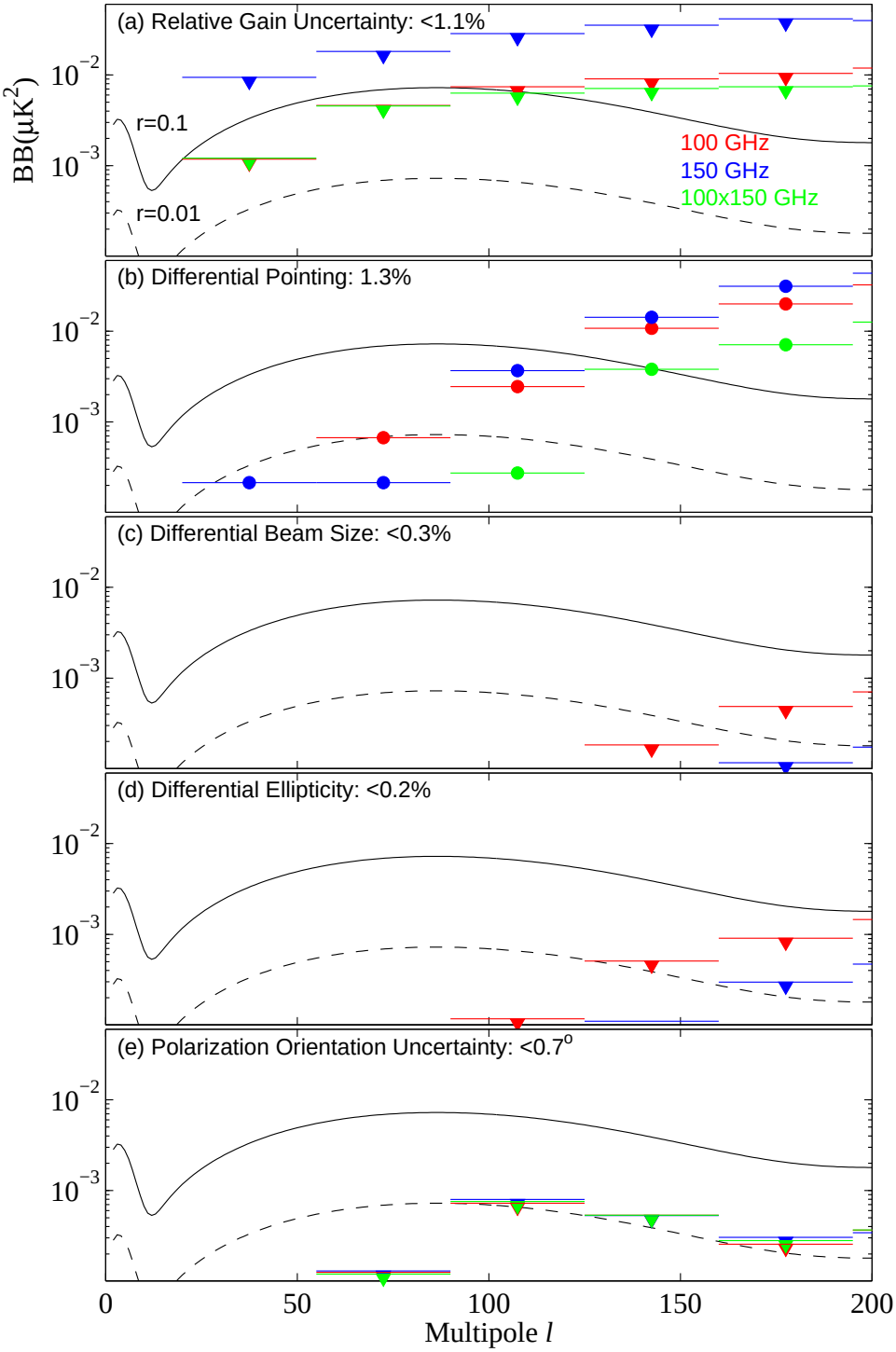

Figure 4.1: Spurious BB power from simulations of measured potential systematic errors. Except for differential pointing, all BB estimates correspond to measured upper limits. Effects of relative gain error and differential pointing can be corrected for in the analysis if necessary. All the potential systematic uncertainties are measured to be well below the 2-year constraint of $r < 0.72$ [5].

We corrected for relative gain differences in two steps, first by deconvolving the temporal transfer function of each PSB to account for frequency-dependent gains, and then by correcting for the DC gains through elevation nods. Since elevation nods use the atmospheric emission, which has a different emission spectrum than the CMB temperature fluctuations, the spectral response of each PSB in a pair must be precisely matched. We measured the detector transfer functions each year, calibrated the DC gains hourly with elevation nods, and made spectral response measurements once before deployment and once in the field. The following subsections describe the measurements of temporal transfer function, DC responsivities, and spectral response. We measured the transfer functions for each pair to within 0.3% uncertainty and elevation nod relative gains to within 1.1% rms uncertainty over the PSB pairs. While the current upper limit on the possible relative gain errors slightly exceeds the 0.9% benchmark for r=0.1, this effect is not significant for BICEP's 2-year CMB results; furthermore, if a significant signal is detected it could be corrected with a more sophisticated analysis.

4.2.1 Temporal transfer functions

Analysis of the time series from each detector begins by deconvolving the temporal response using the measured frequency-domain optical transfer function of the detector. Since the transfer function is proportional to the gain of the detector as a function of frequency, it directly affects the relative gains of a PSB pair to be differenced. We thus had to measure the relative transfer functions with errors below the 0.9% benchmark set for the relative gains.

At the nominal scan speed of 2.8°/s in azimuth at ∼60° elevations, our target angular scales of $\ell = 30$–300 fall into 0.1–1 Hz frequency band. Since the elevation nods described in the next section are sensitive to relative fluctuations at ∼0.02 Hz, we measured the transfer functions down to 0.01 Hz.

The primary measurement technique involved analyzing the step response to a fast-switched square-wave source (Gunn oscillator or broadband noise source) operating at 0.01 Hz, while under optical loading conditions representative of CMB observations (Figure 4.2). We explored possible dependence on background loading and detector non-linearity by repeating the measurement with extra loading from sheets of emissive foam placed in the beam in combination with different signal strengths. To obtain the transfer function for each detector, we averaged the ratio of the Fourier transforms of the time-domain detector response and of the input square wave. Figure 4.3 shows the measured transfer functions for representative and anomalous PSBs; they were stable against different combinations of loading and signal levels.

The relative gain uncertainty due to measurement uncertainty was found to be <0.3% over the frequency range of 0.01–1 Hz. The measured transfer functions fit the following model as a function of frequency ω,

$$\tilde{K}(\omega) \propto \frac{1-\alpha}{(1-i\omega\tau_1)(1-i\omega\tau_2)} + \frac{\alpha}{(1-i\omega\tau_\alpha)}, \tag{4.2}$$

where $\tau_{1,2,\alpha}$ are time constants and α is the fractional amount of a slow additive component. We however measured the transfer functions with sufficiently high signal-to-noise ratio (S/N)

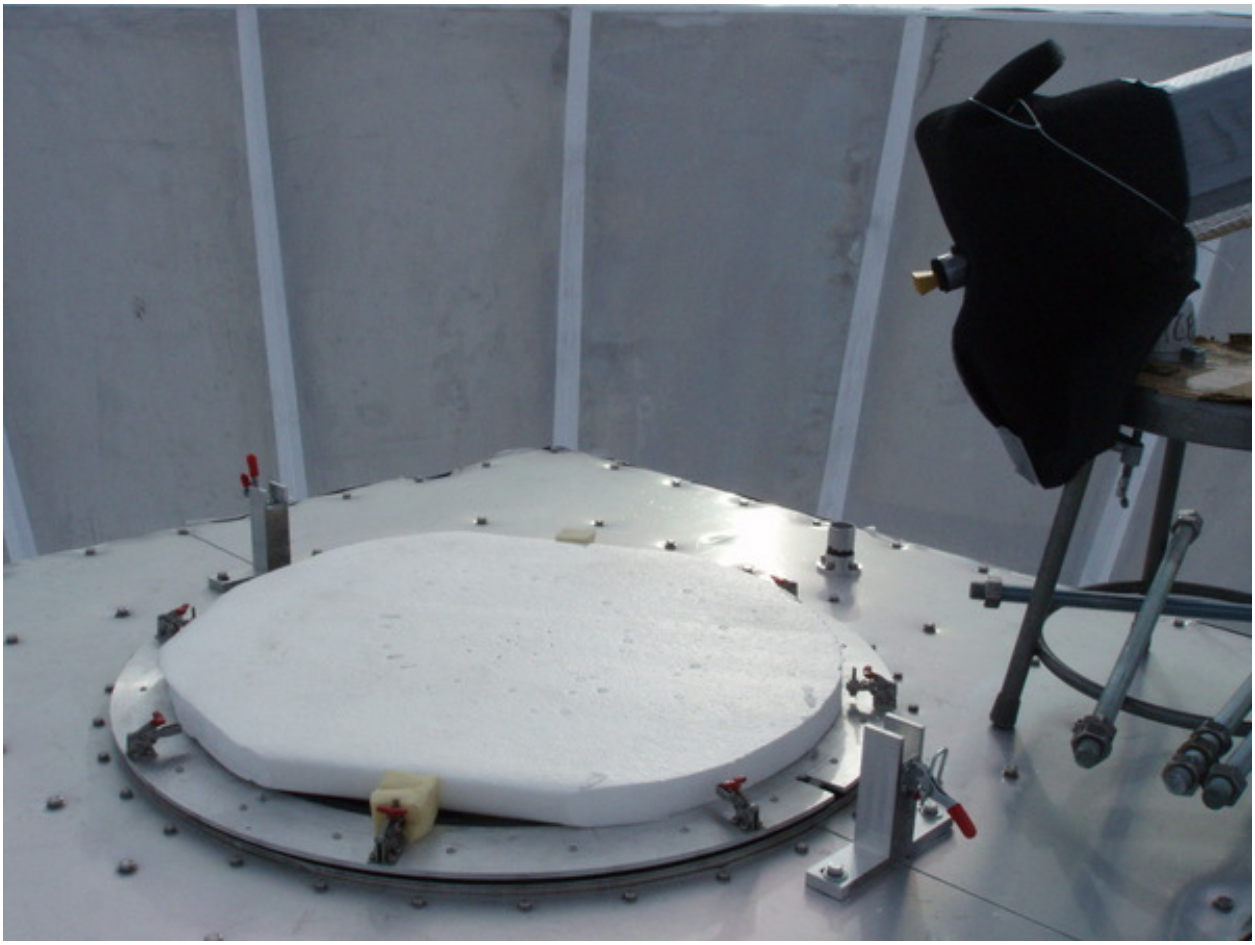

Figure 4.2: Fast-switched source in front of the telescope aperture used for the measurement of temporal transfer functions. Metal washers were embedded in transparent polypropylene foam sheet to scatter the PIN-switched broadband noise source signal (from upper right) into the beam while keeping the total optical loading similar to that during nominal CMB observations.

so that we could directly inverse Fourier transform them to define the deconvolution kernels. The median time constants were $\tau_1 \approx 20$ ms and $\tau_2 \approx 5$ ms, and τ_α was generally 100–200 ms with α typically <0.05. From the first observing year, we excluded 6 bolometers at 150 GHz from CMB analysis due to excessive roll off between 0.01 and 0.1 Hz (large α and τ_α). Two of the worst were in a single PSB pair and we replaced them at the end of the year.

Between the first two observing years, the transfer function measurements generally agreed to within 0.5% rms across the signal band. Two exceptions were excluded from the first year CMB data where the transfer functions were less well constrained at low frequencies. Details of the measurements and analysis are in Ki Won's thesis [52].

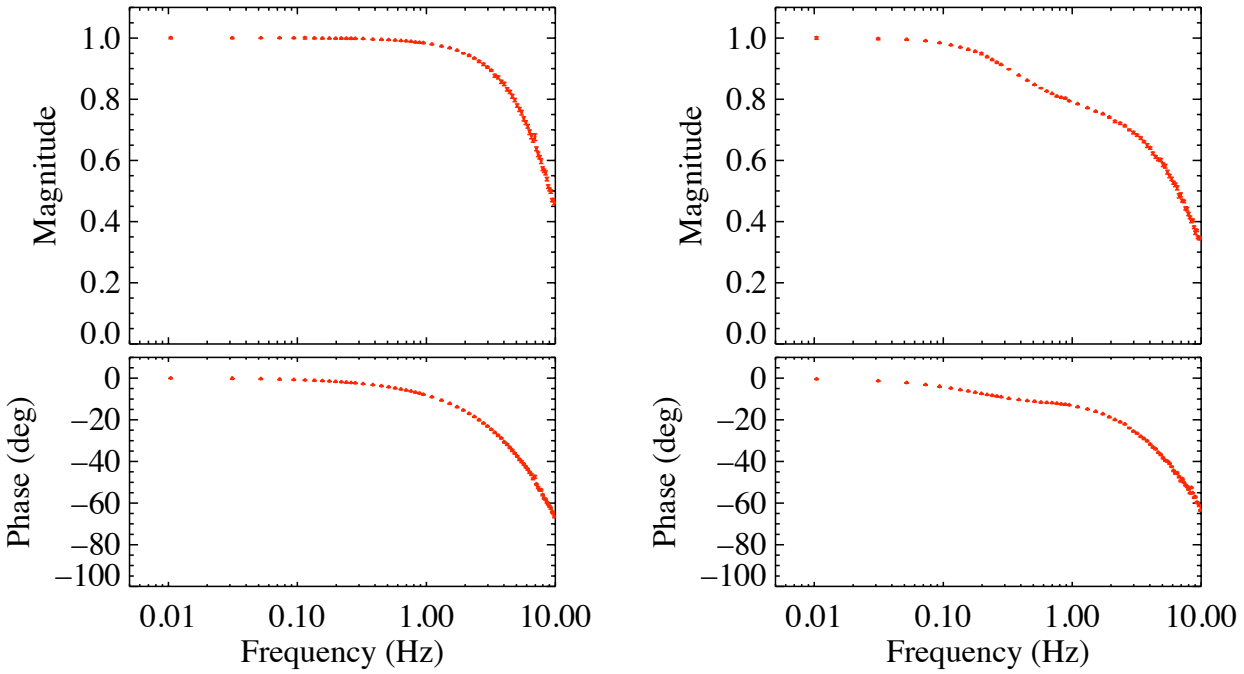

Figure 4.3: Measured transfer functions for a representative PSB (left) and an anomalous PSB (right), with error bars showing rms measurement repeatability. Most of the anomalous transfer functions were well characterized by Equation 4.2 and the measurements were repeatable, but we have conservatively excluded them from the initial analysis.

4.2.2 Relative responsivities

We derived relative gains using elevation nods performed at the beginning and end of every one-hour constant-elevation scan set (Figure 4.4). The telescope scanned in elevation with a rounded triangle wave pattern over a range of $\pm 0.6°$, varying the optical loading by $\sim \pm 0.1$ K due to the changing line-of-sight air mass. We fit the bolometer responses to a simple air mass model of atmospheric loading versus elevation, $T_{\rm atm} \propto \csc(EL)$, to derive the relative gains across the array.

We performed the elevation nod slowly over 50 s to limit thermal disturbances on the focal plane. During the nod, the diagnostic "dark" PSBs not illuminated through the feedhorns exhibited systematic voltage responses that were ∼0.4% of the typical responses of the illuminated PSBs, indicating thermal contamination at this level. To reduce the effect of the thermally-induced signals, we performed the two elevation nods for each scan set in opposite patterns (up-down-return and down-up-return) and averaged the response. While the two patterns resulted in a small systematic difference in the individual gains, the PSB pair *relative* gains were consistent to within the measurement noise of 0.6% rms.

PSB pair differencing is able to remove common-mode atmospheric fluctuations, and the relative gains were very stable (Figure 4.6). Even over a time scale of months, the measured relative gains were stable with ∼1% rms and exhibited no systematic variation with optical loading. I also tried computing relative gains by correlating timestream atmospheric

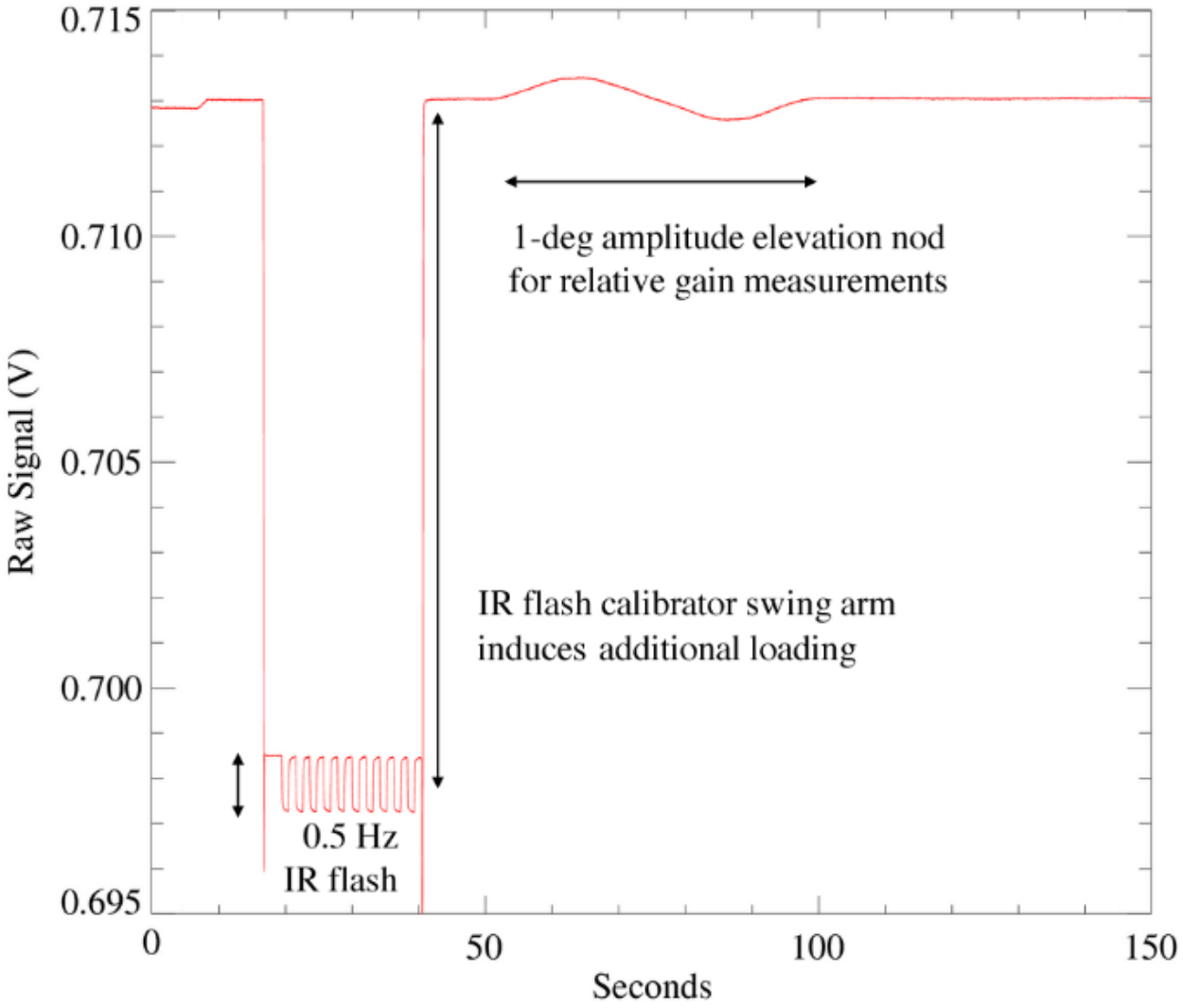

Figure 4.4: Bolometer timestream during a relative responsivity calibration procedure. An infrared source swings into the beam to inject a signal of very stable amplitude, useful for tracking any gain variations. The elevation nod uses the atmospheric loading variation.

fluctuations within PSB pairs, and the results were consistent with the elevation nods to within ±3%.

As an additional method to track gain variations, an infrared source supported by a foam paddle was swung into the beam to inject a signal of very stable amplitude [51] (visible in Figure 3.3). It produced a very repeatable (0.4% rms) response between the beginning and end of the one-hour scan sets and also showed that the individual gains are stable with 1% rms across the full elevation range. However, because of the ∼3 K optical loading introduced by the swing arm and unknown polarization of the infrared source, we have not used the relative gains from the flash calibrator for pair-differencing.

To quantify the level of leakage of the CMB temperature anisotropy into pair differences, we cross-correlated the individual PSB pair-sum and pair-difference maps. This analysis per-

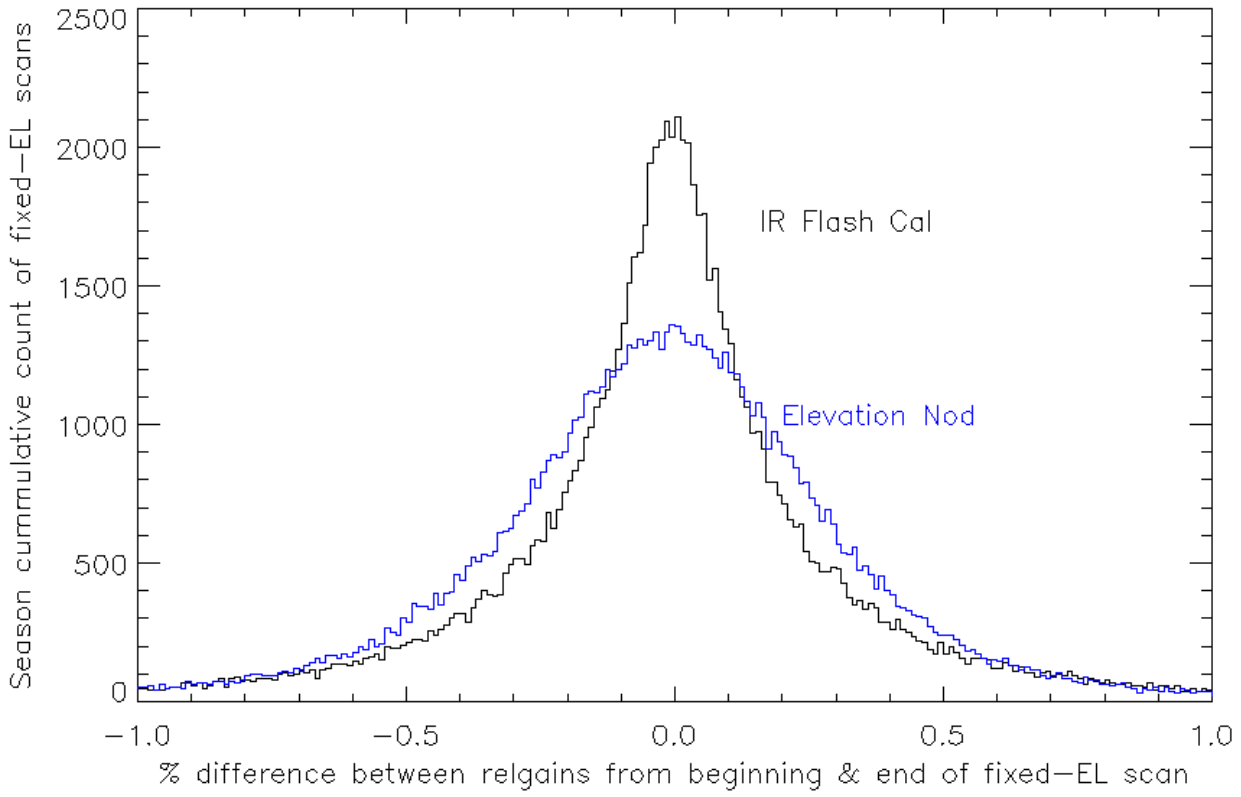

Figure 4.5: PSB pair relative responsivity was consistent to within 0.6% with elevation nods between the beginning and end of one-hour scan set. With the infrared flash calibrator, the measurements were consistent to within 0.4%.

formed on the yearly maps from the first 2 years showed no statistically significant evidence for relative gain errors in the data and placed an upper limit of <1.1% rms on the angular scales of interest. There is weak evidence that a small subset of PSB pairs, especially at 150 GHz, have excess sum-difference correlations. With the full 3-year data set, we anticipate placing tighter constraints on the gain uncertainties. The power spectra of spurious B-mode polarization due to the best-estimate distributions of 1.1% rms relative gain errors is plotted in Figure 4.1a. Although these upper limits exceed the signal for r=0.1 on some scales, especially for 150 GHz, this systematic effect is still well below the statistical error in the first 2 years of data. If measured, this leakage can be mitigated by projecting out a CMB temperature anisotropy template from the polarization maps.

The measured individual gains were scaled for each one-hour scan set such that the mean response of the detectors in each frequency band is constant. Finally, we derived the absolute gains for converting the detector voltage into CMB temperature units by cross-correlating CMB temperature anisotropy maps by BICEP and *WMAP*. As described in detail in [5], the BICEP map (in volts) and "BICEP-observed" *WMAP* maps (in K_{CMB}) were identically smoothed and filtered, and we computed the absolute gain g_ℓ for each of the frequency bands from cross-correlations in multipole space. Within the multipole range of $\ell = 56$–265, g_ℓ was nearly flat; the average was used as a single calibration factor for each frequency band.

The standard deviation of 2% is a conservative estimate of the absolute gain uncertainty in CMB temperature units. The results were consistent with those from the dielectric sheet calibrator (described in §4.4), which can provide a real time absolute calibration with a 10% uncertainty.

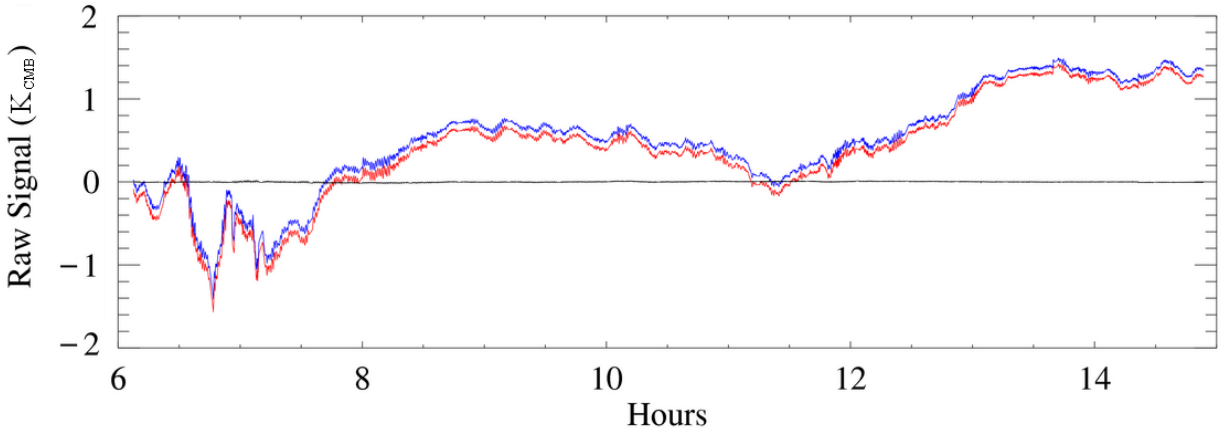

Figure 4.6: Individual 150 GHz timestreams within a PSB pair (red and blue) are differenced (black) in this plot using a single relative gain fit over the plotted 9-hour period. For the actual CMB analysis, we updated relative gains for every one-hour scan set.

4.2.3 Spectral response

As described above, the relative gain calibration of a PSB pair was based on the relative response of the detectors to the change in atmospheric loading from a small nod in elevation. Because the temperature derivative of the CMB and the atmospheric emission have different spectral shapes, the relative gain derived to match the response to elevation nods may not be optimal for the rejection of CMB temperature fluctuations.

We measured the spectral response of each detector channel using two separate polarized Fourier transform spectrometers with a maximum resolution of 0.3 GHz, once in the lab at Caltech and once in the field at the South Pole. Within each frequency band, the spectra were very similar from channel to channel (Figure 4.7 shows the average spectra), and the preliminary upper limit on the expected relative gain errors due to spectral mismatch was roughly 1% rms over the array. This upper limit does not rule out spectral mismatch as a source of possible relative gain errors in the small subset of PSB pairs.

In addition to the main band, we verified that there was no significant response at higher frequencies due to leaks in the low-pass filters. We used high-pass thick grill filters with cut-off frequencies of 165 and 255 GHz in front of the telescope aperture one at a time and measured the response to a chopped thermal source. 150 GHz channels showed no sign of leaks beyond 255 GHz down to the noise floor at -35 dB, while 100 GHz channels exhibited leaks at ~ -25 dB level above 255 GHz. The magnitude of this small ($\sim$0.3%) leak was consistent between the PSBs in each pair, so the effect on relative responsivities is expected to be negligible.

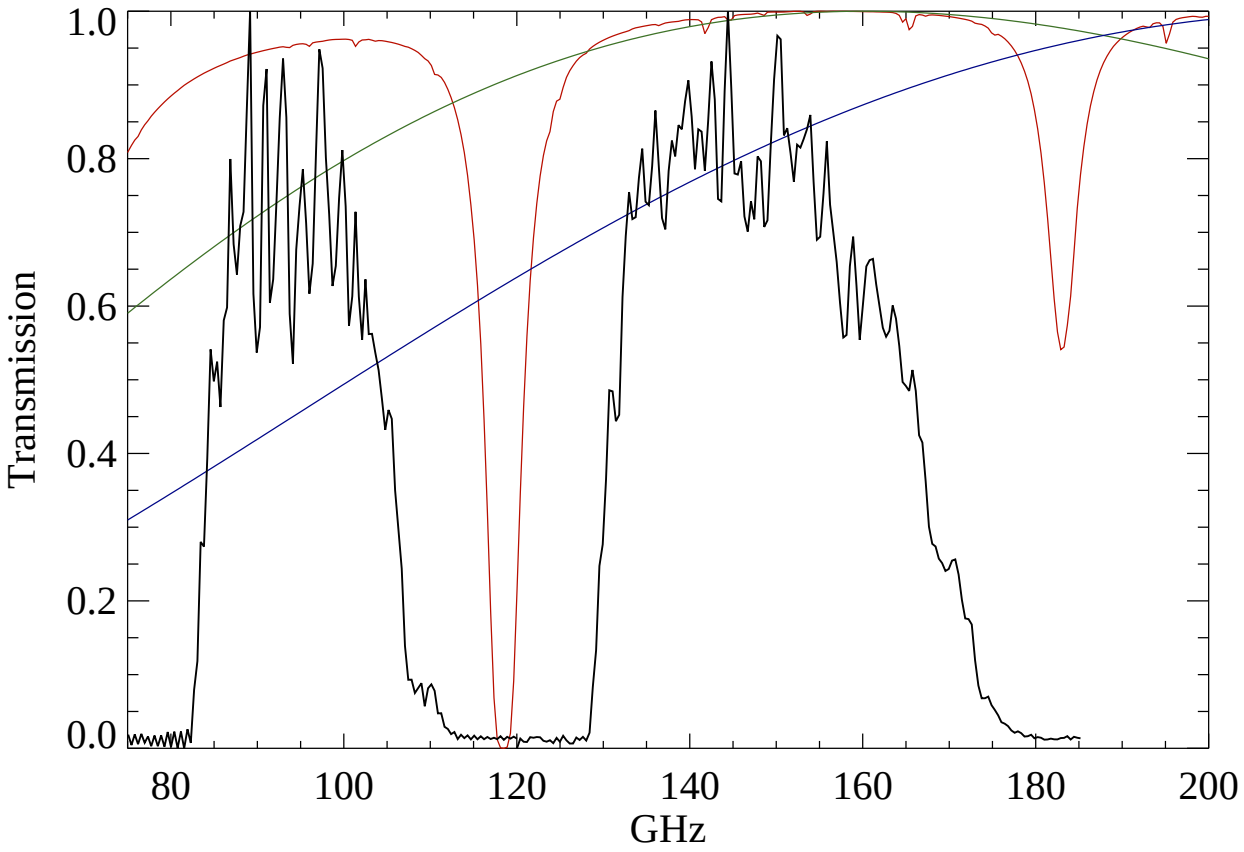

Figure 4.7: Average measured spectral response for each of BICEP's frequency bands, as a fraction of the maximum. Overplotted are the atmospheric transmission at the South Pole (red), the CMB spectrum (green), and its temperature derivative (blue).

4.3 Beam characterization

Mismatch in the beams of a PSB pair can result in a false polarization signal from unpolarized temperature anisotropies. Beam mismatches can also lead to mixing between E-mode and B-mode polarization. The difference between two nearly circular beams can be decomposed into three quantities corresponding to monopole, dipole, and quadrupole differentials: differential beam size $(\sigma_1 - \sigma_2)/\sigma$, differential pointing $(\mathbf{r_1} - \mathbf{r_2})/\sigma$, and differential ellipticity $(e_1 - e_2)/2$, where $\sigma_{1,2}$ are the Gaussian beam sizes of the first and second PSBs in a pair, σ is the average beam size, and $\mathbf{r}_{1,2}$ are the centroid locations. Here ellipticity is defined as $e \equiv (\sigma_a - \sigma_b)/(\sigma_a + \sigma_b)$, where $\sigma_{a,b}$ are widths of the major and minor axes, respectively. Beam size and ellipticity differences are sensitive to the second spatial derivative of the temperature field, while pointing offset is also sensitive to the temperature gradient.

For BICEP's focal plane layout and scan strategy, simulations showed that differential beam size, pointing, and ellipticity of 3.6%, 1.9%, and 1.5% rms over the array, respectively, would result in spurious B-mode signal at the r=0.1 level. The differential pointing effect was simulated using the measured magnitude and direction of beam offsets with the expected

amount of false BB power scaling as the square of the magnitude. Differential beam size was simulated by introducing a random distribution of beam size differences in PSB pairs, while keeping the average beam size the same. Similarly, differential ellipticity was simulated by making the beam of every PSB elliptical by a small randomized amount such that the pairs have ellipticity differences of the given rms while keeping the beam sizes the same. The measurements described below indicated that the major axes tend to be more azimuthal with respect to the optical axis than radial, and the major axes of paired PSB beams tend to align within $\sim 15^\circ$ rms of each other. Therefore, the major axes in the simulations were varied around the azimuthal direction by 10° rms to roughly simulate the observed alignment trend within each pair. Analytic calculations show, and these simulations verify, that the expected false BB power scales as the square of differential beam size or ellipticity and as the fourth power of the beam size [47]. I observed no significant systematic shifts in other power spectra, including TE.

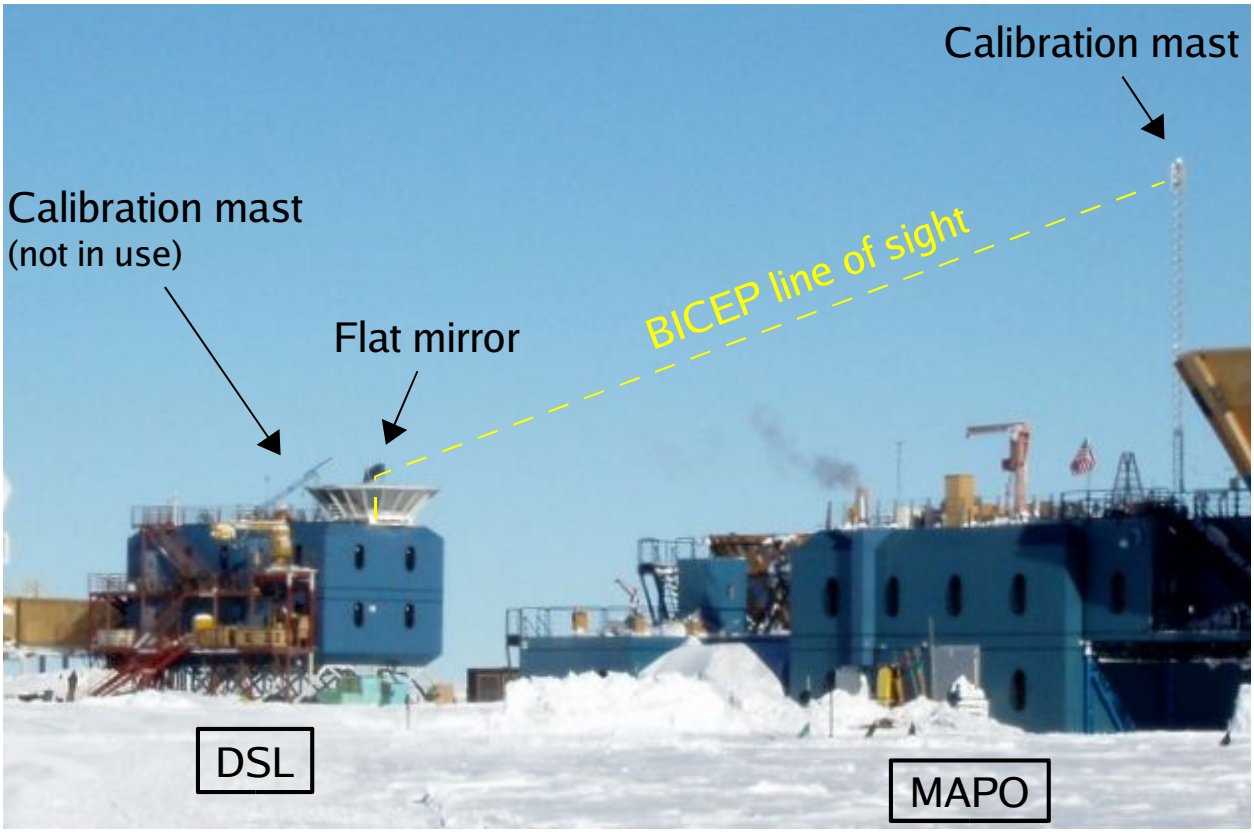

Figure 4.8: Beam mapping setup on site consisted of sources mounted on top of fold-over masts. When using the mast on the MAPO building (200 m from the Dark Sector Laboratory), we mounted a flat mirror to direct the beams over the ground screen.

We mapped the beams by raster scanning a bright source at various boresight rotation angles. The far field of the telescope is about 50 m from the aperture, which permitted measurements in the Caltech high bay prior to telescope deployment as well as with the telescope installed at the South Pole. In the high bay, we used a thermal blackbody source

at a 40-m distance, consisting of a liquid nitrogen temperature load behind chopper blades covered with ambient temperature absorber. At the South Pole, we installed a temporary mast on the rooftop outside of the fixed ground screen, allowing us to position a source at 60° elevation 10 m away. For a truly far-field measurement, we installed an additional mast on the roof of the Martin A. Pomerantz Observatory (MAPO), at a distance of 200 m, and temporarily mounted a flat mirror on top of the telescope to direct the beams down to allow the observation of the distant mast as well as low elevation astronomical sources (Figure 4.8). The sources used included an ambient temperature chopper against the cold sky, a broadband noise source, the Moon, and Jupiter. The broadband noise source is an amplified noise diode that is ideal for probing low-level effects.

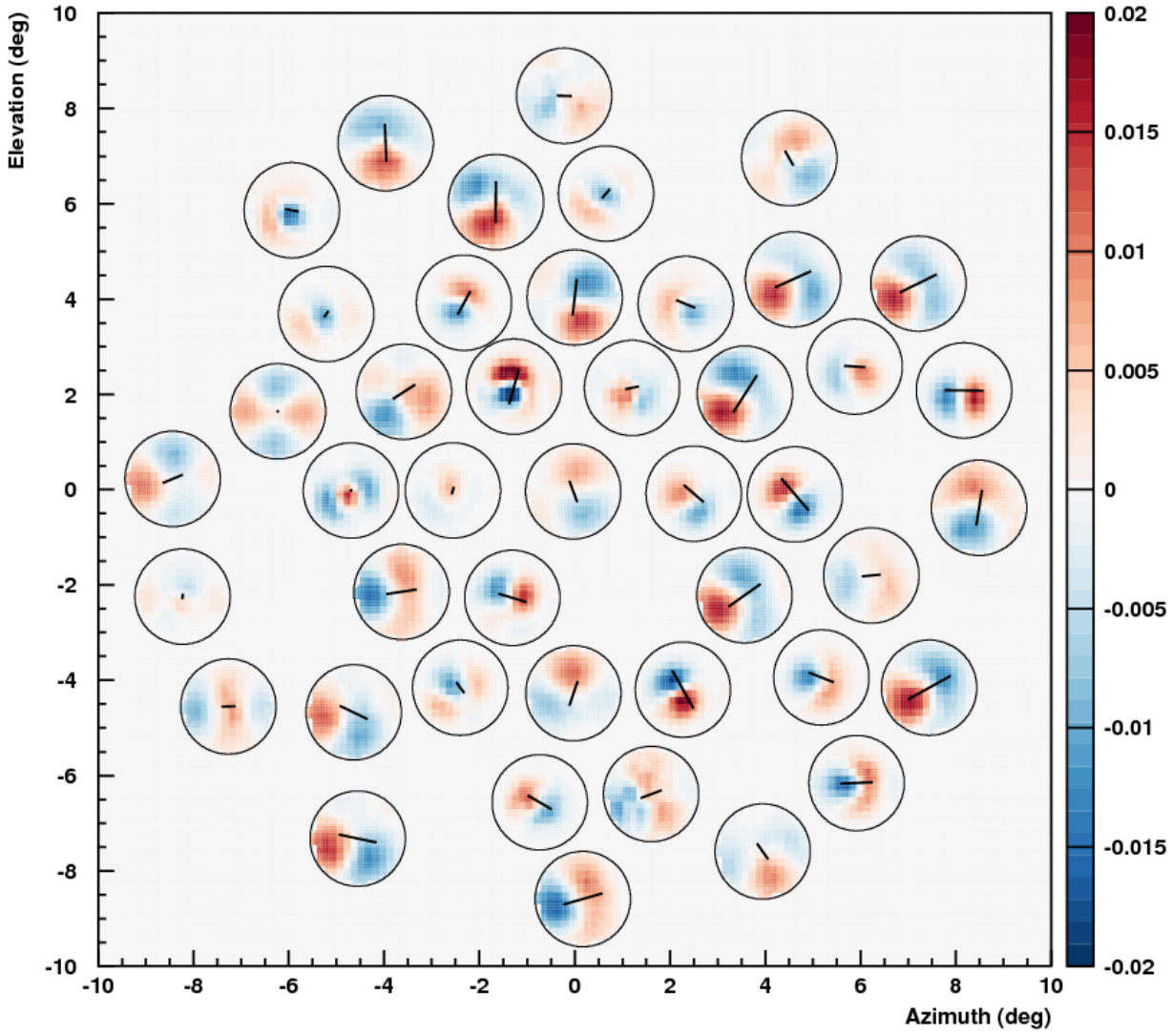

Figure 4.9: Beams for each PSB pair were normalized and differenced to produce this composite differential beam map (in the same orientation as Fig 2.4). The overplotted lines show the fitted pointing offsets magnified by a factor of 100.

The measured beams fit a Gaussian model well, typically resulting in 1% residuals in amplitude. The fitted centroids were repeatable to $\sim$0.02°, although the accuracy of the absolute locations is currently limited by uncertainties in parallax and pointing corrections while using the flat mirror. The average measured FWHMs were 0.93° and 0.60° for 100 and 150 GHz, respectively, about 5% smaller than predicted from physical optics simulations. The beam widths were measured to $\pm$0.5% precision and varied by $\pm$3% across the array. The beams had small ellipticities of $e < 1\%$ at 100 GHz and $e < 1.5\%$ at 150 GHz.

The largest beam mismatch effect was a pointing offset that resulted in dipole patterns in many of the differenced beams (Figure 4.9). The differential pointing offset had a median of 0.004° at both 100 and 150 GHz, and was on average 1.3% of the beam size σ. The offsets were repeatable between measurements with both the broadband noise source and the Moon to within the measurement uncertainty of 0.4% of σ. The origin of the beam offsets is unclear. The direction of the beam separation has some tendency to align with the polarization orientation of one of the PSBs in a given pair. QUaD a two-lens system coupled to a 2.6-m Cassegrain reflector [15], experienced a similar pattern of beam offsets. This suggests asymmetric propagation of linear polarization states through the optical elements. It may be due to birefringence in the lens material.

Simulated observations with the measured pointing offsets indicate a false BB with an amplitude comparable to the r=0.1 spectrum (Figure 4.1b), although well below the noise level of the initial 2-year data analysis. With the magnitude and direction of the pointing offsets measured precisely, the resulting leakage of CMB temperature gradients into polarization can be estimated and accounted for in future analysis. Differential beam size and ellipticity were not measured with significance; the measured upper limits of 0.3% and 0.2% rms, respectively, are negligibly small (Figure 4.1c,d).

4.4 Polarization orientations and efficiencies

To construct accurate polarization maps from PSB timestreams, we must know the polarization orientation angle ψ and cross-polarization response ϵ of each PSB. We must use accurate orientations to prevent rotation of E-mode polarization into false B-mode. Cross-polarization response determines the polarization efficiency $(1-\epsilon)/(1+\epsilon)$, which affects the amplitude scaling of the power spectrum. We developed experimental techniques to measure these quantities by injecting polarized radiation into the telescope at many angles with respect to the detectors. The phase and amplitude of each PSB's response determine ψ and ϵ, respectively. This section discusses the calibration benchmarks for these quantities and describes three measurement techniques and their results. We measured the absolute PSB orientations to within $\pm$0.7°, relative orientation to within $\pm$0.1°, and ϵ to within $\pm$0.01.

PSB orientations can vary from their design angles due to the limited mechanical tolerances in their mounting. A deviation from perfect orthogonality of a pair simply reduces its polarization efficiency; however, an error in the overall orientation of the pair can lead to rotation of E-modes into B-modes. With the expected fractional leakage being $\sin(2\Delta\psi)$, the $\sim$1 μK E-modes at ℓ=100 can rotate into false B-modes at the r=0.1 level of 0.08 μK if the orientation measurement is off by 2.3°. I verified this benchmark and the expected

scaling by simulating systematic orientation offset of all the PSBs. The calibration procedure (§3.3) was designed to determine the polarization orientations to within a degree.

Another factor, though less important, is that the PSBs are not perfectly insensitive to polarization components orthogonal to their orientations, effectively reducing the polarization efficiency to $(1-\epsilon)/(1+\epsilon)$. To achieve 10% accuracy in the amplitudes of the polarization power spectra, which are proportional to $(1-\epsilon)^2/(1+\epsilon)^2$, our goal was to measure cross-polarization responses ϵ to better than ± 0.026.

The dielectric sheet calibrator (§3.3) was used several times throughout each observing year and produced repeatable results for the individual PSB orientations with 0.1° rms (Figure 4.10). The relative orientation uncertainty of $\Delta(\psi_1 - \psi_2) = 0.1°$ results in negligible absolute calibration error. The PSB pairs were orthogonal to within 0.1°, and together were within 1° of the design orientations shown in Figure 2.4. PSB orientation measurements performed before and after the focal plane servicing (November 2006) show a possible discrepancy, exhibiting a systematic rotation averaging 1.0° across the array. We therefore conservatively assign a <0.7° rms uncertainty in the absolute orientation for each year. This absolute orientation angle accuracy is sufficient for measuring $r \ll 0.1$ (Figure 4.1e).

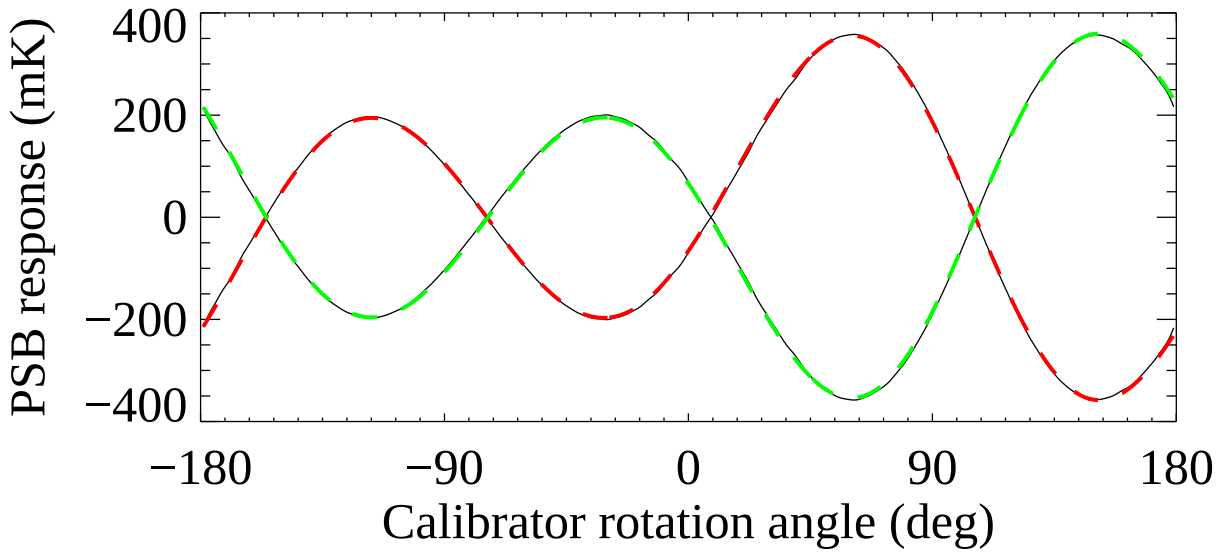

Figure 4.10: Response of each PSB in a pair as a function of the dielectric sheet calibrator orientation (black), plotted over by the fits (in red and green dashes) with the polarization orientations and responsivities as free parameters.

The cross-polarization responses ϵ were measured using two methods that also independently verified the absolute orientation measurement. One method used a rotatable wire grid in front of the telescope window with a chopper modulating the polarized load through a small aperture between the ambient absorber and the cold sky (Figure 4.11). Fitting a sinusoid to the individual PSB response as a function of the wire grid angle gives the polarization efficiency and orientation. The measurements for all three years gave cross-polarization response values with a distribution $\epsilon = 0.045 \pm 0.02$. We omitted from analysis one 150 GHz

bolometer for having an ϵ>0.12 and replaced it at the end of the first year.

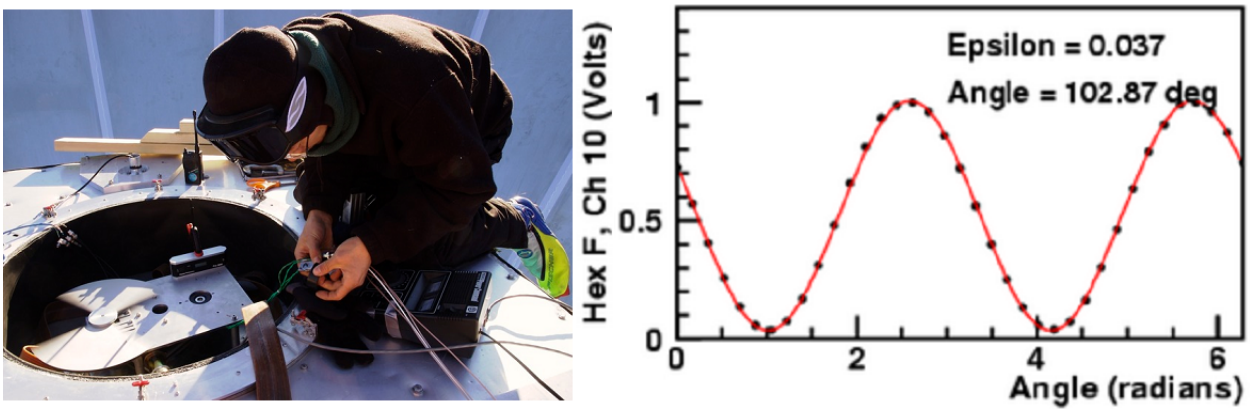

Figure 4.11: Setup above the cryostat window for measuring cross-polarization responses and PSB orientations. We covered the window with a metal plate with a 2-cm Eccosorb aperture, and a 10-cm diameter wire grid was on a rotation stage under the circular aperture of the rectangular plate. The chopper modulated the load between the ambient temperature and the cold sky.

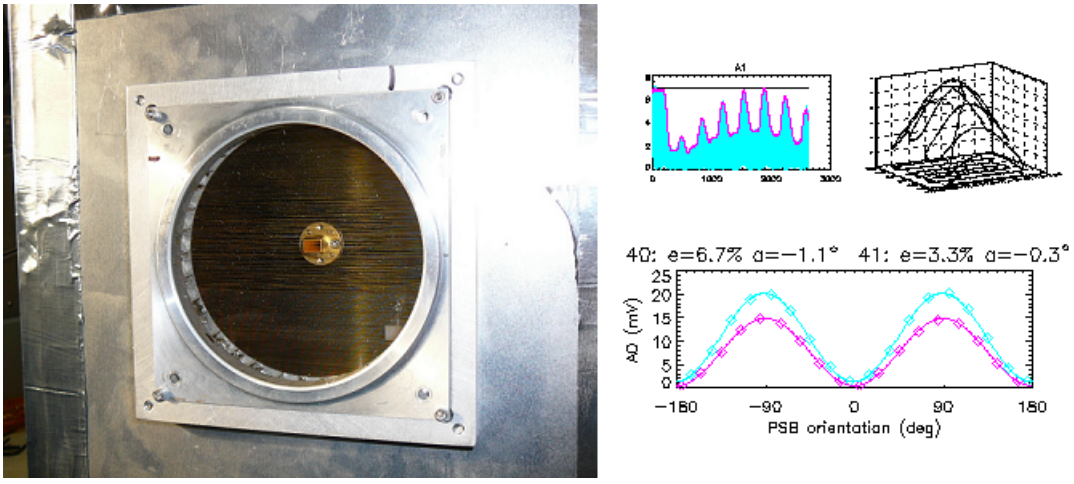

Figure 4.12: Another calibration source, used on top of a mast, for measuring cross-polarization responses and PSB orientations. A broadband noise source at 100 or 150 GHz outputs power through the rectangular feedhorn oriented for either vertical or horizontal polarization 2 cm behind a precisely aligned 10-cm diameter wire grid to minimize cross-polarized signal.

The other method used a chopped broadband noise source with a rectangular horn behind a wire grid and mounted on the mast 200 m away (Figure 4.12). With a low-loading reflector in front of the mast, BICEP observed this source using the far-field flat mirror, with the bolometer bias and the temperature control loop adjusted for the higher atmospheric loading. The source, chopped at 4 Hz, was raster scanned by each of our beams with 18 different

detector orientations with respect to the wire grid. We repeated this for 100 and 150 GHz sources oriented in vertical and horizontal polarizations.

The timestreams were deconvolved and 2–10 Hz band-pass filtered. For each raster scan at a given telescope orientation, I demodulated the timestreams and fitted a 2-dimensional Gaussian profile. Then for each detector, I plotted the signal amplitude as a function of the nominal detector polarization orientation projected on the sky and fitted a sine curve to find the cross-polarization response ($\epsilon = min/max$) and angle. The measurement had a median of ϵ=0.038, slightly lower than with the aperture measurement. Based on the scatter against the results from the first method, we assign an uncertainty of $\Delta\epsilon = 0.01$, which translates to 4% uncertainty in the polarization power spectrum amplitudes.

4.5 Telescope and detector pointing

As mentioned in §3.5, pointing errors greater than 1% of the beam size σ could contaminate the B-mode spectrum at the $r{\sim}10^{-4}$ level [17]. Since the amount of spurious BB power scales as the square of the pointing error, the r=0.1 benchmark would correspond to 0.3σ, or $5'$ for BICEP. I verified that this benchmark was conservative by simulating a $5'$ rms shift in boresight pointing every 10 elevation steps in one of our simulation pipelines and finding negligible spurious signal compared to the r=0.1 BB signal. We used the optical star pointing camera to measure the telescope boresight pointing model with uncertainties over an order of magnitude smaller than required to achieve our benchmark.

We performed optical pointing calibration every two days during the refrigerator cycles, weather permitting, as well as before and after each mount re-leveling. In each run, we pointed the telescope at 24 stars at boresight rotation angles of $-45°$, $45°$, and $135°$, and recorded the azimuth and elevation offsets required to center each star. We fit the pointing data to an 8-parameter model (it was not necessary to fit for telescope flexure), resulting in typical residuals of $0.2'$ rms. We checked the pointing model by cross-correlating the CMB temperature anisotropy patterns between the pointing-corrected daily maps and the cumulative map; we detected no systematic offsets or drifts.

In parallel with the optical pointing calibration, we monitored the tilt of the telescope mount every two days using two orthogonal tilt meters mounted on the azimuth stage. We observed tilt changes of up to $0.5'$ per month, possibly due to the building settling on the snow, and typically re-leveled the mount before the tilt exceeded $1'$.

Finally, to co-add maps made with different PSB pairs, we must determine the actual locations of all the beams relative to the boresight. We accomplished this by first making a full season co-added map of the CMB using the design locations and then cross-correlating the temperature anisotropy pattern with single detector maps for each of the 4 boresight rotation angles to adjust the individual beam coordinates. We then used these adjusted coordinates with respect to the boresight to iterate this process until every individual pair map became consistent with the full co-added map. This derivation of the absolute beam locations resulted in an uncertainty of $2'$ rms, based on the agreement between the first and second years. For BICEP, using the CMB temperature fluctuations proved more effective than attempting a similar procedure with Eta Carinae, the brightest compact source accessible.

4.6 Sidelobe rejection

Sidelobes of the telescope beams can pick up emission from the bright Galactic plane and structures on the ground, potentially resulting in contamination of the polarization maps. We designed the ground shields to reject the ground radiation to a level where the contamination is below our target B-mode polarization sensitivity. This section describes the sidelobe measurement and the possible polarization contamination due to the sidelobes. BICEP's measured sidelobes are sufficiently low for probing B-mode polarization to the level of r=0.01.

We measured the sidelobe response of the telescope, including the forebaffle, using a chopped broadband noise source on the mast 10 m from the telescope aperture (Figure 4.13). The telescope was stepped in elevation up to 70° away from the source in 0.5° increments, making one revolution about the boresight and back at each step to measure a radial average of the beam. We performed this measurement with both vertically and horizontally polarized sources and with several source attenuations down to below −50 dB to probe the far sidelobes with sufficient S/N while also measuring the main beam without saturating the detector. Each measurement run took 6.5 hours.

Figure 4.13: Sidelobe measurement using a modulated broadband noise source on a mast.

I demodulated the timestreams by removing a central moving average smoothed over 1 second, and then multiplying by a normalized chopper reference. Then I constructed

sidelobe response maps by binning into 0.8° square grids across an 80° radius centered on the source, correcting for the parallax (Figure 4.14). Sidelobes and their polarization appeared very similar among all detector pairs of a given frequency band. Incident waves polarized parallel to the absorbing forebaffle lip surface seem to diffract more strongly than those polarized perpendicular to the lip. This seems to cause partial polarization in the sidelobe response beyond ∼16° from boresight where the forebaffle lip cuts off the beam. This difference appears to be mainly responsible for the polarized response in the sidelobes. Sidelobe response maps constructed from the gain-adjusted pair differences show that the sidelobes are up to 50% polarized.

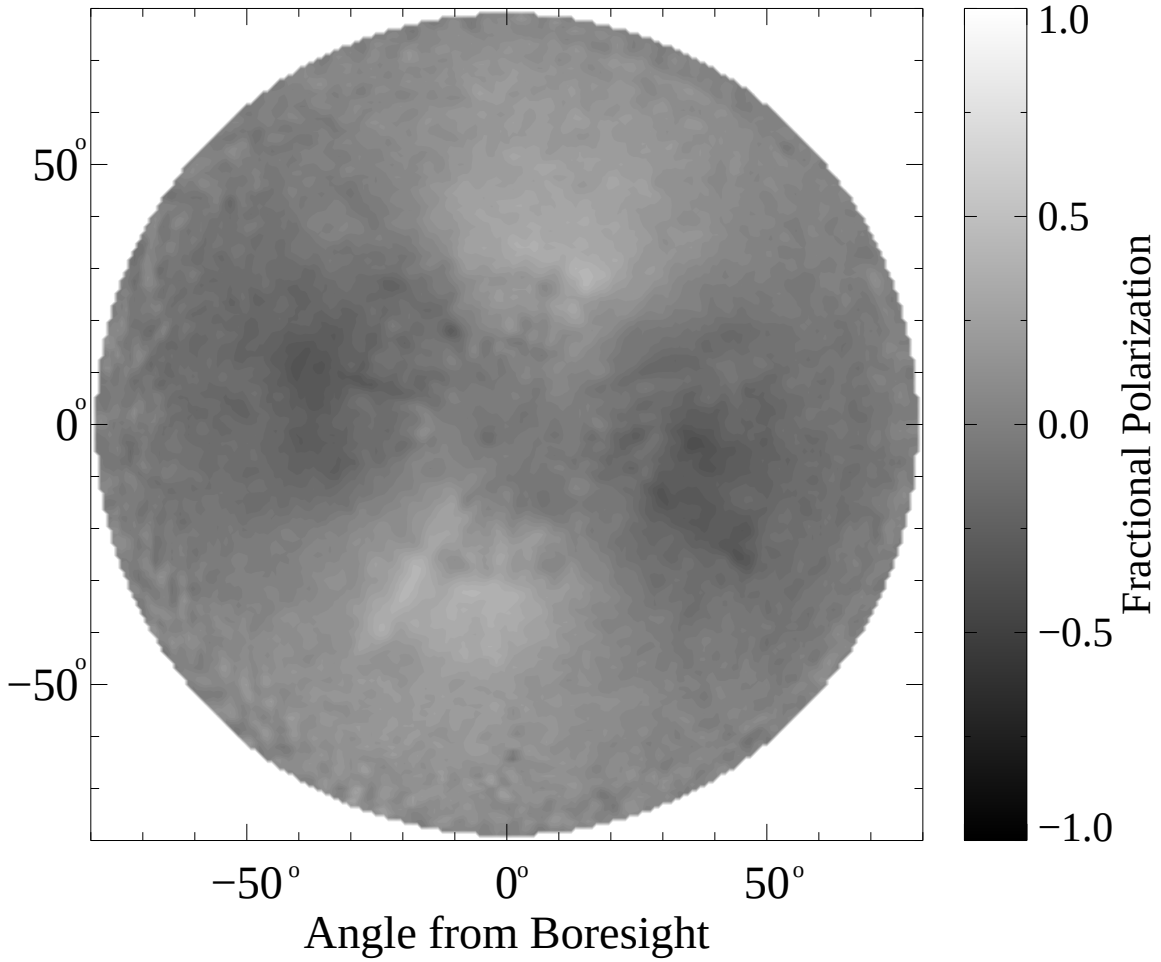

Figure 4.14: Map of fractional polarization for a 100 GHz feed ("C1") up to 80° from the beam center, showing the gain-adjusted pair difference divided by the pair sum. Beyond ∼15° from the boresight where the forebaffle cuts off the beam, the sidelobes are generally up to 50% polarized, but with smooth quadrupole pattern aligned with the polarization sensitivity.

The individual sidelobe maps were averaged azimuthally over boresight rotation angle to obtain a radial profile (Figure 4.15). I corrected for the relative detector responsivities

using V/K_{CMB} calibration values from the dielectric sheet calibrator. Then I determined the gain normalization factor for each frequency band by matching the main beam profile with that of a separate main beam measurement. To express the gain in dBi, a unit-normalized gain was multiplied by $4\pi\Omega$, where $\Omega = 2\pi\sigma^2$ is the beam solid angle (Table 4.3). Results from high and low source powers agreed well (except for detector saturation around the main beam and noise beyond certain angles for low powers).

Table 4.3: Beam gain normalization

Band	Beam size σ	Beam solid angle ($\Omega = 2\pi\sigma^2$)	Forward gain ($4\pi\Omega$)
96 GHz	0.395°	2.986×10^{-4} sr	42081 (46.2 dBi)
150 GHz	0.255°	1.243×10^{-4} sr	101132 (50.0 dBi)

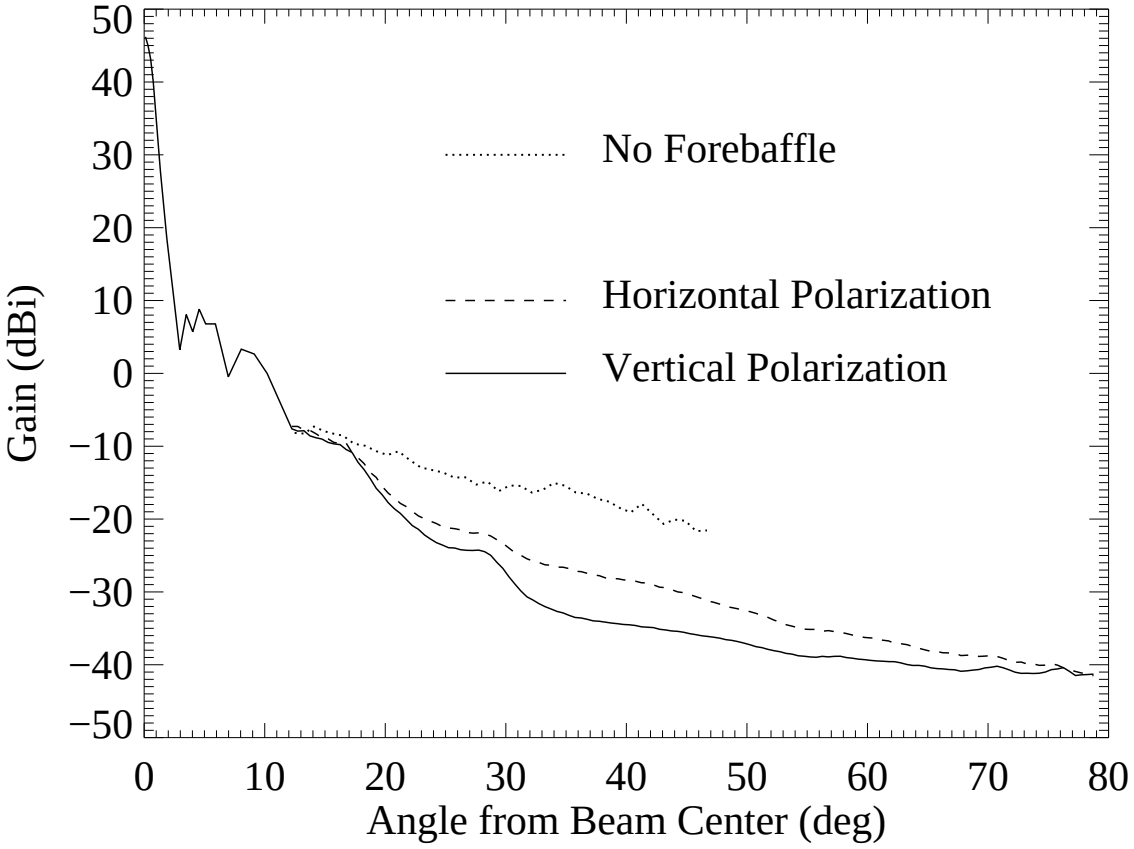

Figure 4.15: Azimuthally-averaged sidelobe response for the 100 GHz central feed. A forebaffle with an absorptive lining cuts in at 15.5° and provides up to an additional ∼15 dB attenuation. When the telescope is at its lowest elevation of 50°, the lip of the outer ground screen is ∼30° from the beam center of the central feed. Sidelobe polarization seems to be mostly due to the difference in sidelobe response between horizontal and vertical polarizations, and can be modeled roughly with a Gaussian profile.

To quantify what fraction of the total power in the beam remains outside of a given angle from the beam center, I tried integrating the net beam profile for horizontal and vertical polarizations (Figure 4.16). The beam leaves $< 0.1\%$ of the power beyond 15° and 20° of the beam center at 100 and 150 GHz, respectively.

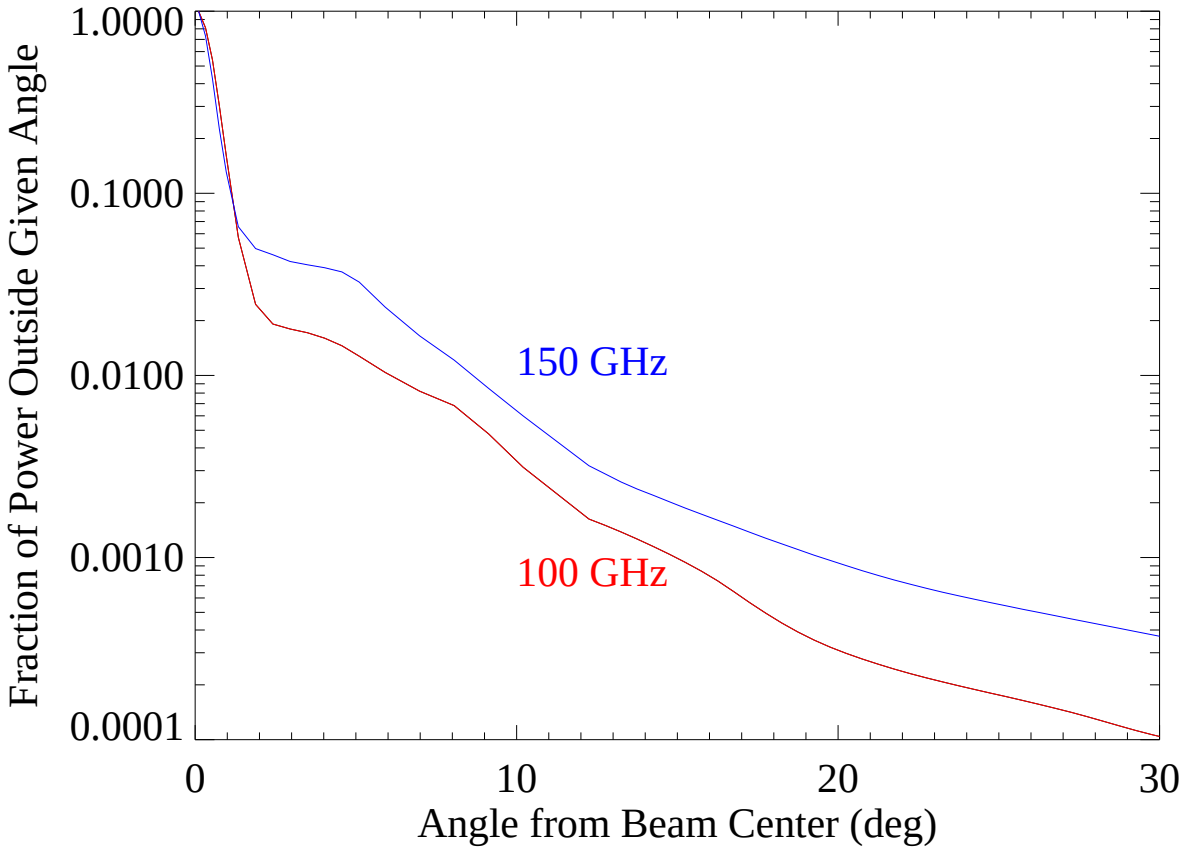

Figure 4.16: Fraction of total power, after integrating the sum of the beam profiles for the horizontal and vertical polarizations in Figure 4.15 over the solid angle from 80° to the given angle.

Polarized sidelobes can result in spurious signals by coupling to emission from the Galaxy and even the outer ground screen itself. To evaluate the far sidelobe rejection performance, we convolved the measured level of polarized response with a model map of a potential contaminant (Figure 4.17), and computed an angular power spectrum in the BICEP field to compare with the r=0.1 BB spectrum. For the Galactic model, we used the dust emission predicted by FDS [10]. The resulting B-mode contamination was at least 400 times below the r=0.1 level, meaning the measured sidelobes are at least 13 dB below the benchmark (Figure 4.18). We repeated the same exercise for a conservative model of snow accumulation on the ground screen, alternating the 20 screen panels between 0 K and 5 K assuming snow with $\sim$2% emissivity. The contamination was even smaller, with the achieved rejection level at least 23 dB better than the benchmark.

We have also probed potential ground contamination in our data through a jackknife test comparing maps made in different azimuth ranges, and have seen no evidence of ground signal. As mentioned in §2.5, the scan range is fixed with respect to ground during each one-hour scan set so that subtracting a scan-synchronous template each hour removes any ground-fixed signal.

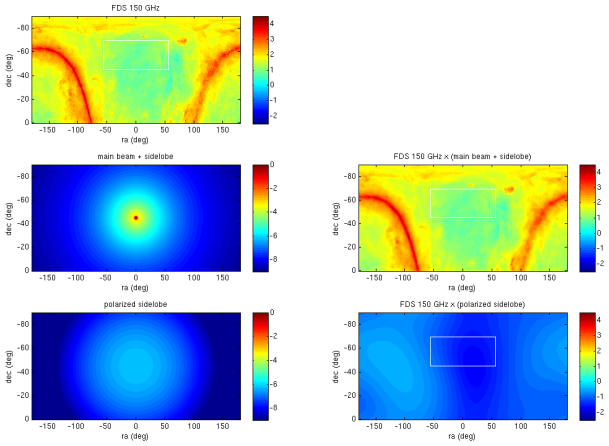

Figure 4.17: Convolution of sidelobes on Galactic emissions (using John Kovac's codes). *Upper left*: FDS 150 GHz template (the scale is $\log_{10}$ of temperature in μK), with the BICEP field shown in rectangle. *Left*: 150 GHz main beam + sidelobe (middle), and the polarized sidelobe only (bottom). *Right*: FDS template convolved with each of these. Angular power spectra were computed in the BICEP field on these maps.

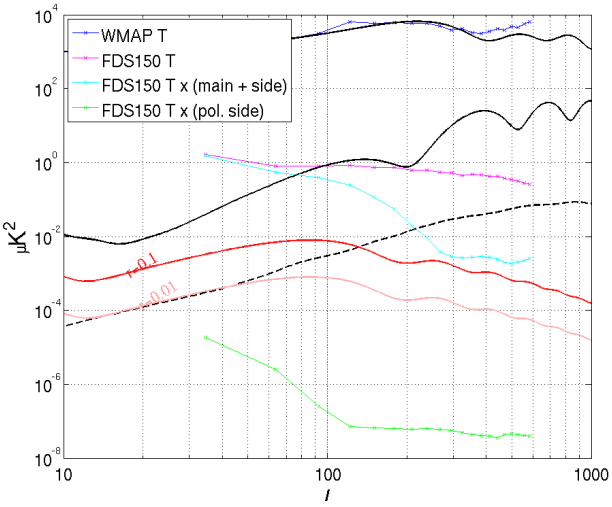

Figure 4.18: Power spectra of sidelobe response to Galactic emissions. Plotted are power from the dust T (magenta), dust T convolved with 150 GHz beam (cyan), and dust T convolved with polarized sidelobes only (green). The power at ℓ=40 is dominated by leakage in the power spectrum estimation technique from much larger angular scales, so should be regarded as an upper limit, but I based our conservative benchmark on this band power. 13 dB higher sidelobes could produce polarized contamination comparable to r=0.1.

4.7 Thermal stability

The thermal and optical responsivities of PSBs in each pair do not necessarily match, so the temperatures of the detector focal plane and the emissive optics must be sufficiently stable to prevent the introduction of scan-synchronous thermal signals. We have measured the thermal responsivity of every bolometer and compared the mismatches with the focal plane temperature stability, which we control with a feedback loop. The thermal stability of both the focal plane and the optics was adequate compared to the r=0.1 benchmark.

We measured the bolometers' responsivities to the bath temperature by correlating the detector timestreams with the 10 mK drop when the temperature control heater was turned off at the end of each refrigerator cycle. The median thermal responsivity, after converting voltages into CMB temperature units, was 0.8 $\mu K_{CMB}/nK_{FP}$, and the median mismatch within PSB pairs was 0.08 $\mu K_{CMB}/nK_{FP}$. Because the pair differential responsivities have a random distribution in the array, the effects of the mismatch would average out when the maps are co-added. The averaged mismatch over the array, considering both the magnitudes and signs of the thermal response, was 0.025 and 0.001 $\mu K_{CMB}/nK_{FP}$ at 100 and 150 GHz, respectively. To meet the r=0.1 target of 0.08 μK_{CMB} at $\ell \sim 100$ then, we must control thermal instabilities in the focal plane to better than 3 nK rms.

To mitigate the thermal fluctuation effects, we stabilized the focal plane temperature at 250 mK using a 100 kΩ resistor as a control heater (nominally depositing $\sim$0.1 μW) in a PID feedback loop with a sensitive NTD germanium thermistor. We set the PID parameters such that no active regulation takes place within the observational signal band of 0.1–1 Hz; we controlled only long time-scale drifts so that the PSB relative gains remain unaffected. The focal plane was equipped with 6 pairs of monitor thermistors spaced evenly around its perimeter. During the first year, the thermal control scheme used a thermistor closest to the thermal strap connected to the refrigerator. To improve the recovery time from major thermal disturbances and other transient events, we installed additional control thermistors near the control heater on the thermal strap at the end of the first year. Vespel[1] supports improved the thermal strap rigidity to reduce susceptibility to vibrationally induced heating. Along with an increased response speed of the control loop, the temperature stability measured by the focal plane thermistors improved from the first year to the second.

To estimate the focal plane temperature stability, we co-added scanset-template subtracted thermistor phase maps for each cryostat orientation and observing year (Figure 4.19), and then computed the angular power spectra. Scan-synchronous template subtraction significantly reduced large-scale temperature fluctuations. Some strong contaminations were still present along the azimuth directions due to isolated cases of thermal instabilities. The measured nominal level of thermal fluctuations at the focal plane was 1 nK rms in the frequency range corresponding to ℓ=100 (Figure 4.20).

Finally, since emission from BICEP's optics is expected to be largely unpolarized, the main concern with optics temperature drifts was in mis-calibration of PSB pair optical relative gains, which have an upper limit of 1.1% rms as described in §4.2.2. To limit the pair-difference response to less than 0.08 μK_{CMB}, the scan-synchronous optical loading fluctuations must be under $\sim$8 μK_{CMB}, requiring the optics temperature to be stable to at least 4 μK_{RJ} rms (for the 150 GHz band). Scan-synchronous fluctuations averaged over all the individual bolometers for a two month period showed 0.7 μK_{RJ} rms variations in the 0.1–1 Hz frequency range.

[1] `http://www2.dupont.com/Vespel/en\_US`

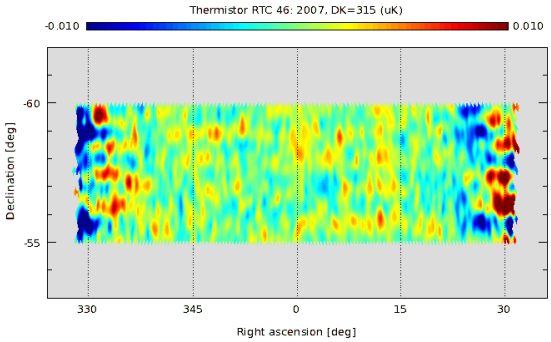

Figure 4.19: Focal plane thermistor map for cryostat orientation of 315° in 2007, excluding observing periods with frequent thermal instabilities.

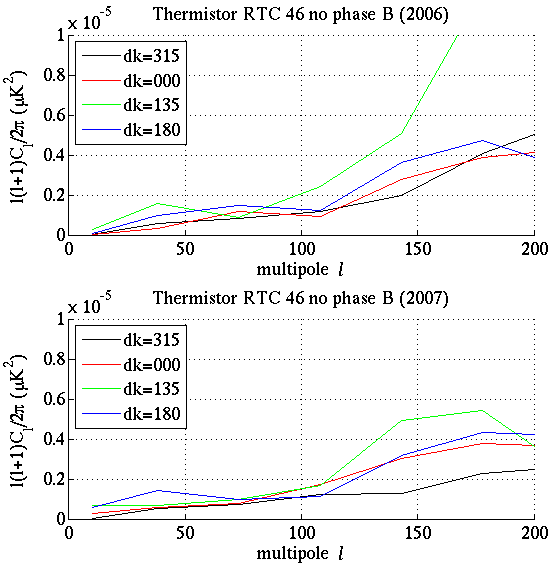

Figure 4.20: Power spectra of focal plane temperature fluctuations, for each cryostat orientation and observing year.

Chapter 5

Data analysis and results

5.1 Collected data, cuts, and observing efficiency

Excluding any incomplete 9-hour observing blocks, BICEP acquired 180 days of CMB observations during 2006, in which we devoted a significant fraction of the observing season to calibration measurements. During 2007 and 2008, we observed continuously except during the ∼100 days that the station was open for the summer (Table 5.1). Altogether, we collected CMB data during 85% of the winter days. Although there is no evidence for Sun contamination during the summer, we currently restrict our CMB analysis to data taken during February–November.

For the initial analysis, we tried to be conservative, using ∼75% of the detectors and 75% of the scanning time. We excluded 5 PSB pairs for unusual looking temporal transfer functions, even though we measured them precisely. Future analyses may use data from these pairs, which would add 10% more data. We also cut scan turnarounds aggressively to be cautious about focal plane thermal disturbances.

The initial analysis has excluded the first 2.5 months of 2006 data because we were investigating a different scan strategy at that time and also detected a small level of radio frequency interference. We successfully eliminated the interference by improving the electromagnetic shield surrounding the room temperature receiver electronics.

As a coarse weather cut, we have excluded 9-hour blocks if the relative gains derived from elevation nods varied by >20% rms, averaged over the detectors. This criterion cut clear outliers in the distribution of atmospheric instability. After these cuts, 117 days in 2006 and 226 days in 2007 remained for our initial baseline CMB analysis (Table 5.1).

Table 5.1: CMB observation summary for the initial analysis

	PSB pairs: used (total)		Observing days:	Integration
	100 GHz	150 GHz	used (total)	time [a]
2006	19 (25)	14 (24)	117 (180) days	4.5×10^6 sec
2007	22 (25)	15 (22)	226 (245) days	8.8×10^6 sec
2008	22 (25)	15 (22)	198 (239) days	7.7×10^6 sec

[a] Based on 18 hours per day of CMB observation at 60% net observing efficiency.

Furthermore, we omitted 3% of PSB pair timestreams due to cosmic ray hits, glitches, or >3% mismatch in the relative gains measured at the beginning and end of each 1-hour

scan set. Accounting for the 75% scan efficiency (Figure 2.9) and the scheduled calibration routines, the net CMB observing duty cycle was 60% during the CMB observing blocks and 45% overall during each 2-day cycle.

After all the data cuts, we acquired 10000 hours of integration time on the main CMB field, 1500 hours on the weak Galactic field, and 1000 hours on the brighter Galactic field (Figure 5.1).

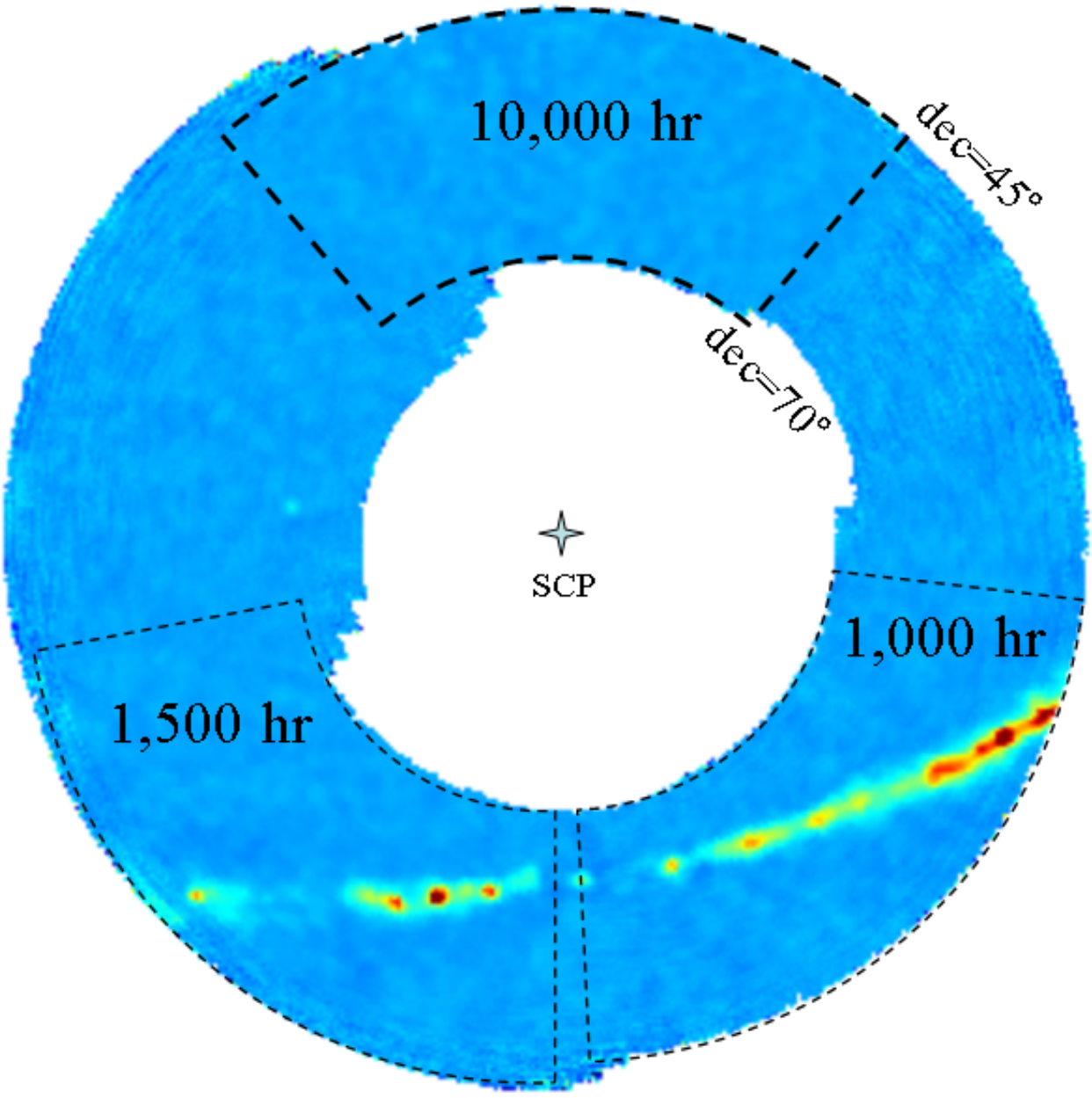

Figure 5.1: BICEP map of the entire mapped field, with integration time on each field after all data cuts. We also spent small amounts of time on regions between the main fields, and have performed 360° azimuth scans to cover the entire annulus. (Map thanks to Cynthia.)

5.2 Data analysis overview

Data analysis (summarized in Figure 5.2) involves raw timestream cleaning, map making (Section 5.3), power spectrum estimation, noise simulations for noise bias removal (Section 5.4), signal simulations for filtering effect correction, signal+noise simulations for uncertainty estimation, and finally the derivation of constraints on r (Section 5.5). The BICEP team has developed two data analysis pipelines that differ starting from the map making stage. The code in each pipeline is completely independent of the other; the only shared data products are the initial set of downsampled, cleaned detector timestreams, telescope pointing, and calibration data. The mapmaking algorithms used by the two pipelines are similar, although one bins in the `Healpix` [13] pixelization scheme, while the other produces maps in rectangular coordinates. For power spectrum estimation, the first performs a curved-sky analysis using the `Spice` [6] package to estimate the power spectra, and the second is a flat-sky pseudo-C_ℓ estimator adapted from QUAD [43]. Both pipelines have produced similar results.

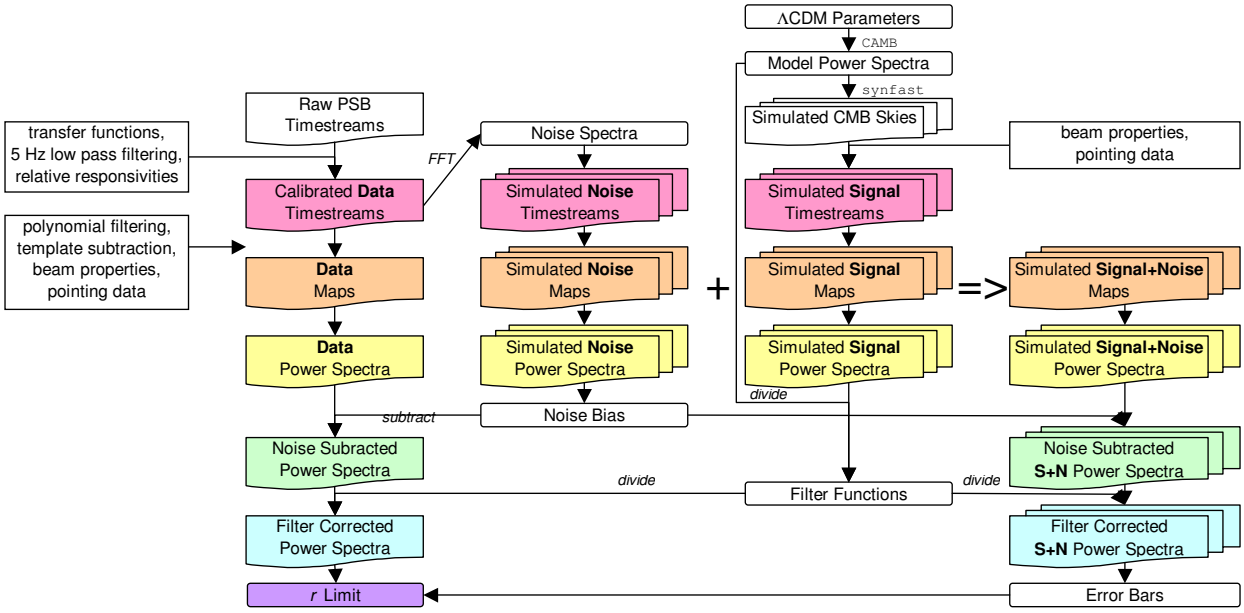

Figure 5.2: Data analysis flow chart.

5.3 CMB temperature and polarization maps

In preparation for making maps, we processed the raw 50 Hz PSB timestreams by deconvolving the temporal transfer functions and low-pass filtering them at 5 Hz to down-sample to 10 Hz. Then we formed gain-adjusted sum and difference timestreams for each PSB pair. To reduce atmospheric $1/f$ noise, we subtracted a 3rd-order polynomial from the sum and difference timestreams for each half-scan in azimuth. We removed azimuth-fixed and scan-synchronous contamination by subtracting a template formed by binning the polynomial-

filtered detector timestreams in azimuth over each set of fixed-elevation scans. There were slight differences in the scan-synchronous signal between left- and right-going scans, so we generated separate templates for each case. The difference in the polarization maps before and after this process – typically 0.1–0.4 μK at the largest scales – indicated that the scan-synchronous contamination was very small. We then binned the bolometer timestreams into temperature and polarization maps.

The temperature T at each map pixel came from simply binning the filtered sum timestreams into map pixels, while Stokes Q and U came from linear combinations of the difference timestreams. We chose the pair sum and difference weights to be proportional to the inverse variance of the filtered timestreams, evaluated from power spectral densities averaged over each 1-hour scan set. More precisely, for each PSB pair, we computed the weight for a scan set from the inverse of the average value of the auto-correlation over 0.5–1 Hz.

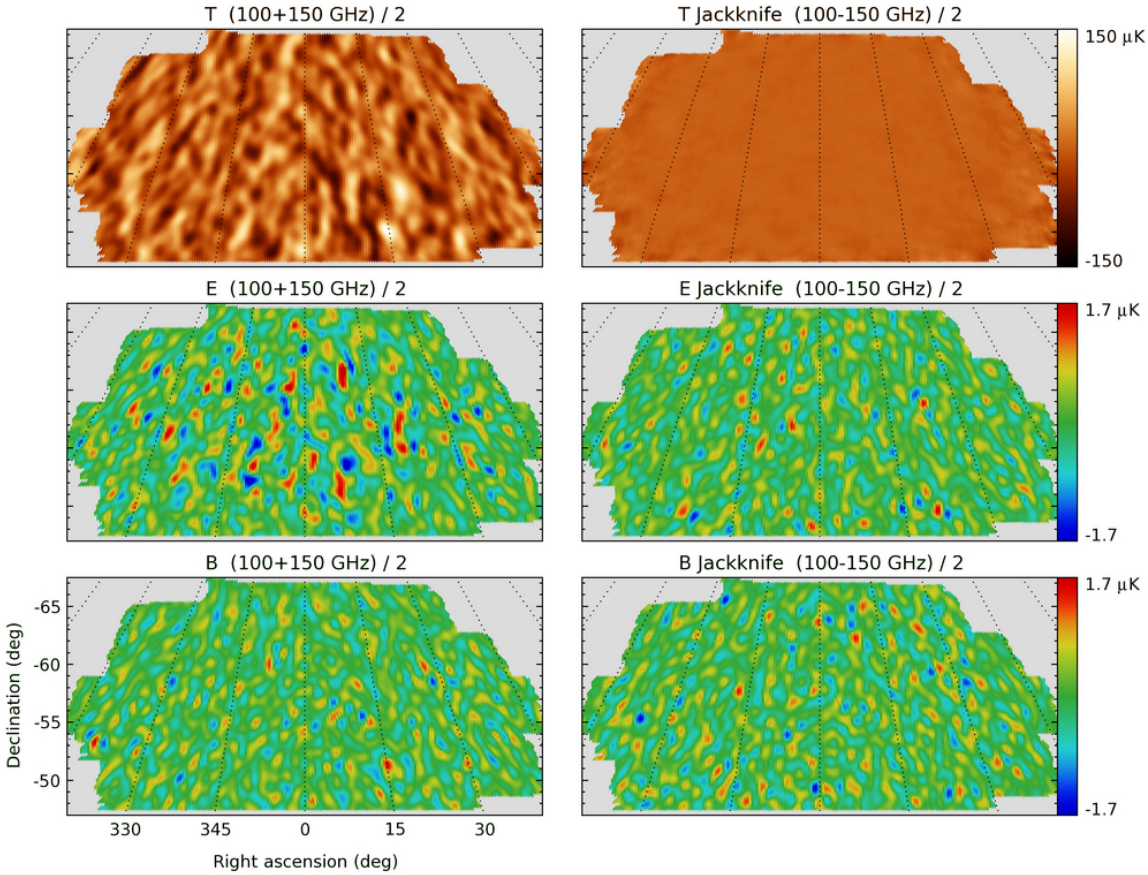

Figure 5.3: Maps from the first 2 years of data, including frequency jackknife differences (right column) [5]. We have removed a 3rd-order polynomial from each half-scan, and have smoothed the maps to 1° resolution. *Top row:* CMB temperature anisotropy. The faint striping in the jackknife map is due to residual atmospheric noise, removed by PSB differencing. *Bottom rows:* Stokes Q and U maps are combined to produce Wiener-filtered E- and B-mode polarization maps. The E signal map shows degree-scale anisotropy at the expected level, while the other three maps are consistent with noise.

Figure 5.3 shows temperature and polarization maps from BICEP's first two years of operation, as well as jackknife differences formed by subtracting maps made at the two frequencies. The CMB temperature anisotropy has been measured with high S/N, as demonstrated by the absence of structure in the temperature jackknife map. The faint striping caused by residual atmospheric noise is removed by PSB differencing.

The E- and B-mode maps were derived from apodized Stokes Q/U maps and are Wiener-filtered according to the expected E-mode signal divided by the beam function. The E-mode map displays the degree-scale structure, while the E and B jackknife maps and B signal maps are consistent with noise. The frequency jackknife maps show no evidence of foreground contamination.

After 3700 hours of total integration time during the first 2 years, the noise per 1 deg^2 pixel in the Q and U jackknife maps was 0.78 μK rms for 100 GHz and 0.62 μK rms for 150 GHz, consistent with expectations. The map noise levels translate to a preliminary estimate of noise equivalent temperature (NET) per detector of 560 $\mu\mathrm{K}\sqrt{s}$ at 100 GHz and 430 $\mu\mathrm{K}\sqrt{s}$ at 150 GHz. This was 17% higher than anticipated at 100 GHz, but on target at 150 GHz.

5.4 Noise properties and modeling

The first step in angular power spectrum estimation was calculating and subtracting the noise bias $\langle \hat{N}_\ell \rangle$. Precise characterization of noise in the BICEP data is crucial for accurately extracting the underlying CMB polarization power spectrum. Noise dominates the detector timestreams and we must model and simulate it to subtract the noise bias from the resulting power spectra. Precise subtraction is critical because any misestimation results in a systematic error in the power spectrum amplitude. Simulating the effect of a noise misestimate on the final BB spectrum from the 2-year BICEP data, we find that a $\pm 3\%$ overall error in the noise power estimate would result in a bias of $r = \pm 0.1$. This translates to a benchmark of 1.5% accuracy in CMB temperature units for the pair difference noise simulation. Also, the simulation of noise, along with that of signal, determines the error bars of the CMB power spectra and the constraints on the B-mode polarization amplitude.

To derive the noise bias, we used the actual data to characterize the frequency spectra of noise, simulated signal-free noise-only timestreams, and processed them with the same pipeline as the actual data to compute the noise power spectra. The resulting simulated spectra were averaged over many realizations to specify the noise bias. This section describes characterization of the noise properties, simulation of noise-only timestreams, and the resulting estimates of the noise bias in the final angular power spectrum. The noise level was consistent with expectations and we found no significant cross-correlations in noise among pair differences, and the simulated noise has been checked for consistency with the actual noise level in the data.

5.4.1 Properties of noise: spectra and covariance

To simulate noise-only timestreams with the same statistical properties as the actual data, we first modeled the noise properties. Because noise dominates BICEP's raw timestreams, we modeled it by simply computing the auto and cross spectral power distributions for PSB sums and differences. The S/N in the timestreams was $\leq$0.2% for the pair differences and 1–10% for the pair sums in the 0.1–1 Hz range corresponding to ℓ=30–300. The significant CMB signal in the pair-sum timestreams is expected to introduce some error, but we permitted this in the initial analysis because the noise bias uncertainty is expected to be much smaller than the cosmic variance in the temperature power spectrum. The initial noise model accounted for correlations among all the detectors in the focal plane, but did not attempt to include correlations between half-scans or between different time scales within each half-scan.

I modeled and simulated PSB pair sums and differences after the removal of a 3rd-order polynomial from the 20 s of each half-scan that we used in CMB map making. For each pair sum or difference consisting of 200 points at a 10 Hz sampling rate, I took the Fourier transform and multiplied by its complex conjugate for an auto power spectrum in frequency space. I multiplied the Fourier transforms of different pair sums or differences during each half-scan, $\tilde{d}_A\tilde{d}_B^*(2/\Delta\nu)$, to obtain complex cross spectra in units of V^2/Hz, where $\Delta\nu$ = 0.05 Hz is the frequency resolution.

For each one-hour constant-elevation scan set, I averaged the complex spectra of 100 half-scans. By comparing the average spectra over the first and the second halves (50 half-scans each) of the scan set, I checked that the noise properties were approximately stationary during a one-hour period compared to the uncertainties in the averaged spectra. Similarly, I compared the average spectra for right-going and left-going scans during a scan set to verify that there was no statistical difference. To compute the noise model, I then binned the spectra into 12 logarithmically spaced frequency bands spanning 0.05–5 Hz. The average auto spectra over all PSB pairs in each frequency band are plotted in Figure 5.4, with the detector voltages converted to CMB temperature differences. The NETs were consistent with expectations, and were comparable to the best achieved in other ground-based experiments like ACBAR [45] and QUAD [15]. Before differencing, the timestreams showed significant atmospheric noise below 1 Hz. Pair differencing rejected this effectively, although there was a hint of excess low frequency noise, especially at 150 GHz. All auto and cross spectra for pair sums and pair differences were combined to form a complex noise covariance matrix $\tilde{\mathbf{N}}(f)$ at each of the 12 frequency bands, some of which are shown in Figure 5.5.

For the purpose of generating the noise model, we gap-filled the pair sum and difference timestreams for cosmic ray hits and electronic glitches. In making the actual CMB maps, however, we simply excluded any detector half-scan with a glitch. Because we constructed the noise covariance matrices by averaging auto and cross spectra over multiple half-scans, excluding a half-scan for a single PSB pair sometimes caused the matrices to become non-positive-definite, preventing the Cholesky decomposition necessary for the timestream simulation process described in the next section. Excluding a half-scan for all detectors if any of them contains a glitch resulted in up to 70% data loss for the noise model calculation. We therefore filled gaps when possible, and rejected a half-scan for all detectors if more than four PSB pairs displayed a simultaneous glitch.

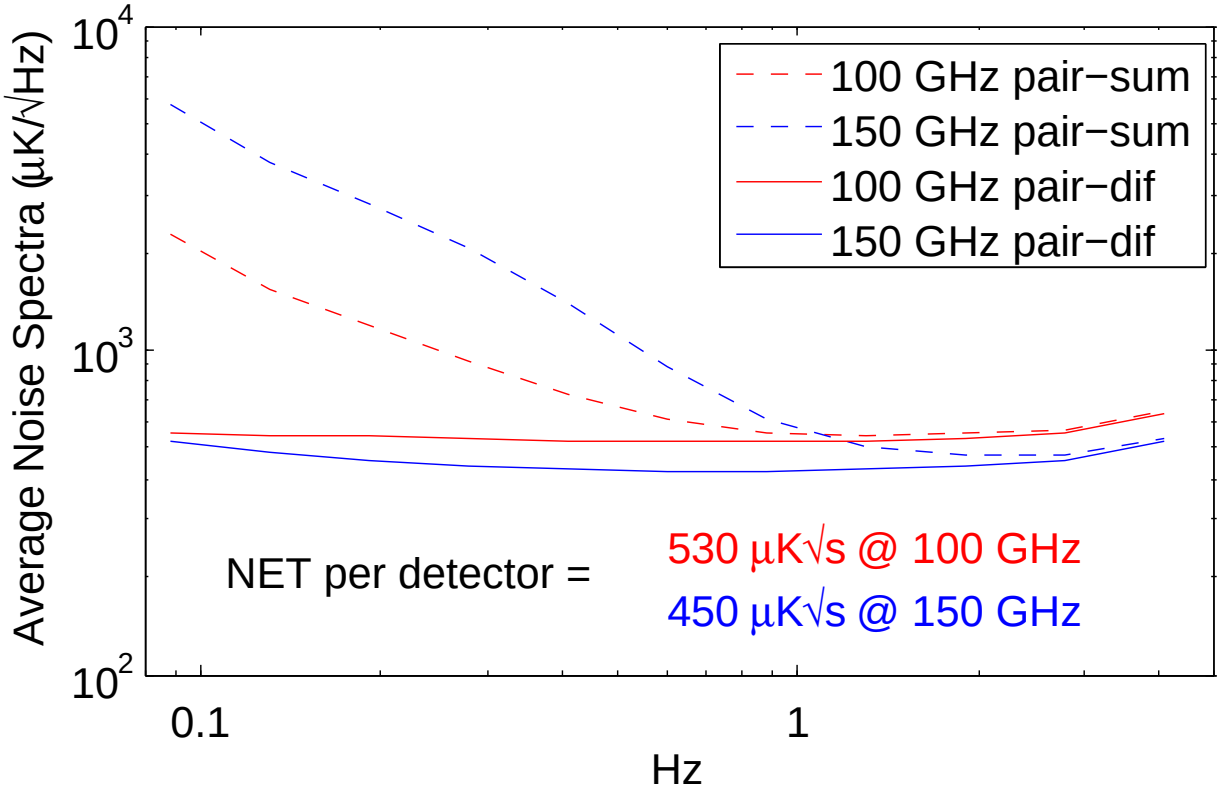

Figure 5.4: Average noise frequency spectra of all PSB pairs used in the analysis, averaged over all observing blocks during the entire first 2 years. The pair-sum spectra show $1/f$ atmospheric noise, which is rejected by pair differencing. We derived the noise equivalent temperatures per detector from the pair-difference average over 0.1–1 Hz. Accounting for polarization efficiencies $(1-\epsilon)/(1+\epsilon) \approx 0.93$, these correspond to an average instantaneous (i.e. single Stokes parameter) "NEQ per feed" of 410 and 340 $\mu\mathrm{K}\sqrt{s}$ for 100 and 150 GHz, respectively.

5.4.2 Simulation of noise-only timestreams

For each one-hour scan set, I used the model noise covariance matrices in the following steps to generate simulated noise timestreams that reflect the measured noise correlations:

1. For each of the 12 frequency bands of the noise model spectra, take the complex covariance matrix $\tilde{\mathbf{N}}(f)$ for sums and differences of all the good PSB pairs [74×74] and compute its complex Cholesky decomposition factor $\mathbf{L}(f)$ [lower triangular 74×74] such that $\tilde{\mathbf{N}}(f) = \mathbf{L}(f)\mathbf{L}^{\dagger}(f)$.

2. For each 20-second (200-sample) half-scan and each pair sum or difference, generate the positive frequency part of a complex spectrum template $\boldsymbol{\rho}$ [74×100] using normally-distributed random numbers whose magnitude has an expectation value of unity.

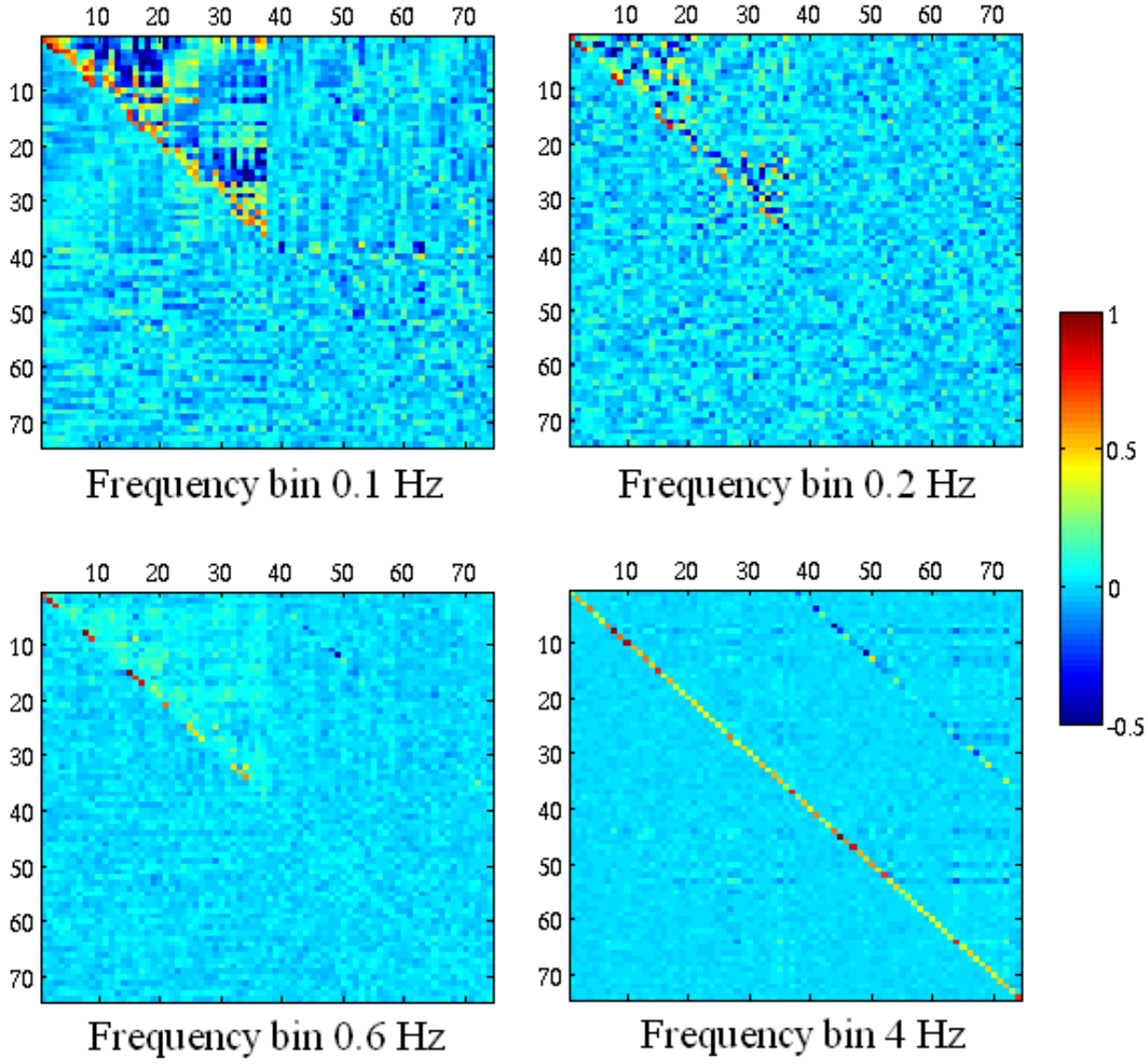

Figure 5.5: Example correlation matrices from the BICEP noise model. Each panel shows the fractional cross-correlations among PSB sums (indexes 1–37) and differences (indexes 38–74) of 37 PSB pairs used in 2007, with the real and imaginary components plotted in the upper-right and lower-left halves, respectively. The auto-spectra values along the diagonal are normalized simply by the maximum of the 74 values. The atmosphere-induced correlations are visible as off-diagonal structure among the pair sums. The imaginary component lack substantial power, except among the pair sums at the lowest frequencies where the correlations due to atmosphere can be phase shifted depending on the relative beam locations. We defined the noise model in 12 frequency bands spanning 0.05–5 Hz, and four of those bands are shown.

3. For each of the 100 positive frequency bins of this vector of unit-spectrum templates, multiply the Cholesky factor from the appropriate frequency band of the noise model: $\tilde{\mathbf{v}}(f) = \mathbf{L}(f)\boldsymbol{\rho}(f)$. The resulting spectra $\tilde{\mathbf{v}}(f)$ will have the same covariance as the actual data:

$$\begin{aligned} \langle \tilde{\mathbf{v}}(f)\tilde{\mathbf{v}}^{\dagger}(f) \rangle &= \langle \mathbf{L}(f)\boldsymbol{\rho}(f)\boldsymbol{\rho}^{\dagger}(f)\mathbf{L}^{\dagger}(f) \rangle \\ &= \mathbf{L}(f)\mathbf{L}^{\dagger}(f) \\ &= \tilde{\mathbf{N}}(f). \end{aligned} \tag{5.1}$$

4. To ensure that these $\tilde{\mathbf{v}}(f)$ approximate the spectra of real timestreams, set the negative frequency part to equal the complex conjugate of the positive frequency part, so that the real part is even and the imaginary part is odd.

5. Take the inverse Fourier transform of $\tilde{\mathbf{v}}(f)$ to generate 200 samples of simulated noise time series for each of the 74 timestreams (sum and difference for the 37 PSB pairs).

To evaluate the accuracy of the noise model and simulation, I fed the simulated timestreams back into the noise modeling pipeline and compared the resulting power spectral distributions and covariance matrix to those of the real data (Figure 5.6). The simulated timestreams successfully reproduced the complex covariance and the spectral amplitudes agreed to within <1% rms with no significant systematic differences.

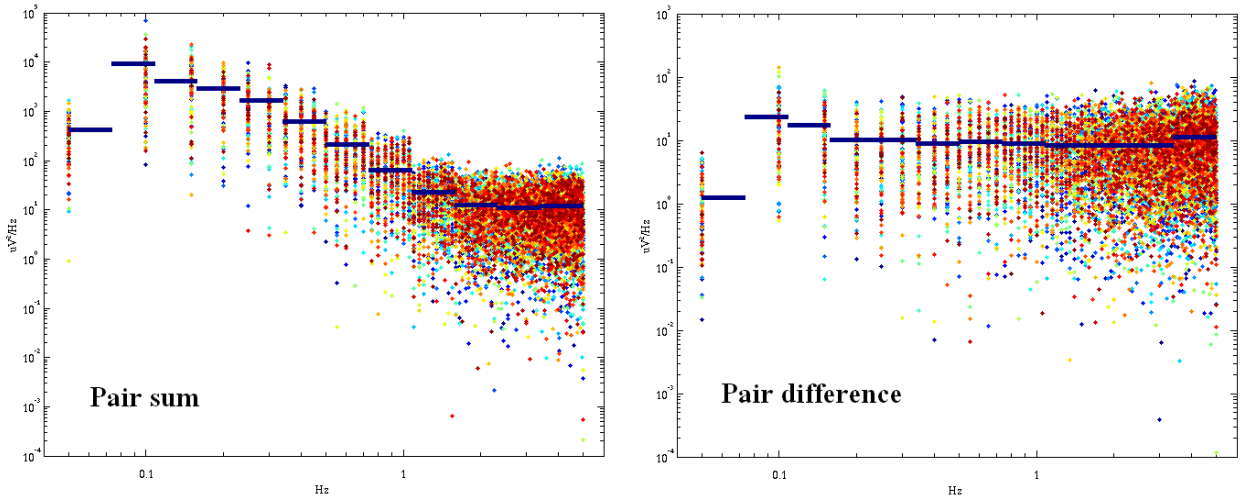

Figure 5.6: Noise model spectrum used for simulation (blue) and 100 half-scan spectra regenerated from simulated timestreams, plotted separately for pair sum (left) and pair difference (right) for one PSB pair. The consistency verifies the noise simulation algorithm.

We used the above procedure to generate 500 realizations of simulated noise timestreams for the entire data set. As with the real data, we calculated and subtracted scan-synchronous templates over each set of azimuth scans, and then co-added the noise timestreams into maps. Figure 5.7 shows example noise timestreams and maps.

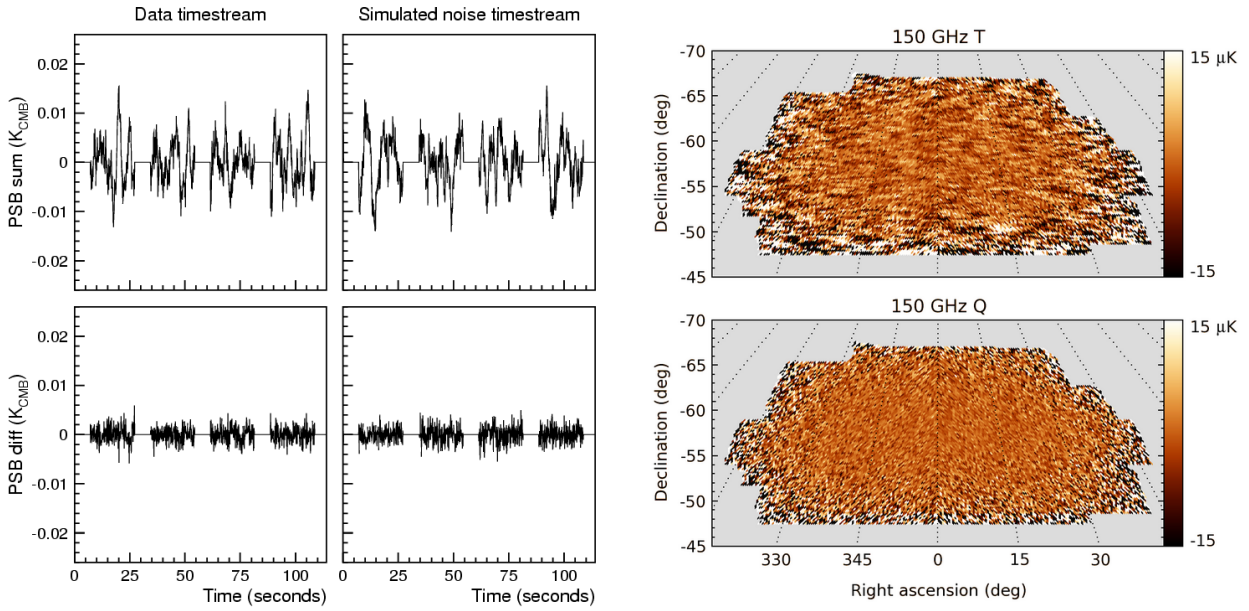

Figure 5.7: Real and simulated-noise timestreams for a PSB pair over four azimuth half-scans, showing accurate reproduction of the noise qualities. The simulated timestreams for all the PSB pairs over the 2 years were co-added to form the noise-only maps (right). The $1/f$ noise causes striping in the T map, while the Q polarization map approximates white noise. (Figure thanks to Cynthia.)

5.4.3 Noise bias in power spectra

We estimated the noise bias $\langle \hat{N}_\ell \rangle$ by averaging the power spectra from an ensemble of many simulated noise-only maps (Figure 5.8). The noise bias in TT was 3 orders of magnitude smaller than the signal, and the signal spectrum was sample-variance limited. For the TE, TB, and EB cross spectra, the noise from each map was mostly uncorrelated, with resulting $\langle \hat{N}_\ell \rangle$ distributed around 0. However, the noise contributed a significant portion of the raw EE signal and is expected to dominate the BB power spectrum. The error bar in the final spectrum was based on the scatter in the results from an ensemble of signal+noise simulations, and for BB was dominated by noise.

We checked the accuracy of the noise model by comparing the spectra of the simulated noise with those of "jackknife" maps, in which two maps made with complete halves of the data are differenced so that they are free of CMB signal and therefore nominally represent the noise level in the data. Jackknife divisions included those based on the left/right scan direction (shown in Figure 5.8), azimuth range, boresight rotation angle pairs, alternating observing weeks, 2006/2007 observing years, and focal plane detector split (more details in [5]). We tested for evidence of noise bias amplitude misestimation using these 6 types of jackknife spectra for EE and BB at 100 and 150 GHz (a total of 24 spectra) by comparing the sum of bandpower deviations over ℓ=300–500 to those from 100 realizations of noise simulations. The set of jackknife spectra from the actual data were consistent with the

simulated distributions, even in this high ℓ range where the effect of noise misestimation is expected to be the largest due to the bias being a rapidly increasing function of ℓ. Repeating this test with an intentionally-introduced $\pm 3\%$ scaling of the noise in the simulations, we could clearly detect a departure of the sum of the actual data jackknife bandpower deviations from those of the simulated distributions. This allowed us to place an upper limit on possible misestimation of the noise bias at this level, at least for a uniformly scaled error across the ℓ range.

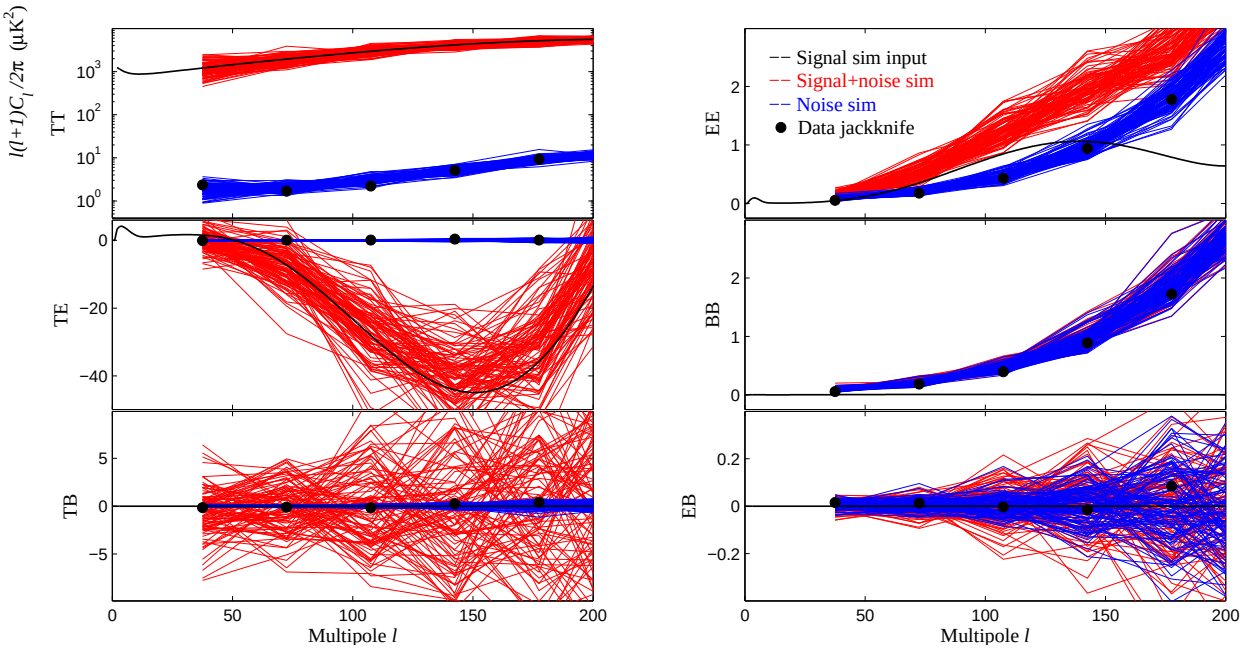

Figure 5.8: 150 GHz power spectra of 100 realizations of simulated signal+noise and noise only, compared to the scan-direction jackknife spectra from the actual data. The distributions of simulated noise spectra were consistent with the data jackknife spectra, expected to be signal-free and a good representation of noise in the data. The CMB signal simulation used the input spectra shown. Error bars in the final spectra were based on the scatter in the signal+noise spectra, which was noise-dominated for BB and EB and largely cosmic variance limited for the other spectra.

As described above, a $\pm 3\%$ misestimation of noise power would correspond to a maximum shift in our r estimate of 0.1 for the noise levels of the current 2-year data set. The actual 2-year constraint on r was $r = 0.02^{+0.31}_{-0.26}$ [5]. The jackknife-derived upper limit on possible misestimation of the noise bias scales with the noise level. Therefore, as the noise in future data releases decreases, we can expect this internal jackknife test to continue to allow us to place upper limits on noise misestimation (or to detect it if present) at a level corresponding to roughly 1/3 of the total statistical uncertainty on r, assuming a noise-limited BB spectrum, and less than this if a BB signal is detected.

5.5 Angular power spectra

After subtracting the noise bias, the next step toward the final power spectra was correcting for the CMB signal loss due to the polynomial filtering and scan-synchronous template removal. We quantified the ℓ-space filter function describing this signal loss through simulations of noise-free CMB signal, which was also used in Section 4.1. The simulation procedure began by generating model power spectra with the `CAMB` [29] software using ΛCDM parameters derived from *WMAP* 5-year data [16] with no tensor perturbations. From the model spectra, we created an ensemble of simulated CMB skies pixelized at 0.11° resolution using the `synfast` utility in `Healpix`. We then used actual pointing data to generate smoothly interpolated PSB timestreams from the simulated T, Q, U maps and their spatial derivatives. A PSB timestream sample that fell into a pixel was expressed as a convolution of the beam with a 2nd-order Taylor expansion of the sky signal around that pixel location. We simulated signal-only detector timestreams according to BICEP's scan strategy, including measured beam locations, PSB orientation angles, and cross-polarization responses. For the characterization of the timestream filtering effects, we did not include differential beam systematic effects to prevent mixing between temperature and polarization anisotropies. The simulated timestreams were filtered and weighted in exactly the same way as the real data and then co-added into maps. Once we had "BICEP-observed" simulated signal maps, we computed the power spectra and averaged the results over many realizations. We computed the filtering functions by dividing these average spectra by the input power spectra. We computed them explicitly only for TT and EE, and then used those to construct filtering functions for the other power spectra.

Finally, we quantified the uncertainties in the power spectra, consisting of two components, one proportional to the signal itself (sample variance), and another that depends on the noise. We estimated the errors by examining the variance of power spectra from simulated signal+noise maps, which have exactly taken into account time-dependent correlated noise, scan strategy, and sky coverage. We added the simulated noise and simulated signal maps, and computed the power spectra for each realization using the same noise bias and filter functions as applied to the real data (red in Figure 5.8). We then computed the band power covariance matrix from the ensemble of simulations. The band power errors came from square root of the diagonal terms of the matrix.

Figure 5.9 shows BICEP's 2-year CMB polarization spectra. The first peak of EE is resolved and sample variance limited. For BB, we have been able to lower the upper limits by an order of magnitude over *WMAP* even with only the first 2 years of data with fairly aggressive cuts. Potential systematic errors have been well below this sensitivity limit.

To constrain r from BICEP's BB spectrum, we compared the measured band powers to template BB curves with varied amplitudes of the inflationary component, assuming that it simply scales with r. The template BB curves were calculated using fixed ΛCDM parameters derived from *WMAP* 5-year data and a wide range of trial r values. We included a constant BB component from gravitational lensing, although the contribution was negligible at degree scales. The initial analysis of the first 2 years of data was able to constrain the tensor-to-scalar ratio to $r < 0.72$ @ 95% confidence. Full 3-year analysis with relaxed data cuts is ongoing with >1.6 times more data total.

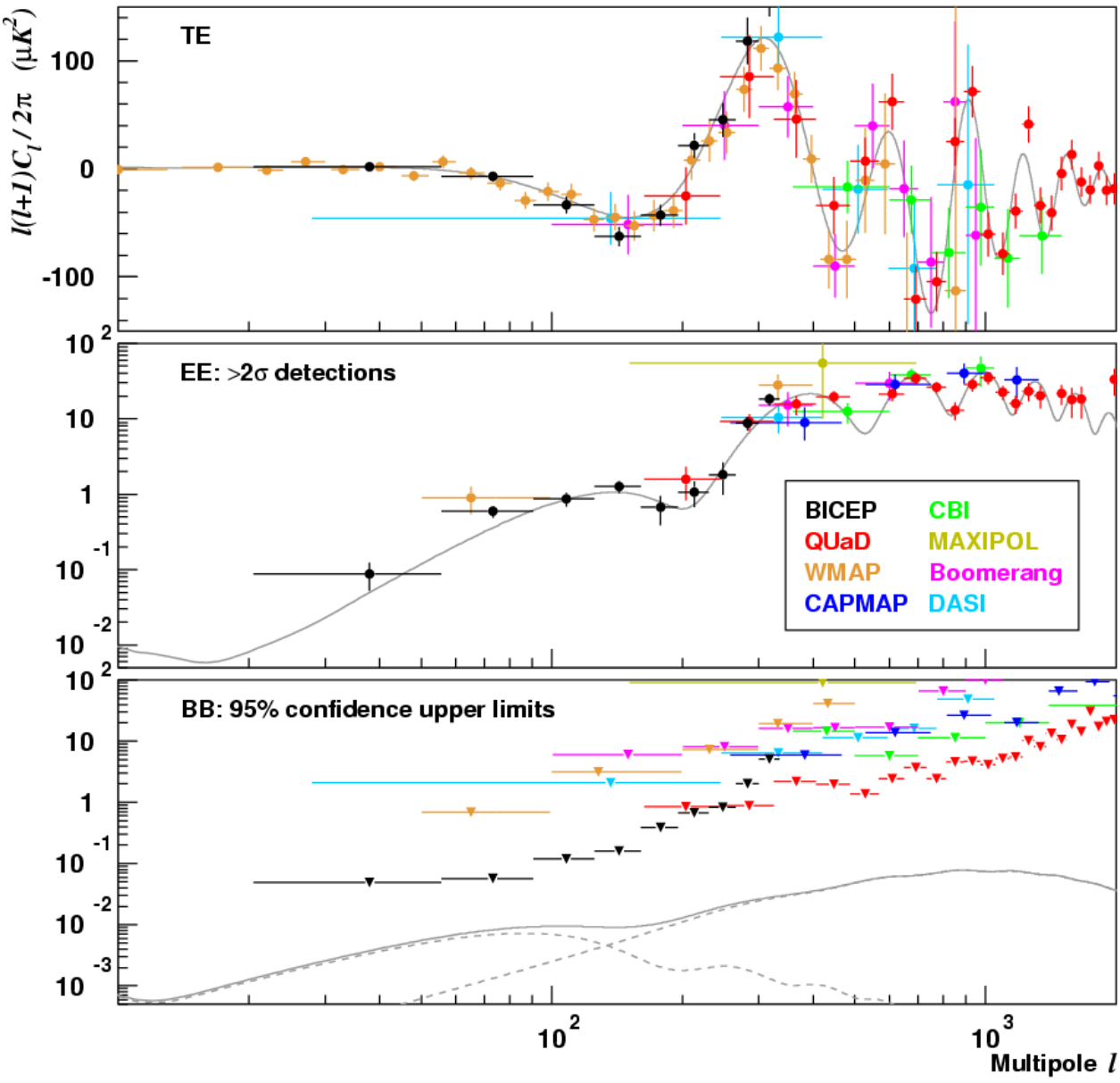

Figure 5.9: BICEP 2-year CMB polarization angular power spectra, compared with other experiments' results [5].

5.6 Conclusion

BICEP was an experiment built with a primary goal of targeting the signature of inflationary gravitational waves in the B-mode polarization of the CMB at angular scales near the expected peak of $\sim 2^\circ$. Its novel design emphasized simplicity and systematic control, employing a carefully-baffled compact cryogenic refractor and relying on a simple observing strategy of azimuth-scan modulation with periodic boresight rotation. BICEP achieved its design goals, being a path-finding experiment that demonstrated the strengths of a small aperture ground-based approach. Using BICEP's actual data analysis pipelines, we have identified those aspects of the experiment's instrumental and noise properties that require careful control and characterization. Careful instrument characterization shows that BICEP is not limited by systematic errors. We have established benchmarks for these quantities corresponding to the expected B-mode polarization signal for a tensor-to-scalar ratio of r=0.1, a value several times smaller than the level of statistical uncertainty of the BICEP 2-year result, $r = 0.02^{+0.31}_{-0.26}$, or $r < 0.72$ at 95% confidence [5].

This practical experience with BICEP provides a guide for future experiments in search for the signature of inflationary gravitational waves in CMB polarization. BICEP has shown that we can go deeper without being systematic error limited. Thus the path forward is to do the same with more throughput, more detectors. Since the beginning of 2010, the BICEP mount has been used for BICEP2. BICEP2 is very similar except with highly packed antenna-coupled transition-edge sensor array, totaling >200 bolometer pairs and the mapping speed expected to be >5 times faster. Based on success of the first BICEP, we can expect BICEP2 to advance the frontier toward potentially detecting the gravitational wave signal from inflation.

Bibliography

[1] P. A. R. Ade, G. Pisano, C. Tucker, and S. Weaver. A review of metal mesh filters. In *Society of Photo-Optical Instrumentation Engineers (SPIE) Conference Series*, volume 6275 of *Presented at the Society of Photo-Optical Instrumentation Engineers (SPIE) Conference*, July 2006.

[2] A. Albrecht and P. J. Steinhardt. Cosmology for grand unified theories with radiatively induced symmetry breaking. *Physical Review Letters*, 48:1220–1223, April 1982.

[3] Ralph A. Alpher and Robert C. Herman. Remarks on the evolution of the expanding universe. *Phys. Rev.*, 75(7):1089–1095, Apr 1949.

[4] J. Bock, A. Cooray, S. Hanany, B. Keating, A. Lee, T. Matsumura, M. Milligan, N. Ponthieu, T. Renbarger, and H. Tran. The Experimental Probe of Inflationary Cosmology (EPIC): A Mission Concept Study for NASA's Einstein Inflation Probe. *ArXiv e-prints*, May 2008.

[5] H. C. Chiang, P. A. R. Ade, D. Barkats, J. O. Battle, E. M. Bierman, J. J. Bock, C. D. Dowell, L. Duband, E. F. Hivon, W. L. Holzapfel, V. V. Hristov, W. C. Jones, B. G. Keating, J. M. Kovac, C. L. Kuo, A. E. Lange, E. M. Leitch, P. V. Mason, T. Matsumura, H. T. Nguyen, N. Ponthieu, C. Pryke, S. Richter, G. Rocha, C. Sheehy, Y. D. Takahashi, J. E. Tolan, and K. W. Yoon. Measurement of Cosmic Microwave Background Polarization Power Spectra from Two Years of BICEP Data. *Astrophys. J.* , 711:1123–1140, March 2010.

[6] G. Chon, A. Challinor, S. Prunet, E. Hivon, and I. Szapudi. Fast estimation of polarization power spectra using correlation functions. *Mon. Not. Roy. Astron. Soc.* , 350:914–926, May 2004.

[7] W. de Sitter. On the curvature of space. *Koninklijke Nederlandse Akademie van Weteschappen Proceedings Series B Physical Sciences*, 20:229–243, 1918.

[8] R. H. Dicke, P. J. E. Peebles, P. G. Roll, and D. T. Wilkinson. Cosmic Black-Body Radiation. *Astrophys. J.* , 142:414–419, July 1965.

[9] S. Dodelson, R. Easther, S. Hanany, L. McAllister, S. Meyer, and et al. Page, L. The Origin of the Universe as Revealed Through the Polarization of the Cosmic Microwave Background. In *AGB Stars and Related Phenomenastro2010: The Astronomy and Astrophysics Decadal Survey*, volume 2010 of *ArXiv Astrophysics e-prints*, pages 67–+, 2009.

[10] D. P. Finkbeiner, M. Davis, and D. J. Schlegel. Extrapolation of Galactic Dust Emission at 100 Microns to Cosmic Microwave Background Radiation Frequencies Using FIRAS. *Astrophys. J.* , 524:867–886, October 1999.

[11] G. Gamow. Expanding universe and the origin of elements. *Phys. Rev.*, 70(7-8):572–573, Oct 1946.

[12] G. Gamow. The origin of elements and the separation of galaxies. *Phys. Rev.*, 74(4):505–506, Aug 1948.

[13] K. M. Górski, E. Hivon, A. J. Banday, B. D. Wandelt, F. K. Hansen, M. Reinecke, and M. Bartelmann. HEALPix: A Framework for High-Resolution Discretization and Fast Analysis of Data Distributed on the Sphere. *Astrophys. J.* , 622:759–771, April 2005.

[14] A. H. Guth. Inflationary universe: A possible solution to the horizon and flatness problems. *Phys. Rev. D* , 23:347–356, January 1981.

[15] J. R. Hinderks, P. Ade, J. Bock, M. Bowden, M. L. Brown, G. Cahill, J. E. Carlstrom, P. G. Castro, S. Church, T. Culverhouse, R. Friedman, K. Ganga, W. K. Gear, S. Gupta, J. Harris, V. Haynes, B. G. Keating, J. Kovac, E. Kirby, A. E. Lange, E. Leitch, O. E. Mallie, S. Melhuish, Y. Memari, A. Murphy, A. Orlando, R. Schwarz, C. O. Sullivan, L. Piccirillo, C. Pryke, N. Rajguru, B. Rusholme, A. N. Taylor, K. L. Thompson, C. Tucker, A. H. Turner, E. Y. S. Wu, and M. Zemcov. QUaD: A High-Resolution Cosmic Microwave Background Polarimeter. *Astrophys. J.* , 692:1221–1246, February 2009.

[16] G. Hinshaw, J. L. Weiland, R. S. Hill, N. Odegard, D. Larson, C. L. Bennett, J. Dunkley, B. Gold, M. R. Greason, N. Jarosik, E. Komatsu, M. R. Nolta, L. Page, D. N. Spergel, E. Wollack, M. Halpern, A. Kogut, M. Limon, S. S. Meyer, G. S. Tucker, and E. L. Wright. Five-Year Wilkinson Microwave Anisotropy Probe Observations: Data Processing, Sky Maps, and Basic Results. *Astrophys. J. Suppl.* , 180:225–245, February 2009.

[17] W. Hu, M. M. Hedman, and M. Zaldarriaga. Benchmark parameters for CMB polarization experiments. *Phys. Rev. D* , 67(4):043004, February 2003.

[18] W. Hu and M. White. A CMB polarization primer. *New Astronomy*, 2:323–344, October 1997.

[19] E. Hubble. A Relation between Distance and Radial Velocity among Extra-Galactic Nebulae. *Proceedings of the National Academy of Science*, 15:168–173, March 1929.

[20] W. C. Jones, R. Bhatia, J. J. Bock, and A. E. Lange. A Polarization Sensitive Bolometric Receiver for Observations of the Cosmic Microwave Background. In T. G. Phillips & J. Zmuidzinas, editor, *Society of Photo-Optical Instrumentation Engineers (SPIE) Conference Series*, volume 4855 of *Presented at the Society of Photo-Optical Instrumentation Engineers (SPIE) Conference*, pages 227–238, February 2003.

[21] B. G. Keating, P. A. R. Ade, J. J. Bock, E. Hivon, W. L. Holzapfel, A. E. Lange, H. Nguyen, and K. W. Yoon. BICEP: a large angular scale CMB polarimeter. In S. Fineschi, editor, *Society of Photo-Optical Instrumentation Engineers (SPIE) Conference Series*, volume 4843 of *Presented at the Society of Photo-Optical Instrumentation Engineers (SPIE) Conference*, pages 284–295, February 2003.

[22] B. G. Keating, C. W. O'Dell, J. O. Gundersen, L. Piccirillo, N. C. Stebor, and P. T. Timbie. An Instrument for Investigating the Large Angular Scale Polarization of the Cosmic Microwave Background. *Astrophys. J. Suppl.* , 144:1–20, January 2003.

[23] Joseph B. Keller. How Dark is the Shadow of a Round-Ended Screen? *J. Appl. Phys.* , 30:1452–1454, September 1959.

[24] A. Kogut, D. N. Spergel, C. Barnes, C. L. Bennett, M. Halpern, G. Hinshaw, N. Jarosik, M. Limon, S. S. Meyer, L. Page, G. S. Tucker, E. Wollack, and E. L. Wright. First-Year Wilkinson Microwave Anisotropy Probe (WMAP) Observations: Temperature-Polarization Correlation. *Astrophys. J. Suppl.* , 148:161–173, September 2003.

[25] E. Komatsu, J. Dunkley, M. R. Nolta, C. L. Bennett, B. Gold, G. Hinshaw, N. Jarosik, D. Larson, M. Limon, L. Page, D. N. Spergel, M. Halpern, R. S. Hill, A. Kogut, S. S. Meyer, G. S. Tucker, J. L. Weiland, E. Wollack, and E. L. Wright. Five-Year Wilkinson Microwave Anisotropy Probe Observations: Cosmological Interpretation. *Astrophys. J. Suppl.* , 180:330–376, February 2009.

[26] J. M. Kovac, E. M. Leitch, C. Pryke, J. E. Carlstrom, N. W. Halverson, and W. L. Holzapfel. Detection of polarization in the cosmic microwave background using DASI. *Nature* , 420:772–787, December 2002.

[27] J. W. Lamb. Miscellaneous data on materials for millimetre and submillimetre optics. *International Journal of Infrared and Millimeter Waves*, 17:1997–2034, December 1996.

[28] G. Lemaître. Un Univers homogène de masse constante et de rayon croissant rendant compte de la vitesse radiale des nébuleuses extra-galactiques. *Annales de la Societe Scietifique de Bruxelles*, 47:49–59, 1927.

[29] A. Lewis, A. Challinor, and A. Lasenby. Efficient Computation of Cosmic Microwave Background Anisotropies in Closed Friedmann-Robertson-Walker Models. *Astrophys. J.* , 538:473–476, August 2000.

[30] A. R. Liddle. An Introduction to Cosmological Inflation. In A. Masiero, G. Senjanovic, & A. Smirnov, editor, *High Energy Physics and Cosmology, 1998 Summer School*, pages 260–+, 1999.

[31] A. D. Linde. A new inflationary universe scenario: A possible solution of the horizon, flatness, homogeneity, isotropy and primordial monopole problems. *Physics Letters B*, 108:389–393, February 1982.

[32] W. Lu and J. Ruhl. Measurement of reflectivity of eccosorb. Private communication, 2004.

[33] C. J. MacTavish, P. A. R. Ade, J. J. Bock, J. R. Bond, J. Borrill, A. Boscaleri, P. Cabella, C. R. Contaldi, B. P. Crill, P. de Bernardis, G. De Gasperis, A. de Oliveira-Costa, G. De Troia, G. di Stefano, E. Hivon, A. H. Jaffe, W. C. Jones, T. S. Kisner, A. E. Lange, A. M. Lewis, S. Masi, P. D. Mauskopf, A. Melchiorri, T. E. Montroy, P. Natoli, C. B. Netterfield, E. Pascale, F. Piacentini, D. Pogosyan, G. Polenta, S. Prunet, S. Ricciardi, G. Romeo, J. E. Ruhl, P. Santini, M. Tegmark, M. Veneziani, and N. Vittorio. Cosmological Parameters from the 2003 Flight of BOOMERANG. *Astrophys. J.* , 647:799–812, August 2006.

[34] J. C. Mather, E. S. Cheng, R. E. Eplee, Jr., R. B. Isaacman, S. S. Meyer, R. A. Shafer, R. Weiss, E. L. Wright, C. L. Bennett, N. W. Boggess, E. Dwek, S. Gulkis, M. G. Hauser, M. Janssen, T. Kelsall, P. M. Lubin, S. H. Moseley, Jr., T. L. Murdock, R. F. Silverberg, G. F. Smoot, and D. T. Wilkinson. A preliminary measurement of the cosmic microwave background spectrum by the Cosmic Background Explorer (COBE) satellite. *Astrophys. J. Lett.* , 354:L37–L40, May 1990.

[35] S. Meyer. Panel test report. Private communication, 2004.

[36] T. E. Montroy, P. A. R. Ade, J. J. Bock, J. R. Bond, J. Borrill, A. Boscaleri, P. Cabella, C. R. Contaldi, B. P. Crill, P. de Bernardis, G. De Gasperis, A. de Oliveira-Costa, G. De Troia, G. di Stefano, E. Hivon, A. H. Jaffe, T. S. Kisner, W. C. Jones, A. E. Lange, S. Masi, P. D. Mauskopf, C. J. MacTavish, A. Melchiorri, P. Natoli, C. B. Netterfield, E. Pascale, F. Piacentini, D. Pogosyan, G. Polenta, S. Prunet, S. Ricciardi, G. Romeo, J. E. Ruhl, P. Santini, M. Tegmark, M. Veneziani, and N. Vittorio. A Measurement of the CMB ¡EE¿ Spectrum from the 2003 Flight of BOOMERANG. *Astrophys. J.* , 647:813–822, August 2006.

[37] M. R. Nolta, J. Dunkley, R. S. Hill, G. Hinshaw, E. Komatsu, D. Larson, L. Page, D. N. Spergel, C. L. Bennett, B. Gold, N. Jarosik, N. Odegard, J. L. Weiland, E. Wollack, M. Halpern, A. Kogut, M. Limon, S. S. Meyer, G. S. Tucker, and E. L. Wright. Five-Year Wilkinson Microwave Anisotropy Probe Observations: Angular Power Spectra. *Astrophys. J. Suppl.* , 180:296–305, February 2009.

[38] C. O'Dell. A New Upper Limit on the Polarization of the Cosmic Microwave Background Radiation. *ArXiv Astrophysics e-prints*, January 2002.

[39] L. Page, G. Hinshaw, E. Komatsu, M. R. Nolta, D. N. Spergel, C. L. Bennett, C. Barnes, R. Bean, O. Doré, J. Dunkley, M. Halpern, R. S. Hill, N. Jarosik, A. Kogut, M. Limon, S. S. Meyer, N. Odegard, H. V. Peiris, G. S. Tucker, L. Verde, J. L. Weiland, E. Wollack, and E. L. Wright. Three-Year Wilkinson Microwave Anisotropy Probe (WMAP) Observations: Polarization Analysis. *Astrophys. J. Suppl.* , 170:335–376, June 2007.

[40] A. A. Penzias and R. W. Wilson. A Measurement of Excess Antenna Temperature at 4080 Mc/s. *Astrophys. J.* , 142:419–421, July 1965.

[41] A. G. Polnarev. Polarization and Anisotropy Induced in the Microwave Background by Cosmological Gravitational Waves. *Soviet Astronomy*, 29:607–+, December 1985.

[42] N. Ponthieu, J. F. Macías-Pérez, M. Tristram, P. Ade, A. Amblard, R. Ansari, J. Aumont, É. Aubourg, A. Benoît, J.-P. Bernard, A. Blanchard, J. J. Bock, F. R. Bouchet, A. Bourrachot, P. Camus, J.-F. Cardoso, F. Couchot, P. de Bernardis, J. Delabrouille, F.-X. Désert, M. Douspis, L. Dumoulin, P. Filliatre, P. Fosalba, M. Giard, Y. Giraud-Héraud, R. Gispert, J. Grain, L. Guglielmi, J.-C. Hamilton, S. Hanany, S. Henrot-Versillé, J. Kaplan, G. Lagache, A. E. Lange, K. Madet, B. Maffei, S. Masi, F. Mayet, F. Nati, G. Patanchon, O. Perdereau, S. Plaszczynski, M. Piat, S. Prunet, J.-L. Puget, C. Renault, C. Rosset, D. Santos, D. Vibert, and D. Yvon. Temperature and polarization angular power spectra of Galactic dust radiation at 353 GHz as measured by Archeops. *Astr. & Astroph.* , 444:327–336, December 2005.

[43] C. Pryke, P. Ade, J. Bock, M. Bowden, M. L. Brown, G. Cahill, P. G. Castro, S. Church, T. Culverhouse, R. Friedman, K. Ganga, W. K. Gear, S. Gupta, J. Hinderks, J. Kovac, A. E. Lange, E. Leitch, S. J. Melhuish, Y. Memari, J. A. Murphy, A. Orlando, R. Schwarz, C. O. Sullivan, L. Piccirillo, N. Rajguru, B. Rusholme, A. N. Taylor, K. L. Thompson, A. H. Turner, E. Y. S. Wu, and M. Zemcov. Second and Third Season QUaD Cosmic Microwave Background Temperature and Polarization Power Spectra. *Astrophys. J.* , 692:1247–1270, February 2009.

[44] V. A. Rubakov, M. V. Sazhin, and A. V. Veryaskin. Graviton creation in the inflationary universe and the grand unification scale. *Physics Letters B*, 115:189–192, September 1982.

[45] M. C. Runyan, P. A. R. Ade, R. S. Bhatia, J. J. Bock, M. D. Daub, J. H. Goldstein, C. V. Haynes, W. L. Holzapfel, C. L. Kuo, A. E. Lange, J. Leong, M. Lueker, M. Newcomb, J. B. Peterson, C. Reichardt, J. Ruhl, G. Sirbi, E. Torbet, C. Tucker, A. D. Turner, and D. Woolsey. ACBAR: The Arcminute Cosmology Bolometer Array Receiver. *Astrophys. J. Suppl.* , 149:265–287, December 2003.

[46] R. K. Sachs and A. M. Wolfe. Perturbations of a Cosmological Model and Angular Variations of the Microwave Background. *Astrophys. J.* , 147:73–+, January 1967.

[47] M. Shimon, B. Keating, N. Ponthieu, and E. Hivon. CMB polarization systematics due to beam asymmetry: Impact on inflationary science. *Phys. Rev. D* , 77(8):083003–+, April 2008.

[48] V. M. Slipher. Nebulae. *Proceedings of the American Philosophical Society*, 56:403–409, 1917.

[49] G. F. Smoot, C. L. Bennett, A. Kogut, E. L. Wright, J. Aymon, N. W. Boggess, E. S. Cheng, G. de Amici, S. Gulkis, M. G. Hauser, G. Hinshaw, P. D. Jackson, M. Janssen, E. Kaita, T. Kelsall, P. Keegstra, C. Lineweaver, K. Loewenstein, P. Lubin, J. Mather, S. S. Meyer, S. H. Moseley, T. Murdock, L. Rokke, R. F. Silverberg, L. Tenorio, R. Weiss,

and D. T. Wilkinson. Structure in the COBE differential microwave radiometer first-year maps. *Astrophys. J. Lett.* , 396:L1–L5, September 1992.

[50] Y. D. Takahashi, P. A. R. Ade, D. Barkats, J. O. Battle, E. M. Bierman, J. J. Bock, H. C. Chiang, C. D. Dowell, L. Duband, E. F. Hivon, W. L. Holzapfel, V. V. Hristov, W. C. Jones, B. G. Keating, J. M. Kovac, C. L. Kuo, A. E. Lange, E. M. Leitch, P. V. Mason, T. Matsumura, H. T. Nguyen, N. Ponthieu, C. Pryke, S. Richter, G. Rocha, and K. W. Yoon. Characterization of the BICEP Telescope for High-precision Cosmic Microwave Background Polarimetry. *Astrophys. J.* , 711:1141–1156, March 2010.

[51] K. W. Yoon, P. A. R. Ade, D. Barkats, J. O. Battle, E. M. Bierman, J. J. Bock, J. A. Brevik, H. C. Chiang, A. Crites, C. D. Dowell, L. Duband, G. S. Griffin, E. F. Hivon, W. L. Holzapfel, V. V. Hristov, B. G. Keating, J. M. Kovac, C. L. Kuo, A. E. Lange, E. M. Leitch, P. V. Mason, H. T. Nguyen, N. Ponthieu, Y. D. Takahashi, T. Renbarger, L. C. Weintraub, and D. Woolsey. The Robinson Gravitational Wave Background Telescope (BICEP): a bolometric large angular scale CMB polarimeter. In Jonas Zmuidzinas, editor, *Millimeter and Submillimeter Detectors and Instrumentation for Astronomy III*, volume 6275 of *Proc. SPIE*, page 62751K, 2006.

[52] Ki Won Yoon. *Design and deployment of BICEP: A novel small-aperture CMB polarimeter to test inflationary cosmology.* PhD thesis, California Institute of Technology, 2007.